PREDICTIVE MODELING FOR DUCTILE MACHINING OF BRITTLE MATERIALS

A Dissertation
Presented to
The Academic Faculty

By

Sivaramakrishnan Venkatachalam

In Partial Fulfillment
of the Requirements for the Degree
of Doctor of Philosophy in the
George W. Woodruff School of Mechanical Engineering

Georgia Institute of Technology
December, 2007

PREDICTIVE MODELING FOR DUCTILE MACHINING OF BRITTLE MATERIALS

Approved by:

Dr. Steven Y. Liang, Advisor
George W. Woodruff School of Mechanical Engineering
Georgia Institute of Technology

Dr. Xiaoping Li, Co-Advisor
Department of Mechanical Engineering
National University of Singapore

Dr. Shreyes N. Melkote
George W. Woodruff School of Mechanical Engineering
Georgia Institute of Technology

Dr. Richard W. Neu
George W. Woodruff School of Mechanical Engineering
Georgia Institute of Technology

Dr. Hamid Garmestani
School of Materials Science & Engineering
Georgia Institute of Technology

Dr. Paul Griffin
H. Milton Stewart School of Industrial and Systems Engineering
Georgia Institute of Technology

Date Approved: 10/10/2007

To my Amma and Appa

ACKNOWLEDGEMENTS

I would, first of all, like to thank my advisor Dr. Steven Liang for all the support, guidance and encouragement throughout the course of my graduate study. I would also like to thank the members of my thesis committee, Professors Shreyes Melkote, Richard Neu, Hamid Garmestani and Paul Griffin. I would especially like to thank my co-advisor Dr. Xiaoping Li and his support staff at National University of Singapore (NUS) for providing the facilities and assistance to carry out my cutting experiments. I would also like to thank my colleagues at NUS, Cai Minbo and Rajanish Javvaji for their hospitality during my stay in Singapore.

Thanks are also due to Steven Sheffield, John Graham for their assistance in conducting my experiments. I would also like to thank all the support staff in MARC and ME for all their help especially John Morehouse, Pam Rountree, Glenda Johnson, Trudy Allen and Wanda Joefield.

I would also like to thank Yolande Berta and Todd Walters for training me to use the SEM. I would also like to acknowledge Dr. Dongsheng Li, Vikas Behrani, Krishna Tunga and Ananya Bhattacharya for their help with sample preparation and EBSD experiments. I would also like to thank Brandon Hernandez, applications engineer from Gatan Inc., for helping me in preparing samples for EBSD experiments. I would like to thank Dr. Mike Haluska for training me on XRD and Melanie Kirkham for her help in using the software for XRD.

I would like to thank my colleagues, Hyung-Wook Park, Ramesh Singh, Sathyan Subbiah, Jiann-Cherng Su, Kuan-Ming Li, Adam Cardi, Carl Hanna, Qiulin Xie, Haiyan

Deng, Austin Chen, and Jing-Ying Zhang for their help and support during my stay at Georgia Tech. I would also like to thank my roommate Sudhakar Jagannathan for his support and understanding during my stay in Atlanta.

Finally, I am indebted to my family especially my mom, dad, sister, brother-in-law, and nephew for their love, support, encouragement and understanding throughout my graduate study. This thesis would not be possible without them.

TABLE OF CONTENTS

ACKNOWLEDGEMENTS iv

LIST OF TABLES x

LIST OF FIGURES xi

LIST OF SYMBOLS xviii

SUMMARY xxi

CHAPTER 1 INTRODUCTION 1

1.1 Overview of Machining 1

1.2 Precision and Ultraprecision Machining 3

1.3 Ductile-Regime Machining 6

1.4 Objectives and Research Plan 8

1.5 Thesis Organization 10

CHAPTER 2 LITERATURE REVIEW 12

2.1 Force Modeling 12

2.2 Tool Edge Radius Measurement 20

2.3 Ductile-Regime Machining 23

2.3.1 Modeling 23

2.3.2 Experimental Investigations 28

2.3.3 Tool Wear 32

2.4 Material Constitutive Model 37

2.5 Effect of Microstructure 40

2.6 High Pressure Phase Transformation (HPPT) 42

2.7 Summary 45

CHAPTER 3 PREDICTIVE MODEL TO DETERMINE TRANSITION UNDEFORMED CHIP THICKNESS FOR SINGLE CRYSTAL SILICON 47

3.1 Properties of Silicon 49

3.2 Force Model 51

3.3 Material Constitutive Model 56

3.4 Strain and Strain Rate 58

3.5 Fracture Toughness 62

3.6 Comprehensive Model 67

3.7 Experimental Set-Up 70

3.8 Experimental Procedure and Results 72

3.8.1 Force Measurements 72

3.8.2 Surface Texture 75

3.8.3 Surface Roughness 78

3.8.4 Chip Formation 82

3.9 Simulation Results and Model Comparison 84

3.9.1 Determination of Forces 85

3.9.2 Determination of Transition Undeformed Chip Thickness 101

3.10 Summary 107

CHAPTER 4 ULTRAPRECISION MACHINING OF POLYCRYSTALLINE BRITTLE MATERIALS 109

4.1 Defects in Crystals – Dislocations and Grain Boundaries 112

4.2 Modeling Microstructure Effects 115

4.3 Ultraprecision Machining of Polycrystalline Germanium 118

4.3.1 Experimental Procedure 119
4.3.2 Experimental Force Measurements 120
4.3.3 Prediction of Forces 121
4.3.3.1 Material Constitutive Model 122
4.3.3.2 Misorientation 123
4.3.3.3 Shear Strain and Strain-rate 126
4.3.3.4 Force Prediction 127
4.3.3.5 Sensitivity Analysis 129
4.3.4 Summary 133
4.4 Ultraprecision Machining of Polycrystalline Silicon Carbide 133
4.4.1 Experimental Procedure 135
4.4.2 Experimental Force Measurements 136
4.4.3 Grain Size Measurement 137
4.4.4 Surface Texture and Chip Formation 139
4.4.5 Prediction of Forces 141
4.4.5.1 Material Constitutive Model 141
4.4.5.2 Shear Strain and Strain-rate 142
4.4.5.3 Force Prediction 143
4.4.5.4 Effect of Microstructure 144
4.4.5.5 Effects of microstructure on cutting and thrust forces 150
4.4.5.6 Summary 156
4.5 Chapter Summary 158
CHAPTER 5 CONCLUSIONS AND FUTURE WORK 159

5.1 Dissertation Overview 159

5.2 Conclusions and Contributions 160

5.3 Recommendations for Future Work 163

REFERENCES 166

LIST OF TABLES

Table 3-1 Properties of Silicon 50

Table 3-2 Johnson-Cook constants for Si 58

Table 3-3 Experimental plan for single crystal silicon 72

Table 3-4 Depth of cut measurements 76

Table 3-5 Theoretical roughness for end turning of silicon 79

Table 3-6 Computation of undeformed chip thickness (UCT) 90

Table 3-7 Computation results for chip flow direction and equivalent side cutting edge angle 94

Table 3-8 Full factorial design for sensitivity analysis 99

Table 3-9 Effect of nominal tool rake angle on transition undeformed chip thickness .. 105

Table 4-1 Machining conditions for polycrystalline germanium (Yan et al., 2004) 119

Table 4-2 Results of optimization process for determining material constants in JC model 122

Table 4-3 Matrices representing the 24 symmetry operations for the cubic system 125

Table 4-4 Misorientation angles for all 24 symmetry operations for the cubic system.. 126

Table 4-5 Constants used in (4.5) 128

Table 4-6 Design of experiments for sensitivity analysis 130

Table 4-7 Machining conditions for polycrystalline silicon carbide 135

Table 4-8 Undeformed chip thickness (UCT) for various depths of cut 136

Table 4-9 Johnson-Cook constants for SiC 142

Table 4-10 Properties of silicon carbide 147

Table 4-11 Sample preparation techniques for EBSD experiments 150

Table 4-12 Design of experiments analysis for *p*-SiC 152

LIST OF FIGURES

Figure 1.1 Orthogonal Machining process.. 2

Figure 1.2 The development of achievable machining accuracy (Taniguchi, 1983).......... 4

Figure 1.3 Micromachining utilizing conventional size machine tools (Ehmann et al., 2007) 5

Figure 1.4 Micromachining utilizing miniaturized machine tools and microfactories (Ehmann et al., 2007).. 6

Figure 1.5 Schematic of ductile-regime machining (Liu et al., 2004)............................... 7

Figure 1.6 Outline of research plan.. 9

Figure 2.1 Composite cutting force circle (Merchant, 1945)... 13

Figure 2.2 Force components in cutting with a rounded tool edge (Albrecht, 1960)....... 14

Figure 2.3 Extrapolation method to determine ploughing forces (Abdelmoneim and Scrutton, 1974)... 15

Figure 2.4 (a) An equilibrium system of forces acting in the deformation zone (b) Equivalent rake angle due to tool edge radius (c) Flow pattern of workpiece approaching tool with finite radius (Connolly and Rubenstein, 1968)... 16

Figure 2.5 Schematic model of micro-cutting for molecular dynamics simulation (Shimada et al., 1992) 17

Figure 2.6 Chip formation in nanometric cutting of copper with nominal thickness of cut of 1 nm (left) and 20 nm (right). (Ikawa et al., 1992).. 18

Figure 2.7 Size effect in metal removal process (Subbiah, 2006) 20

Figure 2.8 SEM image showing the line of contamination as the edge profile (Drescher, 1993) 22

Figure 2.9 Optical image and least square fit to determine tool edge radius (Venkatachalam and Liang, 2007)... 22

Figure 2.10 a) Indentation pattern showing lateral crack (top) and median crack (bottom) for Vickers indentation test b) Vickers indentation data on soda lime glass (Lawn et al., 1976) 24

Figure 2.11 Machining geometry used to derive cutting model (Blackley and Scattergood, 1991) 26

Figure 2.12 Domain diagram for brittle/ductile mode transition at low cutting speed and t = 2 μm (Ueda et al., 1991) 27

Figure 2.13 Surface generated and chip formation in single crystal silicon ductile machining (Yan et al., 2002) 29

Figure 2.14 Tool wear for brittle mode removal (left) and ductile mode removal (right) (Yan et al., 2003) 33

Figure 2.15 Formation of sub-cutting edges on the main cutting edge due to nano/micro grooves (Li et al., 2005) 34

Figure 2.16 Area of ductile material removal in (001) silicon (left) and (111) silicon (right) (Shibata et al., 1996) 35

Figure 2.17 Crystallographic orientation dependence on critical chip thickness (Yan et al., 2002) 36

Figure 2.18 Critical chip thickness as a function of crystal orientation (O'Connor et al., 2005) 36

Figure 2.19 Schematic of effect of crystallographic orientation on surface roughness for (100), (110) and (111) single crystal copper (Lee et al., 2000) 37

Figure 2.20 (a) Comparison of yield fucntions in principal stress space (b) Yield and phase transformation surfaces in principal stress space (loading) (Vodenitcharova and Zhang, 2004) 39

Figure 2.21 (a) Elastic-plastic material behavior (b) Experimental working diagram of hydrostatic stress vs. volumetric total strain in pure hydrostatic compression (Vodenitcharova and Zhang, 2004) 40

Figure 2.22 TEM picture of a polycrystalline silicon carbide chip (Bhattacharya et al., 2005) 43

Figure 2.23 Critical states of phase transformations under indentation for silicon (Zhang, 2004) 43

Figure 2.24 Grinding induced deformation a) both amorphous layer and dislocations b) dislocations for table speed of 1 m/min c) dislocations for table speed of 0.02 m/min (Zhang and Zarudi, 2001) 44

Figure 2.25 TEM image of machined surface showing amorphous layer, microcracks and dislocations (Jasinevicius et al., 2007) 45

Figure 3.1 Brittle material removal (left) and ductile material removal (right) (adopted from O'Connor, 2002) 49

Figure 3.2 Mechanics around the rounded tool edge (Venkatachalam and Liang, 2007) 53

Figure 3.3 Equivalent rake angle for different undeformed chip thickness (Liu K., 2002) 55

Figure 3.4 Determination of shear strain in cutting (Shaw, 1987) 59

Figure 3.5 Geometry of cutting process (reproduced from Manjunathaiah and Endres, 2000) 61

Figure 3.6 Basic modes of loading involving different crack surface displacements (Hertzberg, 1976) 63

Figure 3.7 Crack inclined θ degrees from z axis. Mode I dominates when $\theta > 60^o$ (Hertzberg, 1976) 64

Figure 3.8 Distribution of stresses in the vicinity of crack tip (Hertzberg, 1976) 64

Figure 3.9 Plat with cracks (non-inclined (left) and inclined (right)) subject to uniform stress (Liu K., 2002) 66

Figure 3.10 Schematic of comprehensive prediction model 69

Figure 3.11 Toshiba ULG-100C ultraprecision machine tool 70

Figure 3.12 Single point synthetic diamond tool 71

Figure 3.13 End turning set-up on the ultraprecision machine tool 72

Figure 3.14 Experimental forces measured for Si (100) and f = 1 μm/rev 73

Figure 3.15 Experimental forces measured for Si (111) and f = 1 μm/rev 73

Figure 3.16 Experimental forces measured for Si (110) and f = 1 μm/rev 74

Figure 3.17 Experimental forces measured for Si (100) and f = 2 μm/rev 74

Figure 3.18 Experimental forces measured for Si (110) and f = 2 μm/rev 75

Figure 3.19 Surface texture for undeformed chip thickness values of a) 62 nm, b) 99 nm, c) 140 nm, d) 197 nm, e) 434 nm, and f) 598 nm for Si (111) and f = 1 μm/rev 78

Figure 3.20 Roughness when turning with a tool having a nose radius 79

Figure 3.21 Surface roughness for Si (100) 80

Figure 3.22 Surface roughness for Si (110) 81

Figure 3.23 Surface roughness for Si (111) 81

Figure 3.24 Surface roughness profiles for Si (100) and f = 1 μm/rev measured using Zygo 82

Figure 3.25 Schematic of cut silicon wafer surface 83

Figure 3.26 Types of chip formation in silicon machining: ductile ((a) – (c)), ductile-brittle ((d) – (f)), brittle ((g) – (j)) 84

Figure 3.27 Orthogonal cutting vs. turning 85

Figure 3.28 Indentation of tool on copper for edge radius measurement 86

Figure 3.29 Measurement of tool edge radius on an AFM 86

Figure 3.30 Fitting a circle to three points 87

Figure 3.31 Computation of edge radius of the tool using Matlab® 89

Figure 3.32 Schematic for determining maximum undeformed chip thickness (Liu K., 2002) 89

Figure 3.33 Geometry of chip flow for nose radius tools (Oxley, 1989) 91

Figure 3.34 Comparison between Oxley and Waldorf for computing width of cut 95

Figure 3.35 Comparison of (a) shear strain and (b) strain-rate for a nominal rake angle $\gamma = 0^o$ and cutting velocity V = 1.1257 m/sec 96

Figure 3.36 Shear flow stress vs undeformed chip thickness 96

Figure 3.37 Oblique cutting geometry 97

Figure 3.38 Comparison between experimental and predicted force values 98

Figure 3.39 Main effects plot for cutting force (F_c) 100

Figure 3.40 Main effects plot for thrust force (F_t) 100

Figure 3.41 Main effects plot for shear angle (φ) 101

Figure 3.42 Cutting and thrust forces as fucntions of t_0 102

Figure 3.43 Effect of cutting velocity on transition undeformed chip thickness 104

Figure 3.44 Transition undeformed chip thickness map for single crystal silicon 106

Figure 4.1 Microstructure effects in machining (adopted from Zhou et al. (2001))....... 111

Figure 4.2 Movement of a solid cube along a slip plane (a) cube showing anticipated slip plane (b) slipped cube showing relative displacement (Hertzberg, 1976) 112

Figure 4.3 Schematic of edge (left) and screw (right) dislocations 113

Figure 4.4 Movement of edge dislocation across the crystal lattice under shear stress (Kalpakjian and Schmid, 2003) 114

Figure 4.5 Grains and grain boundaries 115

Figure 4.6 Sample grain structure of Alumina (Al_2O_3) & lognormal distribution for grain size 117

Figure 4.7 Grain map of *p*-Ge obtained using Orientation Imaging Microscopy (OIM) and corresponding Euler angles for the three grains (reproduced from Yan et al., 2004) 119

Figure 4.8 Machining model: a – depth of cut; h – undeformed chip thickness; f – feed; b – width of cut; κ – cutting edge angle (reproduced from Yan et al., 2004) 120

Figure 4.9 Experimental force data extracted from Yan et al., (2004) 121

Figure 4.10 Schematic of the grain map in polycrystalline germanium 123

Figure 4.11 Schematic of misorientation between two grains 124

Figure 4.12 Comparison of (a) shear strain and (b) strain-rate for a nominal rake angle $\gamma = -20^o$ and cutting velocity V = 5 m/sec 126

Figure 4.13 Comparison of predicted forces with corresponding experimental values . 127

Figure 4.14 Force comparison for grains *A* and *B* 129

Figure 4.15 Main effects plot for cutting force (F_c) 131

Figure 4.16 Main effects plot for thrust force (F_t) 132

Figure 4.17 Main effects plot for shear angle (φ) 132

Figure 4.18 (a) Crystal structure of silicon carbide (left) with the blue atoms representing silicon and the gray atoms representing carbon (b) Multiple unit cells with 100 plane. 134

Figure 4.19 Schematic of machining setup and cutting force measurement system 135

Figure 4.20 Measured cutting and thrust forces for *p*-SiC 136

Figure 4.21 Methods for measuring grain size (a) caliper method (b) line intercept method (Brandon & Kaplan, 1999) 137

Figure 4.22 Grain size measurements for *p*-SiC 138

Figure 4.23 (a) *p*-SiC grain size measurement results (b) lognormal distribution for grain size 140

Figure 4.24 (a) SiC wafer as received (b) UCT = 11.11 nm (c) UCT = 15.74 nm (d) UCT = 35.20 nm 141

Figure 4.25 (a) Strain and (b) Strain-rate computation for *p*-Sic 143

Figure 4.26 Comparison of measured and predicted cutting and thrust forces for *p*-SiC 144

Figure 4.27 (a) Variation of normal flow stress with grain size, D (b) conventional plot of normal stress versus square root of grain size 146

Figure 4.28 Diffraction of X-rays by a crystal (Cullity, 1978) 148

Figure 4.29 X'Pert PRO MRD instrument (PANalytical) 149

Figure 4.30 Intensity (I) vs. 2θ for *p*-SiC 150

Figure 4.31 Force comparisons illustrating the effects of microstructure 151

Figure 4.32 Force variations for a period of (a) 0.5 sec and (b) one revolution 153

Figure 4.33 Simulation representation of two grains of *p*-SiC 154

Figure 4.34 Deformation in the grain boundary zone 154

Figure 4.35 Simulated cutting and thrust forces 155

Figure 4.36 Main effects plot for cutting force (F_c) 157

Figure 4.37 Main effects plot for thrust force (F_t) 157

Figure 5.1 Complexities involved in ductile-regime machining 164

LIST OF SYMBOLS

t_0	undeformed chip thickness
t_1	chip thickness
γ_k	instantaneous rake angle
φ_k	instantaneous shear angle
β_k	instantaneous friction angle
γ	nominal rake angle
φ	nominal shear angle
β	nominal friction angle
γ_e	equivalent rake angle
φ_e	equivalent shear angle
r_c	chip ratio
r	tool edge radius
R	tool nose radius
k_s	shear flow stress
dF_c, dF_t	differential forces in cutting and thrust directions
F_c, F_t, F_r	forces in cutting, thrust and radial directions
A, B, C, m, n	Johnson-Cook flow stress constants
σ	normal flow stress
ε	normal strain
$\dot{\varepsilon}$	normal strain-rate
T_m	melting point of material
T_r	environment temperature

T	material temperature
γ_s	shear strain
$\dot{\gamma}$	shear strain-rate
V	cutting velocity
V_s	shear velocity
K_I	stress intensity factor (Mode I)
K_{II}	stress intensity factor (Mode II)
K_{Ic}	fracture toughness (Mode I)
F	geometric factor in stress intensity equation
a	crack length
W	width of finite plate with internal crack
E	elastic (Young's) modulus
H	hardness
G	shear modulus
f	feed
R_a	average roughness
R_t	peak-to-valley roughness
w	width of cut
a_0	depth of cut (turning)
C_s	side cutting edge angle
C_s^*	equivalent side cutting edge angle
ρ_t	total dislocation density
ρ_0	dislocation density in the volume between boundaries

ρ_b	dislocation density per unit volume
θ_{av}	average misorientation angle
k	constant based on type of grain boundary
D_{avg}	average grain boundary spacing
M	Taylor factor
b	burgers vector
α	material constant
D	grain size
θ	misorientation angle
$\varphi_1, \Phi, \varphi_2$	Euler angles

SUMMARY

Brittle materials such as silicon, germanium, glass and ceramics (silicon carbide, silicon nitride etc.) are widely used in semiconductor, optical, micro-electronics and various other fields. The surface finish requirements for these applications are very stringent and hence the finishing processes have to be conducive to producing high quality surfaces. Traditionally, grinding, polishing and lapping have been employed to achieve high tolerance in surface texture of silicon wafers in semiconductor applications, lenses for optical instruments etc. The conventional machining processes such as single point turning and milling are not conducive to brittle materials as they produce discontinuous chips owing to brittle failure at the shear plane before any tangible plastic flow occurs. The brittle fracture significantly influences the surface integrity of the part being machined. In order to improve surface finish on machined brittle materials, ductile regime machining is being extensively studied lately. The process of machining brittle materials where the material is removed by plastic flow, thus leaving a crack free surface is known as ductile-regime machining. This mode of micro-machining has been adopted based on the fact that all materials will deform plastically if the scale of deformation is very small. Ductile machining of brittle materials can produce surfaces of very high quality comparable with processes such as polishing, lapping etc.

The objective of this project is to develop a comprehensive predictive model for ductile machining of brittle materials. The model would predict the critical undeformed chip thickness (depth of cut) required to achieve ductile-regime machining. The input to the model includes tool geometry, workpiece material properties and machining process

parameters. The fact that the scale of ductile regime machining is very small leads to a number of factors assuming significance which would otherwise be neglected. The effects of tool edge radius, grain size, grain boundaries, crystal orientation etc. are studied so as to make better predictions of forces and hence the critical undeformed chip thickness. The model is validated using a series of experiments with varying materials and cutting conditions.

This research would aid in predicting forces and undeformed chip thickness values for different brittle materials given their material properties and process conditions. The output could be used to machine brittle materials without fracture and hence preserve their surface texture quality. The need for resorting to experimental trial and error is greatly reduced as the critical parameter, namely undeformed chip thickness, is predicted using this approach. This can in turn pave way for brittle materials to be utilized in many more applications.

CHAPTER 1

INTRODUCTION

1.1 Overview of Machining

The goal of changing the geometry of a raw material in order to form a mechanical part can be met by (i) putting material together, (ii) moving material from one region to another or (iii) removing unnecessary material (Shaw, 1987). The process of removing material from the bulk is termed machining. The process of machining can be further categorized based on the method of material removal as turning, milling, drilling, grinding etc. The process of cutting (turning, milling, and drilling) involves the removal of chips in the form of ribbons or particles. In order to perform cutting operations, different machine tools such as lathes, drilling machines, horizontal and vertical milling machines etc. are utilized.

The mechanics of the cutting process are best understood by studying the two dimensional orthogonal cutting process as shown in Figure 1.1. The cutting tool moving with a velocity V removes a thickness t_0 of material (workpiece) to form a new surface. The thickness t_0 is known as the undeformed (uncut) chip thickness and V is termed cutting velocity. The thickness of the chip, t_1, moving with a velocity V_c, is generally higher than the undeformed chip thickness and hence their ratio, termed as chip ratio, is generally less than unity. There are three important angles, namely the rake, shear and clearance angles, which influence the nature of material removal. The rake angle, γ, is the angle that the rake face of the tool makes with the direction perpendicular to the cutting velocity. The shear angle, φ, is the angle that the shear plane makes with the direction of

cutting velocity. The clearance angle, θ, is the angle that the clearance face of the tool makes with the direction of cutting velocity. The process of orthogonal cutting with continuous chip formation has two deformation zones as shown in Figure 1.1. The primary deformation zone stretches from the tip of the tool to the free surface of the workpiece, and the secondary deformation zone involves the tool-chip interface (Stephenson and Agapiou, 2006).

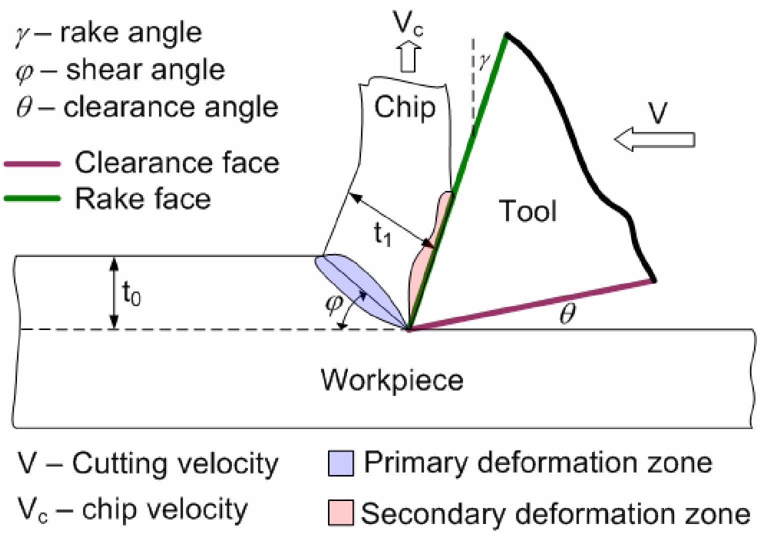

Figure 1.1 Orthogonal Machining process

The workpiece materials in cutting can either be ductile materials such as steels, iron, copper etc. or brittle materials such as glass, ceramics etc. Ductility, in the conventional sense, describes the ability of the material to be drawn into wires or its ability to deform plastically without fracturing; it is measured as elongation or reduction in cross sectional area in a tensile test. This property is very critical in all of the material removal processes as it dictates the way the material removal takes place. From a machining standpoint ductile materials usually produce continuous chips leading to a

fracture free (smooth) surface finish. The other class of materials, called brittle materials, produces discontinuous chips characterized by fracture in the surface leading to undesirable surface finish. In order to overcome issues relating to surface finish in brittle materials, it is desirable to machine them in a way that chips are formed during machining thus leaving a crack-free surface post-machining. This process, known as ductile-regime machining, is the focus area of this thesis. In order to achieve high quality surfaces many machining techniques including precision (micro-machining) and ultraprecision (nanotechnology) machining are currently being employed.

1.2 Precision and Ultraprecision Machining

The development of achievable machining accuracy over the years has given rise to new classes of machining processes such as precision and ultraprecision machining. Taniguchi (1983) summarizes the progress of accuracy in machining as shown in Figure 1.2. The processes of precision and ultraprecision machining have advanced in terms of achievable accuracy to the extent that nanometer level accuracy has been reached and efforts to improve the accuracy to the sub-nanometric levels are gaining momentum.

In the field of micro-cutting the range of dimensions investigated is between 1–200 μm with some variation among different methods (Masuzawa and Tonshoff, 1997). Since the scale of micro-cutting is in the micrometer regime, the process can be interpreted in two ways: (i) utilizing conventional scale machine tools to produce micro scale features and parts (Figure 1.3) and (ii) utilizing miniaturized machine tools to manufacture micro scale parts, features and dimensions (Figure 1.4). Highly precise and accurate conventional size machine tools have been shown to be useful for producing

microscale features such as micro-grooves, micro lens arrays, and high quality surfaces in silicon wafers etc as shown in Figure 1.3.

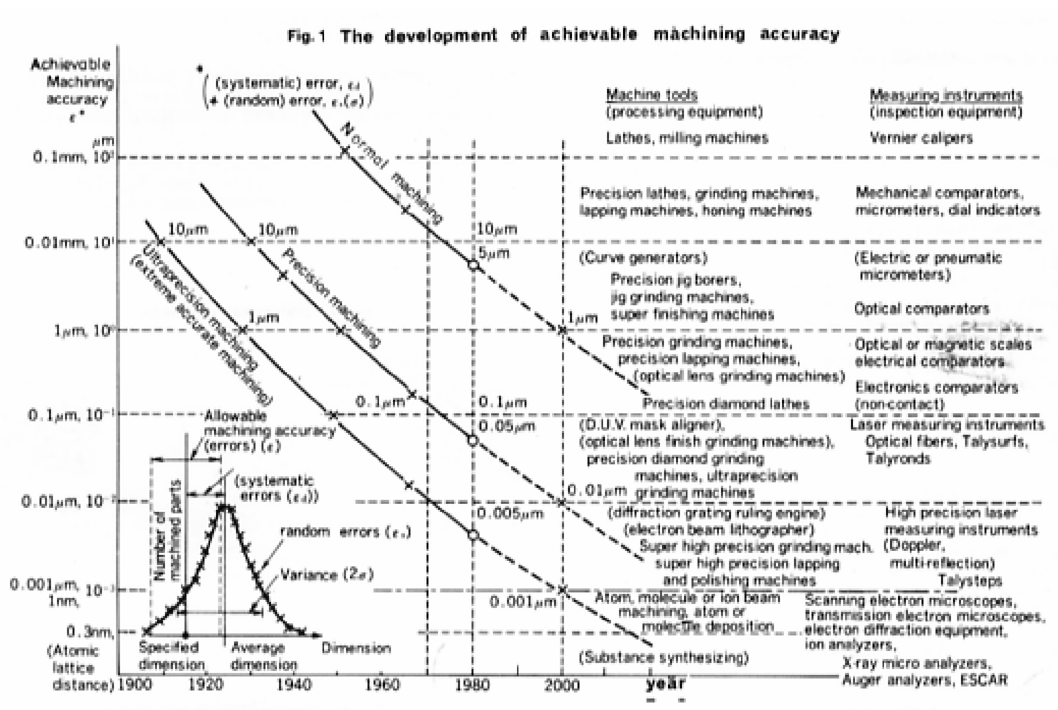

Figure 1.2 The development of achievable machining accuracy (Taniguchi, 1983)

In order to reduce the power consumption and the ratio of the size of the machine tool to the produced feature size, miniaturization of machine tools has occurred. This trend has led to the development of microfactories (Okazaki et al., 2004) which typically are comprised of a set of machine tools such as micro-lathe, micro-milling machine, micro-EDM, micro-press etc as shown in Figure 1.4. Applications for micromachining have been growing over the years and hence have received widespread attention from researchers and industry alike. Some of the feasible products, systems and applications include prosthetic devices, ingestible or implantable “smart pills” which have sensors and are combined with dose regulating drug dispensers, silicon connectors for repairing blood

vessels in biological systems, catheter-based medical diagnosis and therapies, flexible fiber-optics-based imaging systems, photonic components and systems assembly, micro-optical systems micro-electronics, electronic fuel injectors for automotive engines, data storage systems (McKeown, 1996), micro- holes, pins, slits and grooves, micro-features in IC devices, fuel cells, cells and tissue handling devices in bio-technology, micro-molds etc. (Masuzawa, 2000).

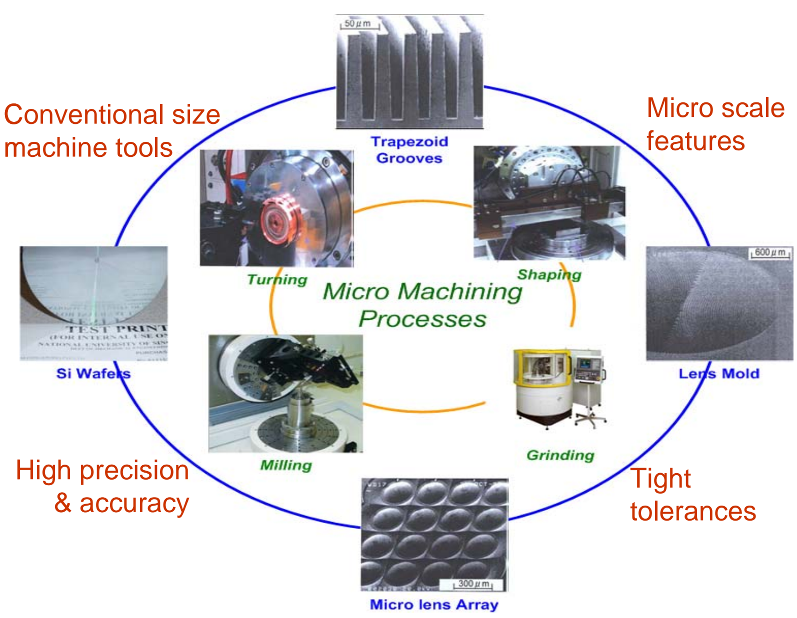

Figure 1.3 Micromachining utilizing conventional size machine tools (Ehmann et al., 2007)

Ultraprecision machining deals with feature sizes on the order of 0.1 – 100 nm and includes processes such as single point diamond and CBN cutting, multi-point fixed abrasive processes such as grinding, honing, belt polishing etc., free abrasive processes such as lapping, polishing etc., chemical processes such as etch machining (McKeown, 1996). The process of single point diamond turning has become an effective method for producing mirror-like surface finishes in components for the optical and semiconductor

industries. It is especially attractive for machining brittle materials such as silicon, germanium, silicon carbide, silicon nitride, glass etc. to produce high quality surfaces by removing chips in a ductile manner. This process has come to be known as ductile-regime machining.

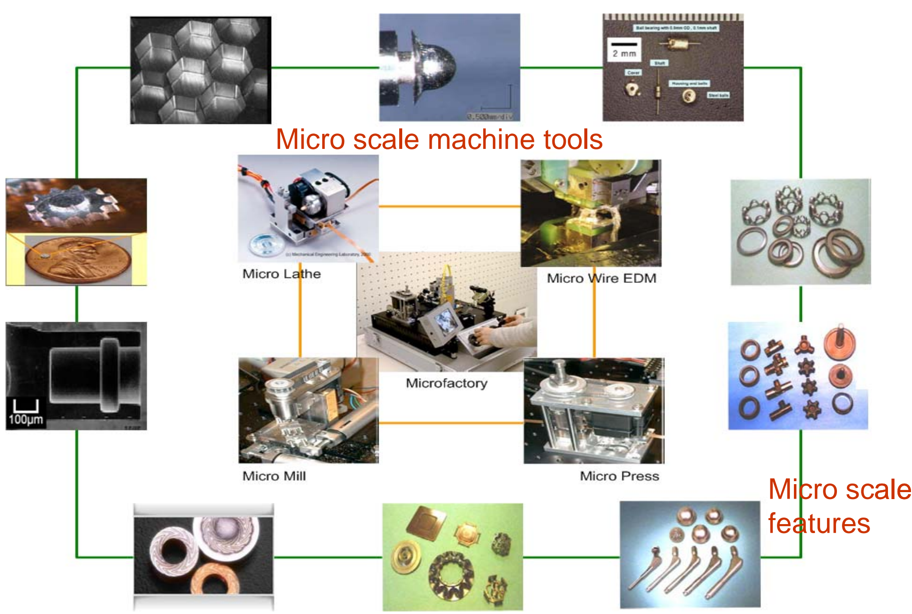

Figure 1.4 Micromachining utilizing miniaturized machine tools and microfactories (Ehmann et al., 2007)

1.3 Ductile-Regime Machining

Brittle materials such as silicon, germanium, glass, ceramics etc. have numerous applications in a wide variety of fields. The applications range from producing micro-wafers, aspherical lenses for camera equipment and optical instruments to manufacturing bone replacements using ceramics. In comparison to other ultraprecision machining processes such as polishing, lapping etc., ductile-regime machining is both cost effective and less time consuming (Fang et al., 2003).

The process of ductile-regime machining is typically carried out on an ultraprecision diamond turning machine and can be described using Figure 1.5. The depth of cut is increased in a plunge cut from left to right in Figure 1.5 and the surface quality and chip formation are observed. There are three distinct zones formed as the tool traverses across the workpiece: (i) a ductile zone where the chip formation is continuous and the surface is free from any defects such as micro-cracks, craters etc. (ii) a ductile-brittle-transition zone which features a semi-brittle fractured surface and (iii) a brittle fractured surface which features holes, cracks and severe surface damage (Liu K. et al., 2004). It can be observed that there is a certain depth at which a ductile to brittle transition occurs, and this particular depth depends on process parameters, workpiece material properties and tool geometry.

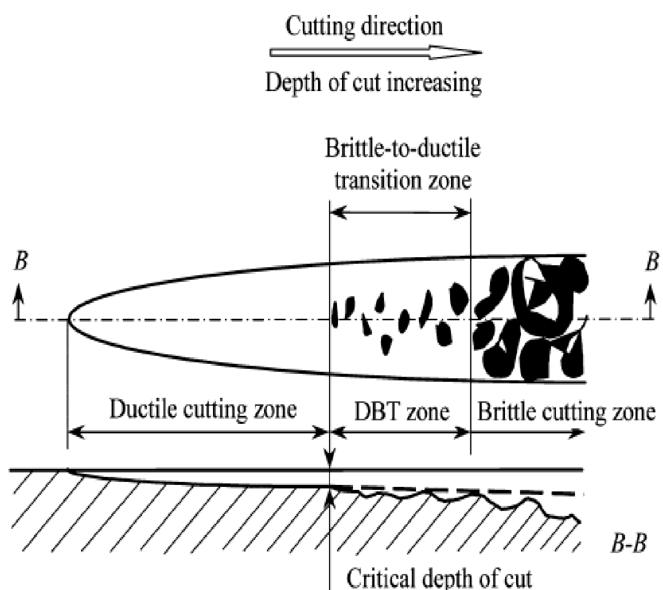

Figure 1.5 Schematic of ductile-regime machining (Liu et al., 2004)

The process parameters (depth of cut, feed etc.) to achieve transition between ductile and brittle modes of material removal has been reported (Blackley and Scattergood (1991), Blake and Scattergood, (1990), Patten et al., (2005), Yan et al., (2002)) to be in the micrometer and nanometer regime. Hence ductile-regime machining is categorized as a precision or ultra-precision machining process. The main goal of this thesis is to evaluate the transition undeformed chip thickness (depth of cut in turning) for different materials based on certain given input conditions.

1.4 Objectives and Research Plan

With the ever increasing number of applications of brittle materials in a variety of fields, the process of machining brittle materials has gained significant importance over the last decade. The process of ductile-regime machining has been extensively studied by performing experiments on different brittle materials such as silicon, germanium, silicon nitride, silicon carbide etc. These experiments have addressed issues of surface integrity and its dependence on crystallographic orientation. The transition undeformed chip thickness has been identified as a key parameter in the ductile-regime machining process. The procedure of predicting the transition undeformed chip thickness has not been studied extensively. One model suggests that the transition undeformed chip thickness is dependent on material properties such as hardness, fracture toughness and elastic modulus. Another models suggests the use of finite element analysis technique which can be time consuming and computationally expensive. The effect of microstructure, tool geometry and workpiece material properties are important issues that need to be considered. The objective of the current research is to develop a comprehensive model to

predict the transition undeformed chip thickness for ductile machining of brittle materials by considering the above mentioned issues. The input parameters are the cutting conditions and material properties of the workpiece and tool. The predictive model is validated through a set of experiments.

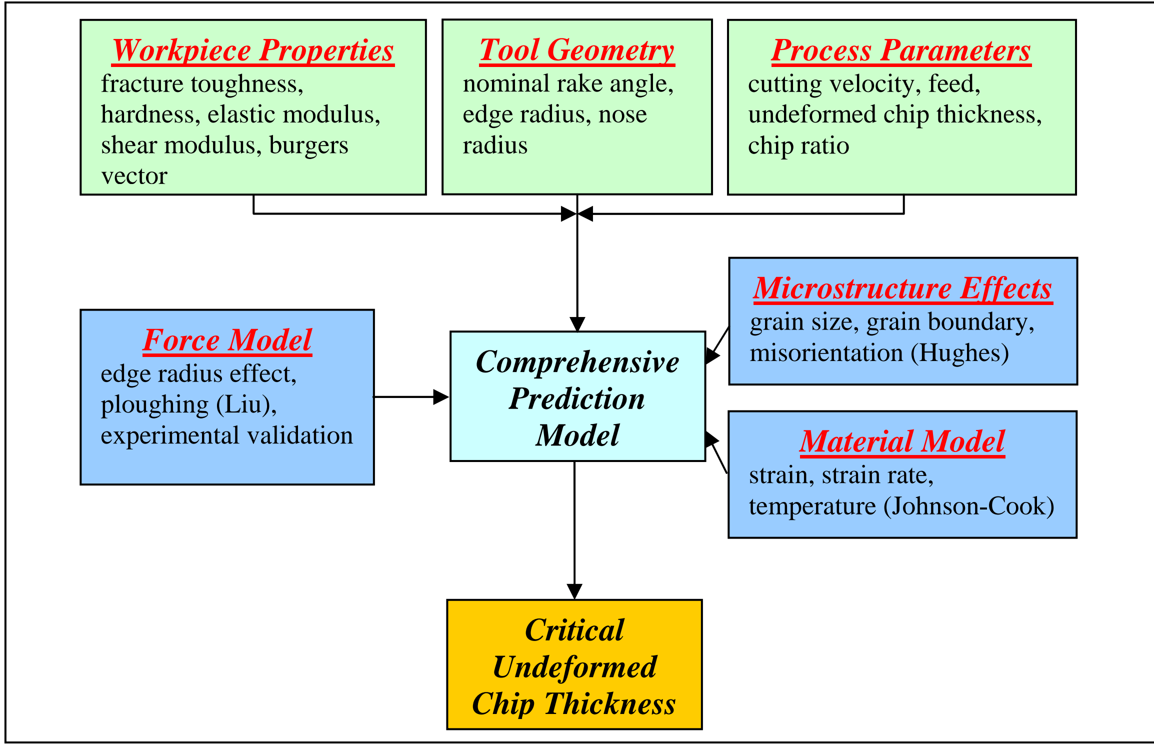

Figure 1.6 Outline of research plan

The outline of the research plan is given in Figure 1.6. The comprehensive prediction model takes workpiece material properties, tool geometry parameters and process conditions as its input. The workpiece materials considered in this work are silicon, silicon carbide and germanium. The material properties of interest include elastic modulus (E – Young's modulus), shear modulus (G), hardness (H), fracture toughness (K_{Ic}) and burgers vector (b). The tool geometry parameters of interest include the nominal

rake angle and tool nose radius, which are usually a part of the tool specification, and tool edge radius. The input process conditions include the cutting velocity, feed, undeformed chip thickness and the chip ratio.

The comprehensive prediction model includes the force model, microstructure effects model and the material constitutive model. The force model takes into account the forces due to chip formation and ploughing. The prediction is validated using a set of cutting experiments. The microstructure effects model considers the effect of grain size, grain boundary and crystal orientation on the flow stress of the material. The material constitutive model takes into account the strain, strain rate and temperature that are generated by the cutting action.

The output of the prediction model is the transition undeformed chip thickness necessary for ductile mode cutting of the given brittle material. The model prediction is validated through a series of experiments under different cutting conditions.

The predictive model would support the determination of the cutting conditions for micro-machining a brittle material in ductile manner without resorting to trial and error and thereby enhancing productivity.

1.5 Thesis Organization

The thesis begins by reviewing the past and present literature on force modeling, ductile-regime machining, microstructure effects on process parameters, and other related research such as molecular dynamics and high pressure phase transformation (Chapter 2). The comprehensive predictive model is detailed for single crystal silicon along with experimental validations (Chapter 3). A model for the effects of microstructure on

process parameters including cutting and thrust forces for polycrystalline materials such as germanium and silicon carbide (Chapter 4) is presented. Finally conclusions of this research and recommendations for future work are presented (Chapter 5).

CHAPTER 2

LITERATURE REVIEW

Ductile-regime machining is a relatively new area of research that has provoked substantial interest over the last two decades. In order to develop the proposed predictive model several aspects of machining are required which would aid in better understanding of the mechanics of ductile-regime machining. Some of the aspects covered in this review include force modeling, process of ductile-regime machining, effects of microstructure on flow stress, material constitutive model and high pressure phase transformation.

2.1 Force Modeling

The procedure for modeling forces in cutting operations has been well documented over the years. The earliest model of the cutting process was developed by Piispanen (1937, 1948) and is known as the card model. This model depicts the material as a deck of cards sliding over one another as the tool moves relative to the workpiece. Though the model had a lot of simplifying assumptions, it captured the central concept of the cutting process. Merchant (1945) developed a model of the force system in the cutting process and determined useful equations to describe the mechanics of the process. The model assumed the tool to be perfectly sharp and derived an analytical relationship for various parameters such as cutting and thrust forces, shear angle, friction coefficient, etc. A simple view of the model is presented in Figure 2.1. Bitans and Brown (1965) studied the forces in orthogonal cutting using a wax workpiece. The deformation grid was studied for various machining conditions and a linear relationship between the shear, rake and

friciton angle was found. Yellowley (1987) suggested a simple predictive model for orthogonal cutting using a boundary equilibrium approach by considering the chip moment. Oxley (1989) proposed an iterative model based on slip-line analysis to predict various parameters involved in the metal cutting process.

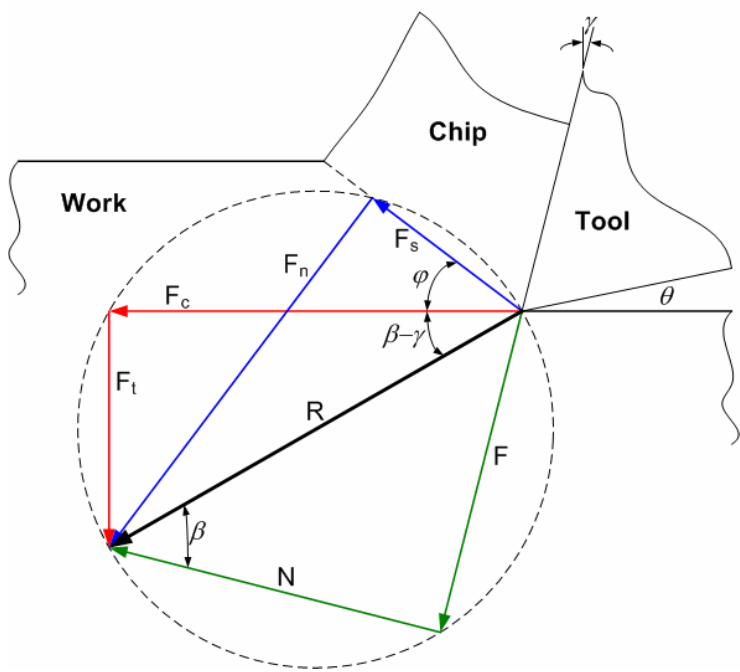

Figure 2.1 Composite cutting force circle (Merchant, 1945)

The advent of micro machining brought out the inherent issues in the models that used sharp tool assumption to predict various process parameters (Liu X. et. al, 2004). This led to the development of newer theories, some of which are discussed herein. The bluntness associated with the tool edge created a 'ploughing' action which was different from the shearing, which is the primary mode of chip formation. Ploughing is considered to be a plastic deformation process where there is displacement of asperities between the

two interlocking surfaces. Researchers argued that the total force or specific cutting energy had contributions both from the shearing action and the ploughing action.

Albrecht (1960) was one of the earliest to attempt to model and express the ploughing forces as separate entities as shown in Figure 2.2. The tool portion of this diagram has two resultant forces, one along the rake face and the other along the rounded portion of the tool. Using these two resultant forces, Albrecht modified the Merchant equations to include the effects of ploughing. Wallace and Boothroyd (1964) use an approach similar to Albrecht in assuming two resultant forces along the tool-chip interface. They also consider sliding and sticking friciton at the tool-chip interface and report that the coefficient of friction in the sliding region is constant and the frictional stress in the sticking region is constant.

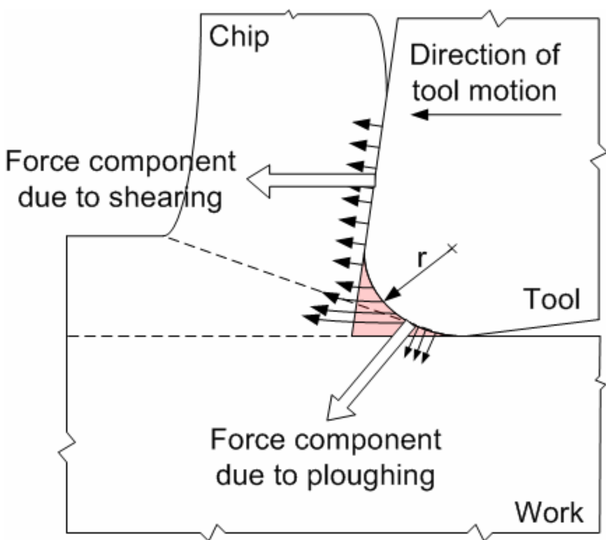

Figure 2.2 Force components in cutting with a rounded tool edge (Albrecht, 1960)

Hsu (1966) used the method of extrapolation to determine the forces due to ploughing and cutting action. The extrapolation is carried out using the plot of the cutting

forces vs. depth of cut. An ordinate is drawn at a distance equal to r (1+sinγ), where r is the tool edge radius and γ is the rake angle, from the origin. The point of intersection of the ordinate with the cutting and thrust forces gives the magnitude of the ploughing forces. This theory assumes that the ploughing force does not change with variation in depth of cut.

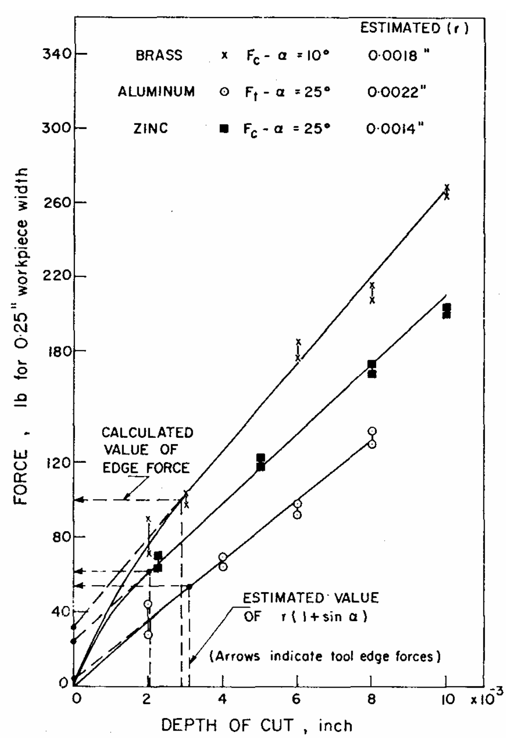

Figure 2.3 Extrapolation method to determine ploughing forces (Abdelmoneim and Scrutton, 1974)

Abdelmoneim and Scrutton (1974) model the cutting forces by assuming that the tool edge is subject to two simultaneous but independent actions (assuming no built-up edge) viz., a rubbing and a cutting action. By examining the energies expended during both rubbing and cutting actions, the total force is expressed as the sum of the two forces. The authors also note that extrapolating the force vs. depth of cut plot to derive the

ploughing forces may lead to erroneous results. The ploughing forces are represented by the force ordinate corresponding to the value of depth of cut for which a departure from linearity is observed as shown in Figure 2.3.

Connolly and Rubenstein (1968) attempted to model the forces in the cutting and tangential direction by performing a force balance on the lower boundary of the primary deformation zone (Figure 2.4a), which is an idealized contour under certain assumptions. The presence of tool edge radius also contributes to the change in rake angle (Figure 2.4b) and the flow pattern (Figure 2.4c) as shown. Manjunathaiah and Endres' (2000) model is based on the same concept as the Connolly model, but attempts to express both the cutting and ploughing forces in terms of the tool edge radius.

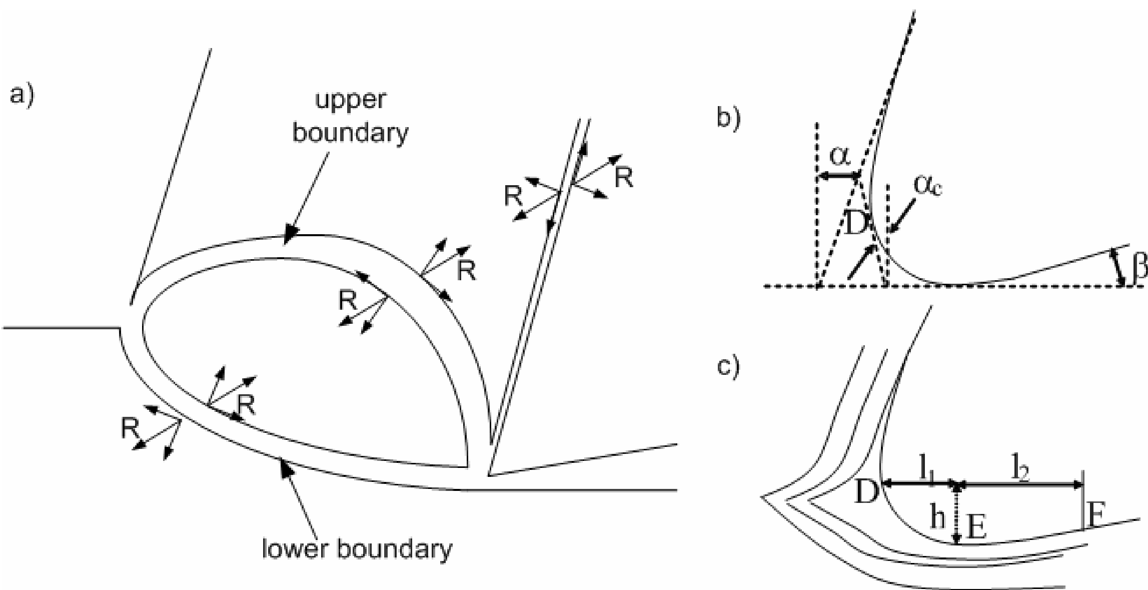

Figure 2.4 (a) An equilibrium system of forces acting in the deformation zone (b) Equivalent rake angle due to tool edge radius (c) Flow pattern of workpiece approaching tool with finite radius (Connolly and Rubenstein, 1968)

Waldrof et al. (1998) and Waldrof (2004) model the cutting and ploughing forces using the slip-line field analysis. The author considers two scenarios: one where the

material flow has a point of separation at the tool edge, and the other where there is a stable built-up edge formed during the cutting action. The author suggests that the formation of a built-up edge is the more likely scenario, as the predictions match well with observed trends. Fang's (2003) model of machining with a rounded edge tool consisted of dividing the slip-line region into 27 different sub-regions and attaching a physical significance to each one of them. The model by Liu K. et al., (2001) considers an infinitesimally small cutting edge and expresses the forces as a function of the material properties and tool geometry. The total force acting on the tool is then derived by summing up all the elements that make up the tool. This model, however, does not attempt to separate the cutting and the ploughing contributions to the total forces. Liu's model for computing cutting and thrust forces is adopted in this thesis work. Other efforts in the field of force modeling using different approaches include Kim et al., 1995, Endres et al., 1995, Schimmel et al., 2002, and Kishawy et al., 2006.

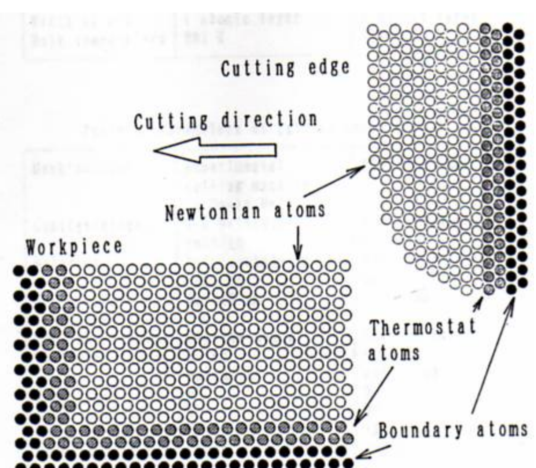

Figure 2.5 Schematic model of micro-cutting for molecular dynamics simulation (Shimada et al., 1992)

A more recent technique in the study of mechanics of micromachining involves the use of molecular dynamics (MD) simulation. Shimada et al. (1992) conducted a MD analysis (Figure 2.5) of the nanometric chip removal process in micro-cutting and compared the cutting forces, specific energies and chip morphologies with experimental results, obtaining good agreement. The experiments were conducted on OFHC-Cu using a diamond tool of 20 nm edge radius. They further discuss the applicability of the MD approach to the analysis of thermal field in metal cutting. Ikawa et al. (1992) also performed MD analysis for micro-cutting copper using a diamond tool and studied the effect of tool edge radius and minimum undeformed chip thickness on the chip formation process. They corroborated their results with cutting experiments and found that there was continuous chip formation for undeformed chip thickness values of 1nm and 20 nm (Figure 2.6).

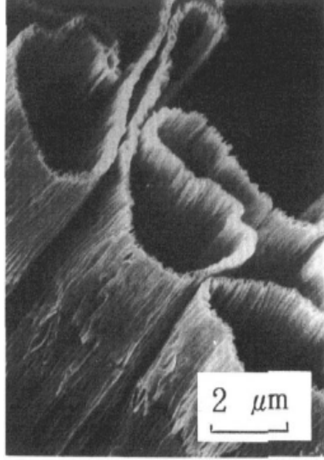

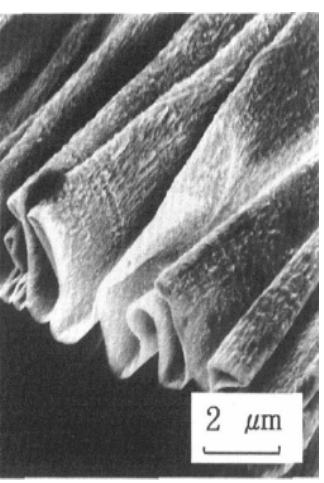

Figure 2.6 Chip formation in nanometric cutting of copper with nominal thickness of cut of 1 nm (left) and 20 nm (right). (Ikawa et al., 1992)

Komanduri et al. (1998) performed MD simulation to study the effects of tool geometry in nanometric cutting. The authors found that the ratio of the depth of cut to the tool edge radius did not have any influence on the cutting force or the specific cutting energy as long as the ratio was held a constant. In other words, the effect of the edge radius and depth of cut on cutting force and specific cutting energy can be separated. Tanaka et al. (2004) analyzed the ductile-brittle transition in monocrystalline silicon using three point bending simulations. Cai et al. (2007) investigated the mechanism of nanoscale ductile mode cutting of single crystal silicon using MD analysis. They analyzed the cutting and thrust forces and the stresses in the chip formation zone for very small values of undeformed chip thickness (2-4 nm).

It should be mentioned here that the specific cutting energy increases with a decrease in the undeformed chip thickness; this is commonly referred to as the "size-effect" (Figure 2.7). There are many theories explaining the reasons for the existence of the size effect. Among them are the effect of tool edge radius that causes ploughing, material strengthening effects, subsurface plastic deformation and material separation (Subbiah, 2006).

Force modeling is integral to all machining processes as it provides information on the energy consumed during the process and tool wear due to forces acting on the tool. From the discussion on force models, it is evident that many proposed approaches have been shown to be effective for micro-machining. One such approach proposed by Liu. K (2002) is adopted in this research to model the cutting and thrust forces. It must however be pointed out that the issue of friction at the tool-chip interface, especially for brittle materials, requires deeper understanding as it plays a vital role in the force variations and

tool wear. It must also be understood that the process of ductile-regime machining involves removal of material through plastic deformation (as opposed to brittle failure), and therefore the models described above are well suited for this process.

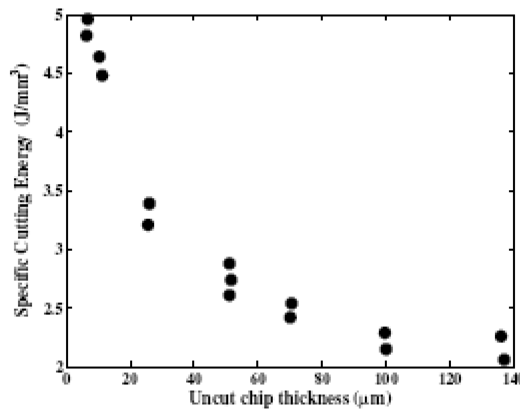

Figure 2.7 Size effect in metal removal process (Subbiah, 2006)

2.2 Tool Edge Radius Measurement

One of the most important parameters in micro-cutting is the tool edge radius, as can be deduced from the above discussion. The process of measuring the edge radius of a tool has been a challenge, yet there is no accepted technique to perform these measurements. Sarwar and Thompson (1982) used an optical projection technique to determine the cutting edge radius, which in their experiments was as large as 558 μm (a very blunt tool). This, however, may not be viable for very small values of tool edge radii. Drescher (1993) described a scanning electron microscopic (SEM) technique for imaging the tool edge of a diamond tool. The process involves creating a contrast using beam contamination effects to obtain accurate edge geometry. It involves three steps in the measurement process with (i) edge perpendicular to scan direction, (ii) edge parallel to scan direction and (iii) edge tilted at 45° to the scan direction. The image thus obtained

can be processed to determine the accurate edge radius. A sample image of this process is shown in Figure 2.8 for which the edge radius was 370 nm. Asai et al. (1990) used an SEM with two secondary electron detectors to measure the edge radius. The shape was determined from the difference in the SEM image signals. The range of the values in their measurements was 10-60 nm. Evans et al. (1987) used a “shadow evaporation” technique to determine the tool sharpness. The procedure is to use the tool as an indenter on polished gold. Once the indentation is performed, micro spheres are located in the groove. Then a well collimated beam is shadow-evaporated past the sphere and the shadow is examined to determine the tool edge profile. Gao et al. (2006) developed an instrument that contains an AFM unit with an optical sensor for alignment and a laser diode to measure the nanometer edge profile of diamond cutting tools. The profiles measured using this instrument were 92 nm for the new tool and 219 nm for the worn tool.

Li et al. (2003b) proposed a non-destructive nano-precision method to determine the tool edge radius of a diamond tool. According to this method, the profile of the tool is first copied by indenting it on a selected material. The indentation profile is then scanned using an atomic force microscope (AFM) from which the tool edge radius can be determined. The method also compensates for the elastic recovery of the indented material to cancel the elastic spring-back. The range of values for the edge radius of the tool measured in this process was 45-647 nm. Li’s method of tool edge radius determination is used in this research work.

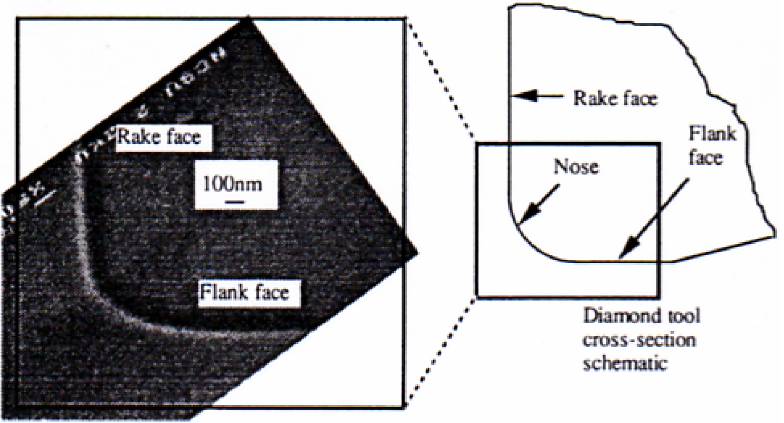

Figure 2.8 SEM image showing the line of contamination as the edge profile (Drescher, 1993)

Subbiah (2006) used a stylus profilometer trace to measure the edge radius of the tool which was in the range of 12.5-75 µm. Venkatachalam and Liang (2007) used an image digitization technique to qualify the edge radius (~7 µm) of a grooving tool. The tool edge radius is first captured as an image using an optical microscope. The image is then digitized to obtain data from the tool edge which is then processed to obtain the edge radius by fitting a least square circle to the data set (Figure 2.9).

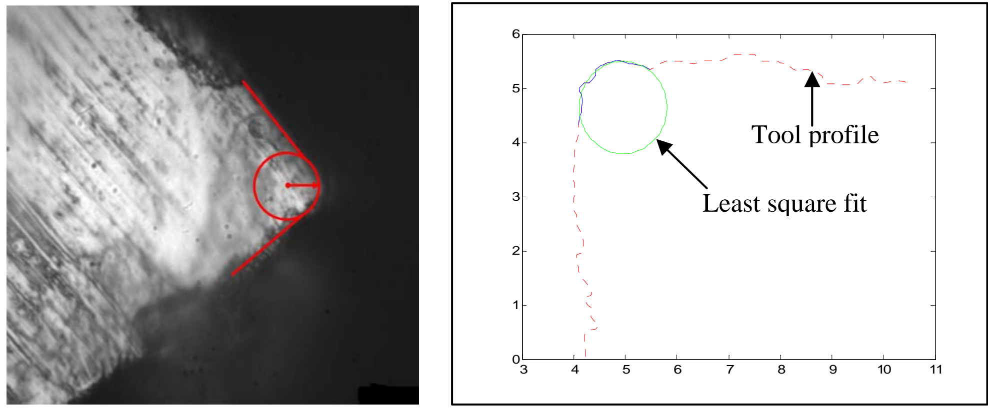

Figure 2.9 Optical image and least square fit to determine tool edge radius (Venkatachalam and Liang, 2007)

2.3 Ductile-Regime Machining

Ductile-regime machining, as stated before, is a special class of ultraprecision machining usually performed on an ultraprecision lathe with a diamond cutting tool. The process of cutting brittle materials to produce continuous chips, thereby producing a crack free surface, is termed ductile-regime machining. This process is very important in many industries utilizing brittle materials and requiring high quality surface textures. The deformation of brittle materials plastically under certain process conditions has been reported by Huerta and Malkin (1976), Moore and King (1980), and Tow and McPherson (1986). The machining of brittle materials in the ductile regime is not restricted to turning and shaping at the micro-scale, but has also been reported for micro-grinding (Bifano et al., 1991).

2.3.1 Modeling

Lawn et al. (1976) were among the earliest to report a critical depth while indenting a hard material, where the critical depth represented the transition from a failure characterized by plastic deformation to a failure characterized by fracture. They employed standard indentation tests to study the degree of brittleness. The authors determined a relation between the material properties and critical dimensions for a brittle material, such as crack length (c) and indentation length (a), for an indentation test (Figure 2.10a). The characteristic dimension (a) of the residual impression left by the indenter due to a load P is given by following relation:

$$P / a^2 = \alpha \pi H \quad (deformation) \tag{2.1}$$

where H is the hardness of the material, and α is the characteristic constant of the indenter. The crack propagation length (c) due to fracture is given by the following relation:

$$P/c^{3/2} = (2\Gamma E/\kappa)^{1/2} \quad (fracture) \tag{2.2}$$

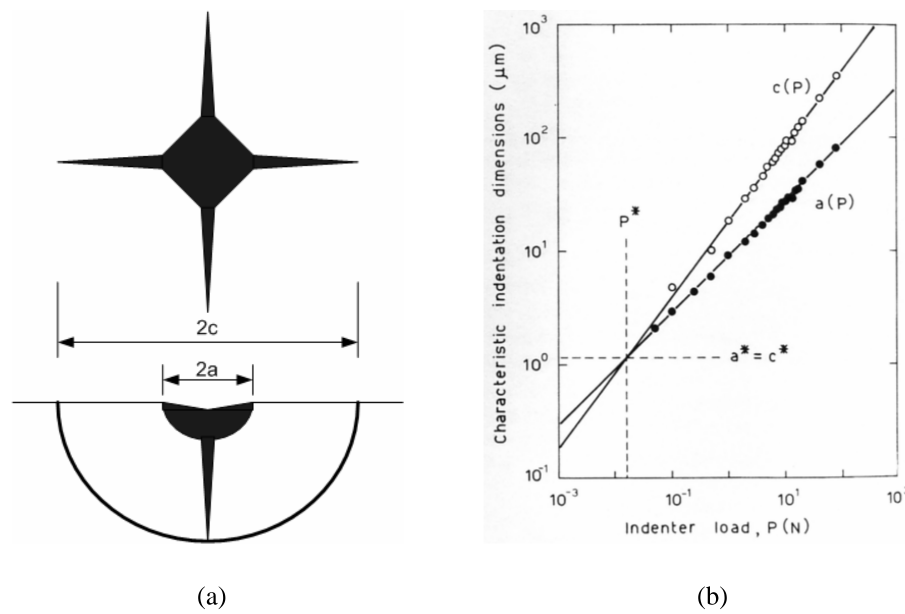

(a) (b)

Figure 2.10 a) Indentation pattern showing lateral crack (top) and median crack (bottom) for Vickers indentation test b) Vickers indentation data on soda lime glass (Lawn et al., 1976)

The relations in (2.1) and (2.2) are plotted as shown in Figure 2.10b. The intersection point in the plot can be thought of as the critical depth of indentation and is given by the following relation:

$$a^* = \xi \frac{\Gamma E}{H^2} = c^* \tag{2.3}$$

where Γ is the fracture surface energy and ξ is a dimensionless geometry factor.

Blake and Scattergood (1990) presented the ductile brittle transition concept in terms of material removal energy. According to the theory, the ratio of the plastic flow energy to the fracture energy is proportional to the depth of cut (d). As the value of d decreases, the material removal by plastic flow become more favorable compared to fracture. The authors derived a relation (similar to Lawn et al., 1976) for critical depth of penetration (t_c) of indenter for crack initiation as shown in (2.4).

$$t_c = \Psi \frac{E}{H}\left(\frac{K_{Ic}}{H}\right)^2 \tag{2.4}$$

where K_{Ic} is the fracture toughness, E is the modulus of elasticity, H is the material hardness and Ψ is a dimensionless constant dependent of indentation geometry. It was also observed that the chips were not removed in a completely ductile manner, but rather by a combination of plasticity and microfracture.

Blackley and Scattergood (1991) also proposed a relation for the critical chip thickness at the point of transition. They also derived a relation for the maximum tool feed at which the ductile-to-brittle transition moves onto the plane of cut. The critical chip thickness (d_c) and the surface damage depth (y_c) are related to the tool feed (f), tool nose radius (R) and the location of ductile-brittle transition (Z_{eff}) as given by the following relation (Figure 2.11):

$$\frac{Z_{eff}^2 - f^2}{R^2} = \frac{d_c^2}{f^2} - 2\left(\frac{d_c + y_c}{R}\right) \tag{2.5}$$

The relation for maximum feed (f_{max}) is given in (2.6).

$$f_{\max} = d_c \sqrt{R} \sqrt{\frac{1}{2(d_c + y_c)}} \qquad (2.6)$$

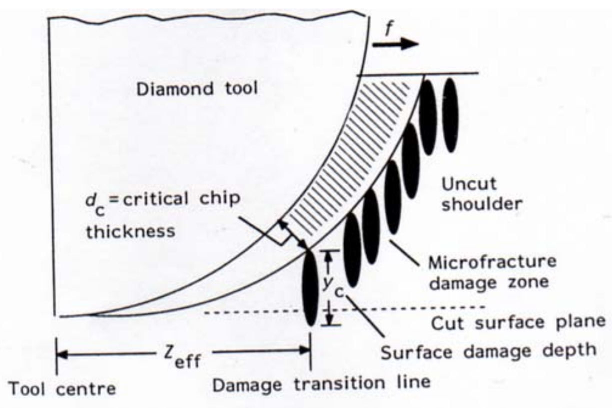

Figure 2.11 Machining geometry used to derive cutting model (Blackley and Scattergood, 1991)

Bifano et al. (1991) adopted a similar procedure for modeling the critical depth in micro-grinding. The authors validated the model given by (2.4) for various brittle materials using the micro-grinding process. Ueda et al. (1991) adopted a J-integral approach to determine the material removal mechanics involved in the microcutting of ceramics. The J-integral around a crack ahead of the cutting edge is formulated using the finite element method. The authors suggest that if the value of J-integral exceeds a critical value (J_c), which is a material property, then the failure is through fracture; otherwise it is through plastic deformation. A summary of their results is shown through a domain diagram as in (Figure 2.12). Liu and Li (2001) conducted a theoretical and experimental study on the ductile cutting of tungsten carbide. The theory was based on the analysis of cutting forces, cutting geometry and fracture mechanics. The results from

the experiments for ductile cutting of tungsten carbide showed a critical depth of cut of 4.76 μm.

The mechanics of ductile regime machining requires a deeper understanding than represented by the approach suggested by Blake and Scattergood (1990), which defines the critical chip thickness as a simple function of material properties. The process parameters and tool geometry are important factors in ductile-regime machining which need to be considered. The approach proposed by Ueda involves using FEM analysis which is time consuming and cumbersome. This thesis proposes a closed-form analytical model to determine the transition undeformed chip thickness for ductile-regime machining process, which can be beneficial in reducing production time and enhancing productivity.

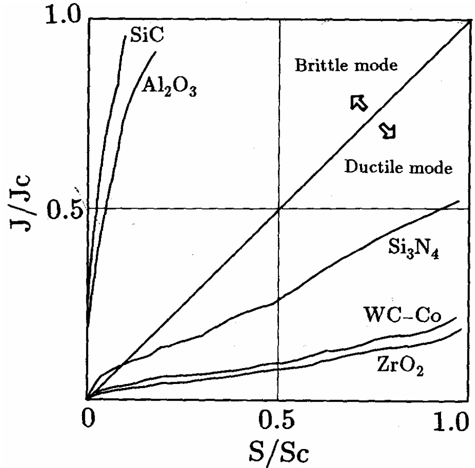

Figure 2.12 Domain diagram for brittle/ductile mode transition at low cutting speed and t = 2 μm (Ueda et al., 1991)

2.3.2 Experimental Investigations

The process of ductile regime machining has been experimentally studied on a variety of different materials. Single crystal silicon (Si) has been the most widely researched material because it forms the backbone of the semiconductor industry. The other materials researched are germanium (Ge), silicon carbide (SiC), glass etc.

Single Crystal Silicon: Fang and Venkatesh (1998) demonstrated diamond cutting of silicon in order to achieve surface finish to the order of tens of nanometers. They report a critical depth of cut of 236 nm for single crystal silicon for ductile-brittle transition that was obtained by using a plunge cut experiment. Leung et al. (1998) experimentally demonstrated the possibility of ductile-regime machining of single crystal silicon under different cutting conditions including using a cutting fluid. They reported a surface finish in the order of 2.86 nm. Patten and Gao (2001) investigated nano-cutting of silicon using a single point diamond tool under extreme negative rake angles (-85°). The cutting was carried out with both the rake and the clearance face resulting in a smooth ductile finish. Chao et al. (2002) used face turning experiments with a slightly tilted workpiece to determine the transition based on the measured surface roughness. Yan et al. (2002) evaluated the feasibility of ductile-regime machining of silicon using large tool feeds. Their results indicate that the tool feed could be as high as 5-20 μm/rev. A sample of the surface generated and chips formed at 5 μm/rev feed is shown in Figure 2.13.

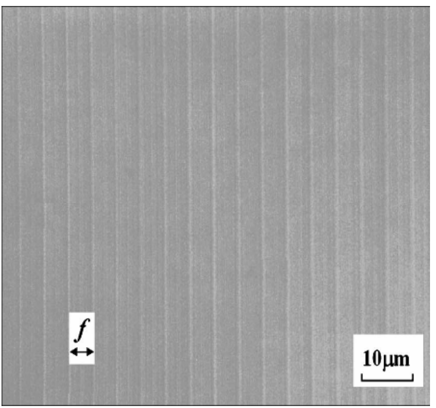

Figure 2.13 Surface generated and chip formation in single crystal silicon ductile machining (Yan et al., 2002)

Yan et al. (2003b) developed a ductile machining system based on the straight line enveloping method to fabricate convex axisymmetric aspheric surfaces on hard brittle materials. A surface was generated on single crystal silicon using a straight nosed diamond tool and a roughness value of R_a = 16 nm was obtained. Fang and Zhang (2003) studied the effect of tool edge radius on cutting single crystal silicon. The results show that ductile cutting can be achieved by varying the cutting edge radius and undeformed chip thickness, which consequently varies the effective rake angle.

Single Crystal Germanium: Blake and Scattergood (1990) performed ductile cutting experiments on single crystal germanium and found that the critical chip thickness for germanium was less than that of silicon. They also reported microstructure damage to the surface termed as pitting. Blackley and Scattergood (1991) also experimentally investigated ductile cutting of germanium and also studied the effect of rake angle and tool edge radius on the critical chip thickness. Yan et al. (2004a) conducted an experimental study of the ultraprecision ductile machinability of single crystal germanium.

Other materials: Sreejith (2005) reported ductile machining experimental studies for hot isostatically pressed silicon nitride and found that ductile cutting was possible at higher speed and negative rake angles. Patten et al. (2005) reported ductile nanomachining for single crystal silicon carbide. The formation of chips for penetration depths under 500 nm has been reported, and the reason for such a behavior has been attributed to high pressure phase transformation. A similar study was reported by Bhattacharya et al. (2006) for single point turning of CVD coated silicon carbide. Moriwaki et al. (1992) presented a method for ductile cutting of glass that is assisted by ultrasonic vibration applied in the cutting direction. The maximum effective depth of cut is given to be a function of the tool edge radius, the feed rate and the depth of cut. In this investigation vibration assisted cutting increases the critical depth of cut by about seven times when compared to conventional cutting. This may be because the profile of the tool is better transferred on to the workpiece during vibration assisted cutting. Schinker (1991) studied subsurface damage mechanisms for high-speed ductile machining of optical glasses and concluded that low depths of cut and rates of feed, in addition to extremely low vibration amplitude are necessary for ductile mode removal in glasses. Yan et al. (2004b) demonstrated single point diamond turning of calcium fluoride (CaF_2) to produce surfaces with nanometric finish. Nakasuji et al. (1990) performed diamond turning of brittle materials such as silicon, germanium and lithium niobate ($LiNbO_3$). They found transition in some areas but with no specific orientation for lithium niobate, but concluded that ductile cutting of this highly brittle material required a vibration-free machine tool and low thickness of cut. Jasinevicius (2006) reported indentation and diamond turning experiments for materials such as gallium arsenide (GaAs) and indium antimonide (InSb). It was found that InSb

was very favorable for ductile cutting at feeds ranging from 1.25 – 7.5 μm/rev. However, GaAs showed predominantly ductile response only for the lowest feed rate. Bifano et al. (1991) reported ductile regime grinding results for various materials such as fused silica, soda lime glass, zerodur, quartz, zirconia, germanium, silicon and silicon carbide. Yoshino et al. (2005) developed a machining device to carry out precision machining experiments under external hydrostatic pressure. The authors performed cutting experiments on soda glass, quartz and silicon under hydrostatic pressure. The application of external hydrostatic pressure suppresses the brittle response in ductile mode cutting as it minimizes cracking tendency and chipping.

Polycrystalline Brittle Materials: The process of ductile cutting of polycrystalline materials has not been widely reported as single crystal materials. The obvious reason for this trend is the fact that single crystal materials are homogeneous in their structure and more amenable to cutting. Polycrystalline materials introduce crystallographic anisotropy which limits the quality of the surface being machined in that it introduces non-uniformity. Liu et al. (2003) studied the ductile cutting of tungsten carbide (WC) and demonstrated a transition from ductile mode of cutting to the brittle mode as the undeformed chip thickness was increased. Yan et al. (2006) conducted ductile cutting experiments using a sharp nose diamond tool on polycrystalline germanium. The cutting was performed on three grains and the surface finish and forces were monitored. It was found that forces and surface roughness values were different for the three grains as the tool passed over the workpiece. It was also reported that uniformly ductile-cut surfaces were produced by using an extremely small undeformed chip thickness value of around

80 nm. Bhattacharya et al. (2005) performed ductile machining on polycrystalline silicon carbide and reported a phase transformation of the material below the tool. Additionally, the authors report that ductile cutting of polycrystalline silicon carbide is possible at penetration depths of 10 to 25 nm.

From the above discussion on the experimental investigations, it is evident that a substantial number of brittle materials have been successfully machined through ductile-regime machining, which bodes well for the future of this process. Although experiments are an effective means of studying material response, it must be emphasized that a fundamental understanding of process mechanics is essential to successfully transfer the process technology from a laboratory environment to a large scale production set-up.

2.3.3 Tool Wear

Although the process of ductile regime machining has been suggested as a viable alternative to current finishing technologies, an important problem is the amount of tool wear involved in the process. Yan et al. (2003a) investigated the nature and pattern of tool wear of diamond tools while cutting single crystal silicon. The authors reported that the tool wear mechanism depended on the undeformed chip thickness values. For values in the ductile-regime range, wear involved crater and flank wear whereas brittle mode chip removal led to edge micro-chipping as shown in Figure 2.14.

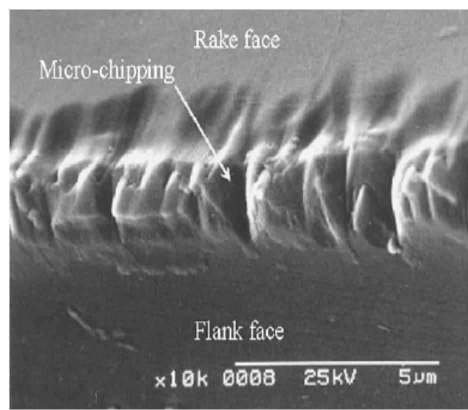

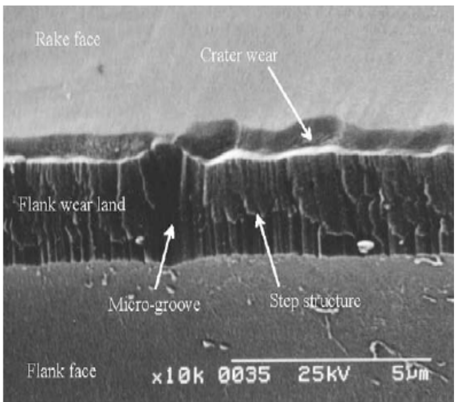

Figure 2.14 Tool wear for brittle mode removal (left) and ductile mode removal (right) (Yan et al., 2003)

Sharif Uddin et al. (2004) considered the dependence of tool wear on crystallographic orientation. They experimentally investigated ductile cutting of silicon using three different tool orientations (not workpiece material). They concluded that ductile cutting gave a smooth wear mark on the rake face and a more severe wear mark on the flank face. Additionally, the tool with {110} rake face had a longer tool life than {100} and {110} rake face tools.

Li et al. (2005) experimentally investigated tool wear for ductile cutting of silicon. It was found that the tool cutting edge radius increased as the number of tool passes increased, but the basic shape of the tool was preserved. The tool also had flank wear characterized by nano and micro grooves, which changed the tool geometry by forming sub-cutting edges of smaller radii than the main cutting edge as shown in Figure 2.15.

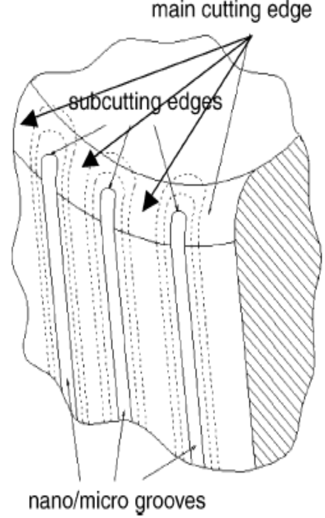

Figure 2.15 Formation of sub-cutting edges on the main cutting edge due to nano/micro grooves (Li et al., 2005)

2.3.4 Effect of Material Anisotropy

Single crystal materials are considered to be highly anisotropic in their physical and mechanical properties. Polycrystalline materials can be considered isotropic in conventional analysis, but have to treated as single crystals with random orientation in micro-cutting analysis. The effect of crystallographic orientation on the critical chip thickness is very pronounced as the plastic deformation depends on favorable slip systems which change with respect to orientation. Cohen et al. (1981) conducted experiments dealing with orthogonal machining of single crystal copper and aluminum and found that cutting force and shear angle were sensitive to crystallography and that they vary inversely with each other. Blackley and Scattergood (1990) developed a line-force stress model to predict the orientation dependence of damage symmetry. Pitting damage was found to vary depending on the cutting direction during machining of single crystal germanium. Shibata et al. (1996) demonstrated the dependence of crystallographic

directions in ductile-regime machining. Diamond turning experiments were performed along all directions on (001) and (111) planes of single crystal silicon. It was found that the crystallographic orientation affected the ductile machining for a (001) crystal significantly more than for a (111) crystal. Figure 2.16 shows that the maximum percentage of ductile mode material removal in (001) was 60% whereas for (111) crystal this ratio almost reached 95% for a chip thickness value of 1 μm.

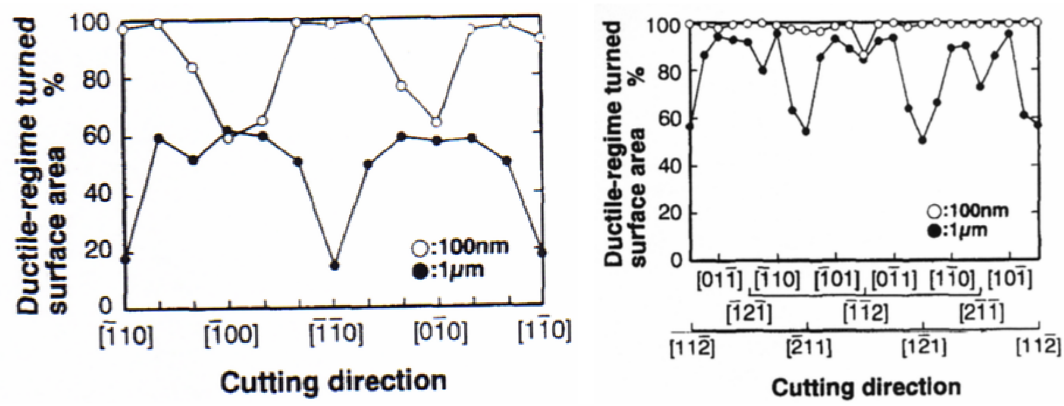

Figure 2.16 Area of ductile material removal in (001) silicon (left) and (111) silicon (right) (Shibata et al., 1996)

Hung and Fu (2000) conducted similar experiments on single crystal silicon to determine the effect of crystallographic orientation. They determined that ductile-regime machining was locally achievable along <110> directions and pitting (sub-surface damage) was observed along <100> directions. Yan et al., (2002) also experimentally studied the crystallographic dependence of critical chip thickness for single crystal silicon. The results of their study are shown in Figure 2.17.

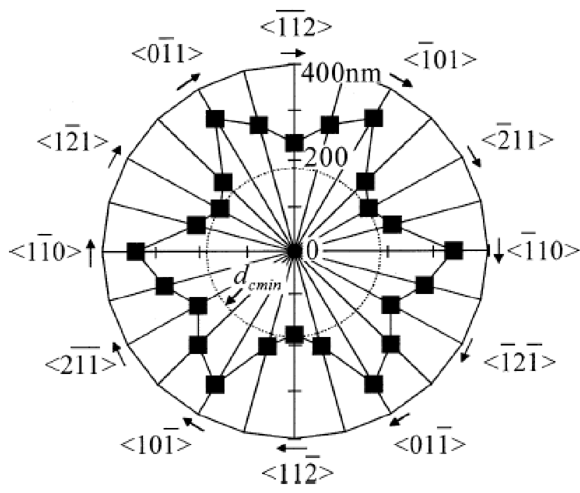

Figure 2.17 Crystallographic orientation dependence on critical chip thickness (Yan et al., 2002)

O'Connor et al. (2005) investigated ductile machining of single crystal silicon using a single point diamond flycutting setup that allows sub-micrometer, non-overlapping cuts in any direction. The results from their experiments show that the critical chip thickness varies from 40 ([100]) – 120 ([110]) nm depending on the orientation direction as shown in Figure 2.18.

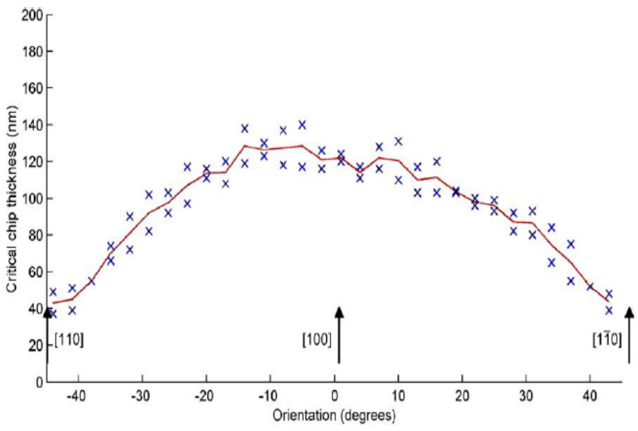

Figure 2.18 Critical chip thickness as a function of crystal orientation (O'Connor et al., 2005)

Ueda et al. (1980) studied the morphology of chip formation in single crystal β-brass and found a strong influence of crystallographic orientation on chip formation, cutting forces, shear angle and surface integrity. Lee and Zhou (1993), Lee et al. (2003) and Zhou et al. (2001) studied the effect of material anisotropy using a mesoplasticity approach during machining of polycrystalline OFHC copper. The authors add that the Taylor factor (M), a dimensionless number, is sensitive to the crystallographic orientation of the material being cut and is often used as an index of plastic anisotropy. Lee et al. (2000) also studied the effect of crystallographic orientation on surface finish for single copper crystals. The schematic representation in Figure 2.19 shows the effect of differently oriented copper crystals.

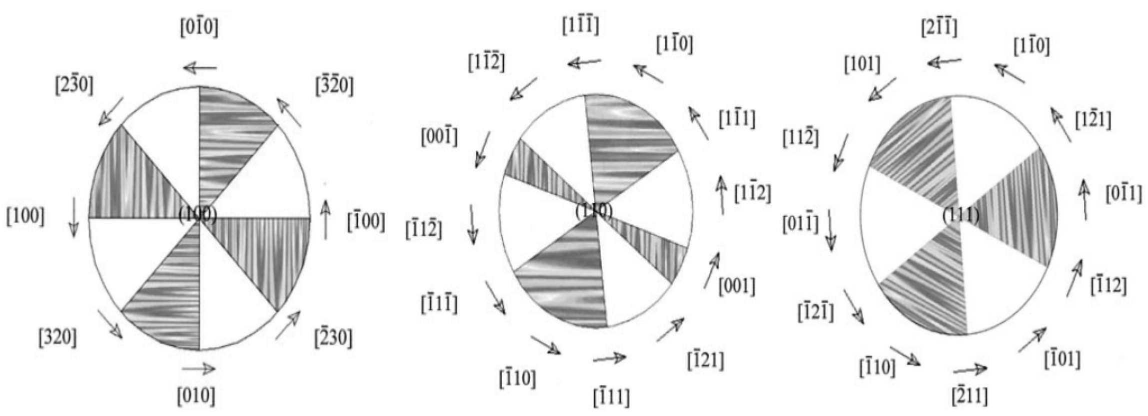

Figure 2.19 Schematic of effect of crystallographic orientation on surface roughness for (100), (110) and (111) single crystal copper (Lee et al., 2000)

2.4 Material Constitutive Model

The process of machining of materials (metals and otherwise) is characterized by plastic deformation (more pronounced in metals than in ceramics and other brittle materials) occurring at high values of strain, strain rate and temperature. The material

constitutive equation typically describes the effects of strain and in some cases, strain rate and temperature on the material flow stress. In the field of machining, two material constitutive models have been widely used. The power-law stress strain relation was initially used in machining theory by Oxley (1989) and Hastings et al. (1980) and is given as follows:

$$\sigma = K\varepsilon^n \tag{2.7}$$

where σ is uniaxial flow stress, ε is uniaxial strain, n is the strain hardening exponent and K is the strength coefficient. The constants K and n are assumed to be functions of strain rate and temperature. This model has been used for carbon steel and aluminum alloy among other materials (Arsecularatne and Zhang, 2004). The other model that has been frequently used in the area of machining is the Johnson-Cook constitutive equation (Johnson and Cook, 1983). The equation provides for the effect of large strains, strain-rates and temperatures on the yield stress of different materials as shown in (2.8). The data for the material constants are obtained from torsion tests, tensile tests and Hopkinson bar tests.

$$\sigma = [A + B \cdot \varepsilon^n][1 + C \cdot \ln \dot{\varepsilon}^*][1 - T^{*m}] \tag{2.8}$$

The constants A, B, C, m, n in (2.8) are material related constants. $\dot{\varepsilon}^*$ is the dimensionless strain rate given by the ratio of $\dot{\varepsilon}/\dot{\varepsilon}_0$ where $\dot{\varepsilon}$ is the equivalent strain rate and $\dot{\varepsilon}_0$=1.0 sec^{-1}. The homologous temperature T^* is given by the ratio $(T-T_r)/(T_m-T_r)$. The Johnson-

Cook model has been used for carbon steel, aluminum and hardened steel. Other material constitutive models that have been proposed are the Drucker-Prager (Desai and Siriwardane, 1984) model, a material model based on dislocation mechanics (Anurag and Gao, 2006), a material model constructed from orthogonal machining data (Lei et al., 1999), and Nemat-Nasser unified constitutive model (Cheng et al., 2001) which has been used for materials such as molybdenum and titanium.

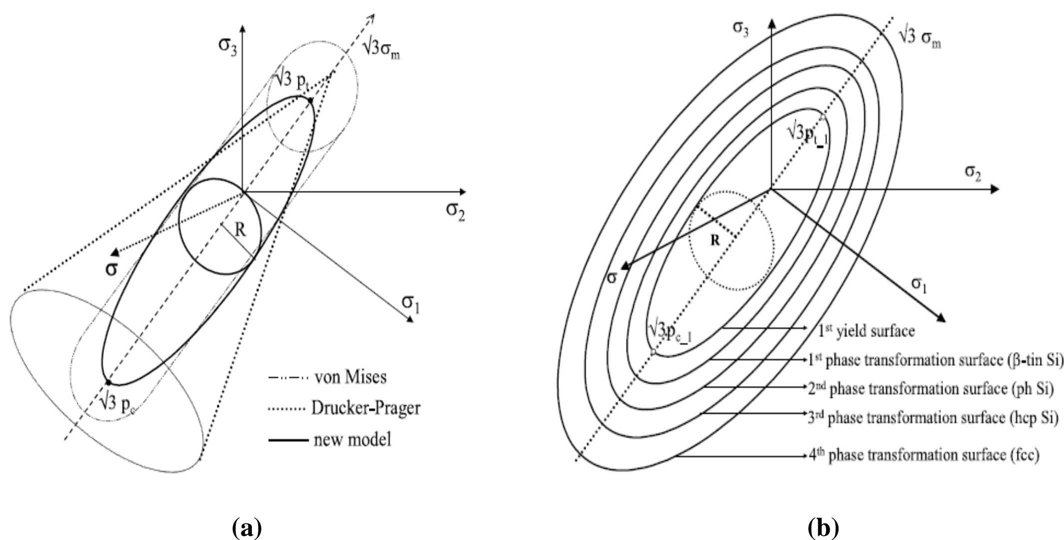

Figure 2.20 (a) Comparison of yield fucntions in principal stress space (b) Yield and phase transformation surfaces in principal stress space (loading) (Vodenitcharova and Zhang, 2004)

Vodenitcharova and Zhang (2004) presented a constitutive modeling technique for the multi-phase transformations in mono-crystalline silicon under complex loading. This model was developed based on physical mechanisms observed experimentally and the incremental theory of plasticity. The stress–strain relationship is derived using closed loading/unloading surfaces, associated flow rule and isotropic hardening rule, to reflect the pressure-sensitive behavior of the material with volumetric plastic strains. The yield function in the principal stress space for this model consists of five ellipsoids signifying

the first yield surface and the other four following phase transformations as shown in Figure 2.20. The model results are shown in Figure 2.21 depicting the elastic plastic material behavior under tension and hydrostatic compression.

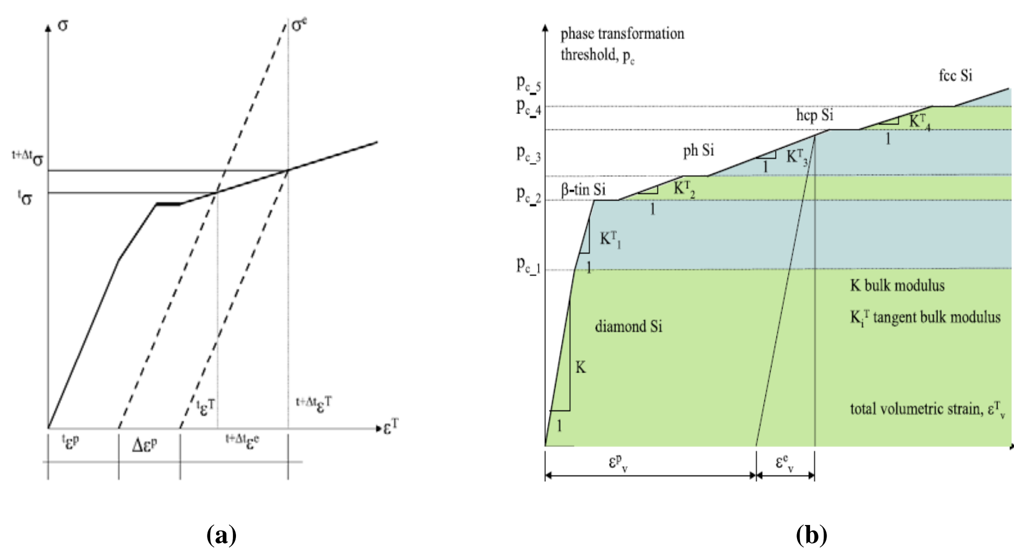

(a) **(b)**

Figure 2.21 (a) Elastic-plastic material behavior (b) Experimental working diagram of hydrostatic stress vs. volumetric total strain in pure hydrostatic compression (Vodenitcharova and Zhang, 2004)

2.5 Effect of Microstructure

The analysis of conventional machining typically ignores the effect of microstructure, as the feature sizes are much larger in comparison with the grain size of the material. But, the process of microcutting involves process parameters including depth of cut, feed etc. that are in the micrometer or sub-micrometer regime. These sizes fall in the realm of the grain size of the material and hence are affected by the size of the grain, grain boundary and crystallographic orientation. The grain size typically ranges from 100 nm to 100 μm (Liu X. et al., 2004) for materials such as aluminum and steel, 3

μm to 35 μm (Xu et al., 1998) for some ceramic materials such as alumina and silicon carbide.

The presence of different grain sizes affects the yield strength and flow stress in a polycrystalline material, as suggested by Hall (1951) and Petch (1953). According to their relation, the strength of the material is inversely proportional to the square root of the grain size. This implies that there is a strengthening of the material as the grain size shrinks. A reverse Hall-Petch effect has been reported (Li et al., 2003) for grain sizes that are smaller than a critical value; when this phenomenon takes place, the material begins to soften with a decrease in grain size. The presence of grain boundaries oriented in different positions relative to one another serves as an effective barrier to the movement of dislocations. Gao et al. (2001) proposed a Taylor based nonlocal theory of plasticity to account for the size dependence of plastic deformation in the sub-micron length scales. A similar approach is proposed by Liu K. et al. (2005) to develop a constitutive model to predict the material strengthening mechanisms. Conrad (2004) reviewed two models for grain size dependence from millimeters to nanometers on flow stress for Copper (Cu). One model is based on the concept of dislocation pile-up while the other is based on dislocation density. Li et al. (2003) also reported that the flow stress is proportional to the average misorientation and the grain size at low strains. Hughes et al. (2000) proposed a model to determine the effect of microstructure on flow stress based on dislocation theory. Hansen and Huang (1998) studied the relation between the deformation of a polycrystal and a single crystal for aluminum and the effect of microstructure on flow stress. Hansen and Juul Jensen (1992) studied the flow stress anisotropy caused by geometrically necessary boundaries which are typically dense dislocation walls and microbands. Liu Q.

et al. (1998) researched the effect of grain orientation on deformation structure in cold-rolled polycrystalline aluminum. The authors also evaluated dislocation density and stored energy for grains of different orientation using boundary parameters.

2.6 High Pressure Phase Transformation (HPPT)

The concept of ductile-regime machining has been studied from the perspective of phase transformation at the tool-chip interface (Patten et al., 2004). The existence of high pressures under the edge of the tool creates high compressive stresses which lead to phase transformation of the material locally. The material upon being removed as a chip does not have the necessary conditions to revert back to its original state. Morris et al. (1995) studied the morphology of chips using a transmission electron microscope (TEM) and found that the chips were amorphous in an elemental germanium matrix with varying amounts of microcrystalline germanium. The authors also report pitting (subsurface damage) in specific orientations on a (110) germanium wafer. Bhattacharya et al. (2005) report a similar transformation in polycrystalline silicon carbide. Their analysis shows that the chips are amorphous (not totally) in nature with some crystalline remnants of the material as shown in Figure 2.22.

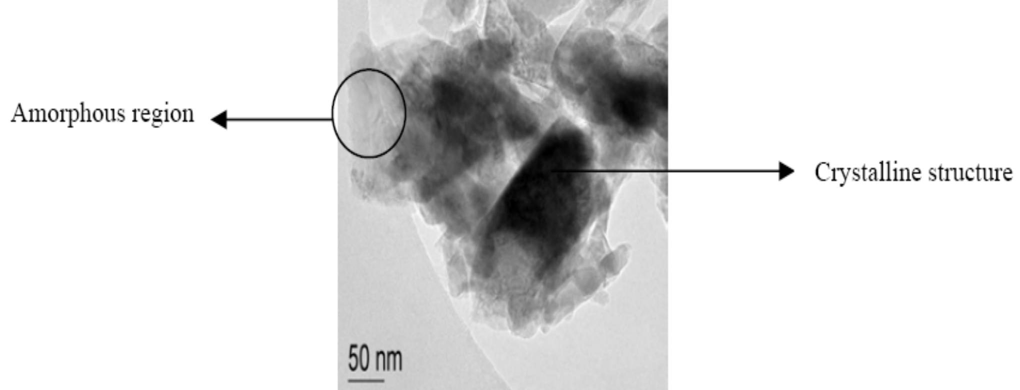

Figure 2.22 TEM picture of a polycrystalline silicon carbide chip (Bhattacharya et al., 2005)

Zhang (2004) reviewed the plastic deformation and microstructural changes in mono-crystalline silicon under various loading conditions including indentation, hydrostatic compression, cyclic loading, chemical effects, machining, indentation and tribological sliding. The author presented the various phase transformations of silicon under different conditions of loading and unloading as shown in Figure 2.23.

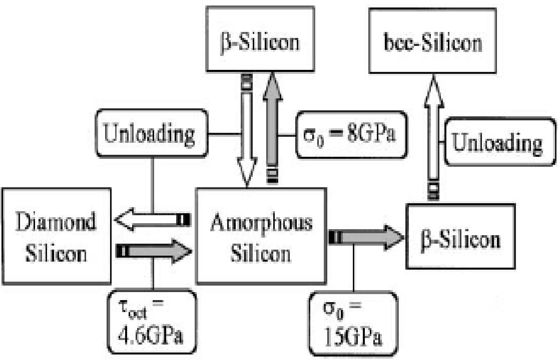

Figure 2.23 Critical states of phase transformations under indentation for silicon (Zhang, 2004)

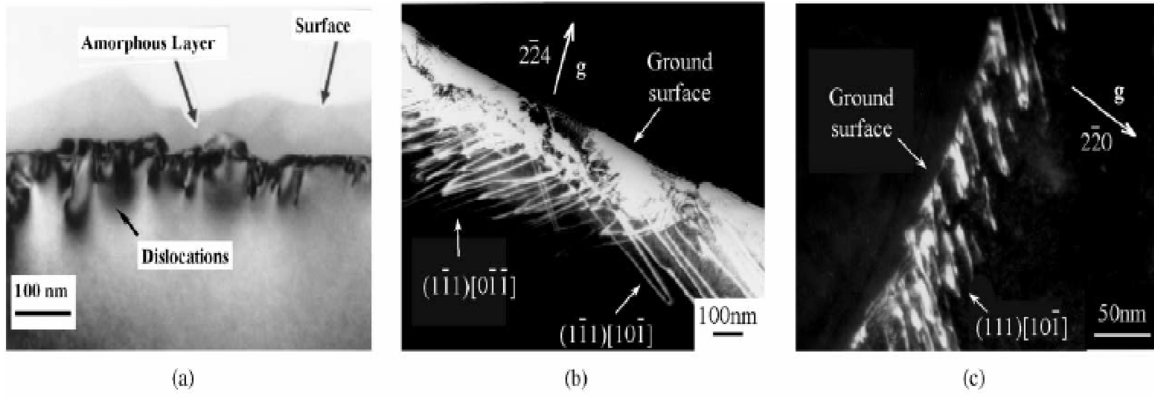

Figure 2.24 Grinding induced deformation a) both amorphous layer and dislocations b) dislocations for table speed of 1 m/min c) dislocations for table speed of 0.02 m/min (Zhang and Zarudi, 2001)

The process of machining including scratching, polishing and grinding induced deformation in mono-crystalline silicon mainly through amorphous phase transformation. But when the cutting depth increased dislocations began to emerge as shown in Figure 2.24.

The process of deformation under indentation loading for monocrystalline silicon has also been reported. Zhao and Bhushan (1998) conducted indentation tests at loads in the range of 20-80 μN. They found no evidence of dislocations when the load was 20 mN as they reasoned that the dislocations disappear during unloading. However for heavy loads of 80 μN, they found bend contours and dislocations and no evidence of phase transformation. Zarudi et al. (2004a) and Zarudi et al. (2004b) demonstrated indentation deformation at loads in the range of 30-90 mN. They found evidence of phase transformation to amorphous silicon and also two metastable phases R8 and BC8 (both crystalline). Morris and Callahan (1994) also report phase transformations under indentation loading of 100-200 mN and find the existence of β-Sn phase under loading and transformation to amorphous phase upon unloading. They further add that there is evidence of dislocation under the transformation zone.

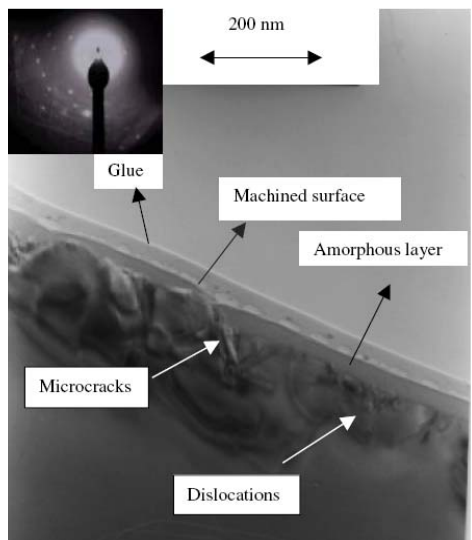

Figure 2.25 TEM image of machined surface showing amorphous layer, microcracks and dislocations (Jasinevicius et al., 2007)

Jasinevicius et al. (2007) demonstrated evidence of different phases in the machined material during the diamond turning process. Figure 2.25 shows presence of very thin amorphous layer, microcracks and also a significant amount of dislocation which is a strong indication of plastic deformation. Zarudi et al. (2005) reported that the effect of stress on the phase transformation is more pronounced than the effect of temperature suggesting that the application of high pressure is sufficient to bring about a phase transformation in monocrystalline silicon.

2.7 Summary

From the above literature review, it is evident that the process of machining is a very complex process requiring the understanding of different aspects such as force modeling, microstructural effects, process mechanics etc. The modeling of forces and effects of microstructure have been studied for ductile materials such as steels, aluminum,

copper etc. These aspects are not studied for brittle materials as conventional machining of brittle materials is not feasible. The advent of ductile-regime machining (micro-machining) has enhanced the need to study all aspects that are related to the machining process. In order to facilitate the complete understanding of the process of ductile-regime machining there is a need to develop a predictive model to determine the point of transition between ductile and brittle cutting in ductile regime machining both for single and polycrystalline materials. The model must consider the forces, friction, effects of microstructure and material properties to accurately predict the point of transition. The prediction becomes an important issue as there is a need to enhance productivity while still maintaining the desired surface texture quality. The advent of new technologies requires new materials, both ductile and brittle and such a model would be very useful to predict the usability of machining in finishing brittle materials.

This thesis will try to address the issue of developing a comprehensive model for determining the transition undeformed chip thickness in ductile-regime machining for single crystal materials. In addition it will also investigate the effect of microstructure on forces in polycrystalline materials.

CHAPTER 3

PREDICTIVE MODEL TO DETERMINE TRANSITION UNDEFORMED CHIP THICKNESS FOR SINGLE CRYSTAL SILICON

Silicon (Si) is the material that drives the semiconductor industry, and the semiconductor is the building block for the information technology (IT) industry. The semiconductor industry is worth $ 213 billion a year and is the backbone for other fields such as telecommunications, internet etc. The industry represents 10% of the world gross domestic product (GDP) and according to industry sources the semiconductor industry could grow to $ 260 billion by 2009 (van Houten, 2005).

The process of growing a silicon wafer is time consuming and depends on a lot of factors such as size and quality of the wafers. The silicon wafers are usually grown by the Czochralski (CZ) method. The CZ method of growing silicon requires pure polycrystalline silicon chunks along with small quantities of dopants such as boron, phosphorous, antimony etc. The materials are heated to a temperature above the melting point of silicon (1415 ^{o}C). A single crystal of silicon having the desired orientation, called the seed crystal, is placed on top of the melt and slowly lifted out allowing the growth of silicon. The cooling process orients the crystal structure to that of the seed crystal. The silicon ingots thus produced are then sliced into wafers using a diamond edge saw to a nominal thickness. The sliced wafers are then taken through a lapping process to remove any marks and defects. Then the wafers are etched and cleaned to remove any microscale defects. The final and the most crucial step is the process of polishing the

wafers. The polishing process is done in stages using polishing compounds or slurries of grain sizes ranging from coarse to fine.

The process of grinding, polishing, and lapping has almost always been used as the finishing process in the manufacture of single crystal silicon wafers and also for other semiconductor and optical materials. The process of diamond turning to which silicon is amenable has been suggested as an alternative to the traditional finishing processes. Diamond turning of silicon may be able to minimize the amount of finishing required and hence reduce the cost and increase the effectiveness of the silicon manufacturing process.

The process of diamond turning is used for conventional and finish machining, as it produces high quality surfaces and features. However, in machining brittle materials conventional process parameters may not be employed, as the materials crack on the surface and subsurface due to marks left by the motion of the tool. In recent years it has been discovered that the surface and subsurface damage caused in the finished material can be reduced as the undeformed chip thickness (a key process parameter) is reduced. It has also been observed that there exists a critical value for which there is no observed subsurface damage. This critical value is known as the transition undeformed chip thickness, and the process of machining brittle materials in such a fashion is called ductile-regime machining. The process is shown as a schematic in Figure 3.1. When the undeformed chip thickness is large the brittle material cracks and forms discontinuous chips, but when the undeformed chip thickness is below the threshold value continuous chips are formed leaving a crack-free surface on the material. The goal of this chapter is to develop a predictive model to determine this transition undeformed chip thickness.

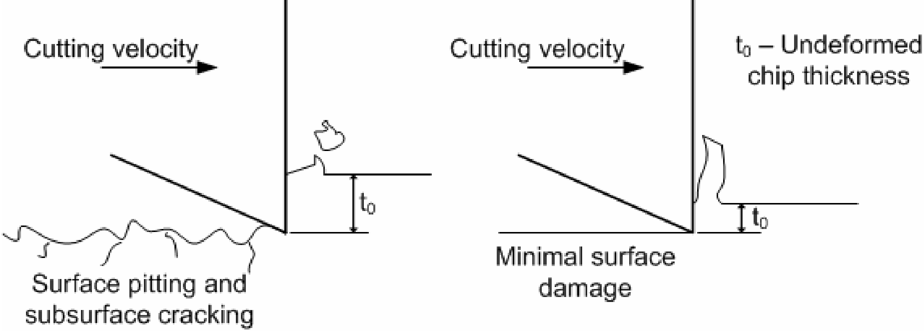

Figure 3.1 Brittle material removal (left) and ductile material removal (right) (adopted from O'Connor, 2002)

The predictive model described in this chapter is based on the following material removal mechanism. When the resolved shear stress (τ_{slip}) exceeds the critical flow stress of the material (τ_c) and if the stress intensity factor (K_I) does not exceed the fracture toughness (K_{Ic}) then the material removal is through localized plastic deformation. But when K_I exceeds K_{Ic} then the material is removed through the propagation of cracks. Therefore, the transition between ductile and brittle modes of material removal occurs when the stress intensity factor equals the fracture toughness of the material. In addition, the flow stress must be greater then the critical shear stress of the material in order to facilitate plastic deformation and material removal (Liu K. et al., 2004). The model described below takes into account the tool geometry, workpiece material properties, and process conditions as input and predicts cutting and thrust forces and the transition undeformed chip thickness.

3.1 Properties of Silicon

The material properties of silicon are very important for understanding the nature of the material and its response to machining. It is well known that silicon is a brittle

material which fails by propagation of cracks and ultimately by fracture. But the material response changes as a shift is made into the microscopic regime of machining. This change in behavior has to do with the property of silicon. The following table (Table 3-1) summarizes some of the key properties of silicon.

Table 3-1 Properties of Silicon

Property	Value/Representation	Reference
Chemical composition	Si	
Atomic number	14	
Atomic weight	28.09	Kovacs, 1998
Boiling point	2878 ^{o}C	Yaws et al., 1981
Burgers vector (b)	0.383 nm	Frost and Ashby, 1982
Crystal structure	Diamond (cubic)	Yoshino et al., 2005
Density (ρ)	2.328 g/cm^3	Kovacs, 1998
Lattice constant (a)	0.5431 nm	Kovacs, 1998
Melting point	1415 ^{o}C	Kovacs, 1998
Specific heat (c)	0.7 $J/g.K$	Kovacs, 1998
Coefficient of thermal expansion (CTE)	2.6 x 10^{-6} K^{-1}	Kovacs, 1998
Thermal conductivity (k)	1.5 $W/cm.K$	Kovacs, 1998
Thermal diffusivity (α)	0.9 cm^2/s	Kovacs, 1998
Compliance constants	s_{11} – 7.68 x 10^{-12} Pa^{-1} s_{12} – -2.14 x 10^{-12} Pa^{-1} s_{44} – 12.56 x 10^{-12} Pa^{-1}	O'Connor, 2002
Stiffness constants	c_{11} – 165.7 GPa c_{12} – 63.9 GPa c_{44} – 79.56 GPa	O'Connor, 2002
Young's modulus (E)	129.9 GPa 190 GPa	Yoshino et al., 2005 Kovacs, 1998
Hardness (H – Vickers)	850 Kg/mm^2	Yoshino et al., 2005
Fracture toughness (K_{Ic})	(100) – 0.95 $MPa.m^{1/2}$ (110) – 0.90 $MPa.m^{1/2}$ (111) – 0.82 $MPa.m^{1/2}$ 0.804 $MPa.m^{1/2}$	O'Connor, 2002 Yoshino et al., 2005
Poisson ratio (υ)	0.273	Yoshino et al., 2005
Yield strength (σ_0)	2.956 GPa 7.0 GPa	Yoshino et al., 2005 Kovacs, 1998
Shear modulus (G)	63.7 GPa	Frost and Ashby, 1982

3.2 Force Model

The force model discussed here is for the case of orthogonal machining where the cutting edge is perpendicular to the direction of the cutting velocity. The reason for considering the orthogonal cutting process is that it serves as a reasonably good approximation to study the mechanics of the cutting process. The force model (adopted from Liu K., 2002) discussed here predicts cutting and thrust forces by considering an infinitesimally small area around the rounded edge of the tool and evaluating the incremental forces in that area. The incremental forces are integrated around the edge of the tool where the tool contacts the workpiece.

Figure 3.2 shows the schematic of the cutting process and the mechanics around the cutting edge *BC*. The cutting edge is assumed as a circular arc with *O* as the center and edge radius *r*. The direction of motion of the tool as shown in the schematic is the cutting direction and it is assumed that the tool moves with a velocity *V*, termed the cutting velocity. The cutting tool has a nominal rake angle of γ which is typically specified by the tool manufacturer. For a nominal rake angle of $\gamma = 0$ degrees the line *OC* becomes horizontal. As stated earlier, the forces are computed by considering an infinitesimally small area *dk* around the point *K*. The instantaneous value of the undeformed chip thickness is designated as t_{0k} and the cut chip thickness is t_{1k}. From the schematic it is obvious that the instantaneous rake angle is not the same as the nominal rake angle. The instantaneous rake angle (γ_k) is highly negative and this facilitates the compressive stresses beneath the edge of the tool. The expression for the instantaneous rake angle is given by (3.1) and is dependent on the undeformed chip thickness (t_0) and the tool edge radius.

$$\gamma_k = \theta = \sin^{-1}\left(\frac{t_0}{r} - 1\right) \qquad t_0 \le r(1+\sin\gamma)$$
$$\gamma_k = \gamma \qquad t_0 > r(1+\sin\gamma) \tag{3.1}$$

The instantaneous value of shear angle is designated as φ_k and its value also changes depending on the instantaneous value of the undeformed chip thickness. The shear angle is related to instantaneous rake angle through the relation (Merchant, 1945) given in (3.2).

$$\tan\varphi_k = \frac{r_c \cos\gamma_k}{1 - r_c \sin\gamma_k} \tag{3.2}$$

The ratio of undeformed chip thickness to the cut chip thickness (t_1) is termed as the chip ratio or cutting ratio (r_c). The chip ratio is typically calculated based on measurements made on the chip after machining. The typical chip ratio for micromachining is in the range of 0.29-0.36 (Shaw, 1987).

From Figure 3.2, the cutting and thrust force per unit width corresponding to the infinitesimally small cutting edge *dk* is given by the following expression.

$$dF_c = \frac{k_s \cdot \cos(\beta_k - \gamma_k) \cdot r\cos(\gamma_k)}{\sin(\varphi_k) \cdot \cos(\varphi_k - \beta_k - \gamma_k)} d\gamma_k$$
$$dF_t = \frac{k_s \cdot \sin(\beta_k - \gamma_k) \cdot r\cos(\gamma_k)}{\sin(\varphi_k) \cdot \cos(\varphi_k - \beta_k - \gamma_k)} d\gamma_k \tag{3.3}$$

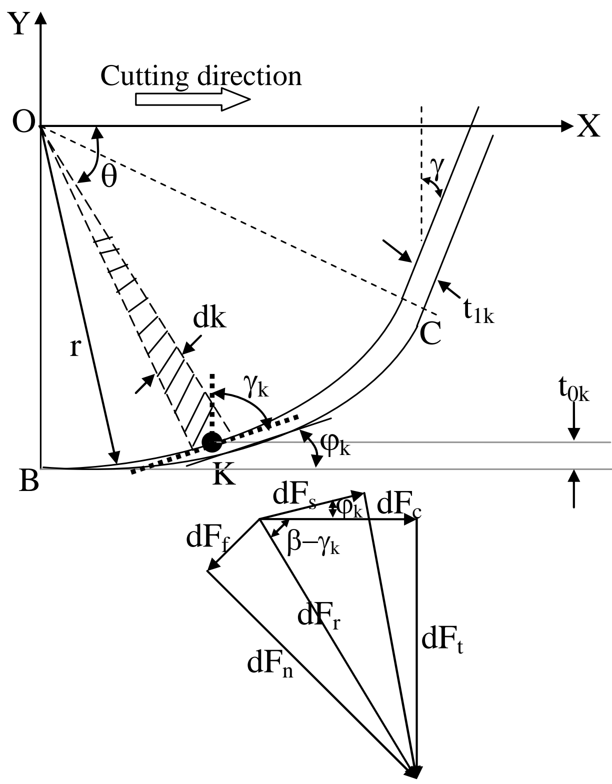

Figure 3.2 Mechanics around the rounded tool edge (Venkatachalam and Liang, 2007)

In (3.3) dF_c and dF_t represent the infinitesimally small cutting and thrust forces respectively. The angle β_k is the instantaneous friciton angle which is computed from the coefficient of friction. The coefficient of friciton has been shown to be variable in the micro and nano scale by Zhang and Tanaka (1997). The shear flow stress (k_s) given in the expression is a material property.

In the micromachining regime the forces represent a combination of two actions viz., chip formation and ploughing. During the process of machining at a depth of cut less than the tool edge radius, some of the material (Figure 2.4) flows towards the tool rake face as a chip (above the point of separation), while the remaining material flows beneath the rounded tool edge (below the point of separation). This process leads to the chip

formation of the material above the point of separation and ploughing of the material below the point of separation. The point of separation is difficult to predict and one such research attempt was undertaken by Basuray et al. (1977). It was reported that the transition point for cutting is constant and equal to 37.6°. The expression for cutting and thrust forces includes both ploughing and chip formation forces. However, the model does not attempt to separate the ploughing and chip formation forces.

The cutting and thrust forces for chip formation and ploughing are obtained by integrating the infinitesimal forces in (3.3). The expressions for cutting and thrust forces per unit width are given in (3.4) and (3.5) respectively.

$$\begin{cases} F_c = \displaystyle\int_{-\pi/2}^{\gamma} \frac{k_s \cdot \cos(\beta_k - \gamma_k) \cdot r\cos(\gamma_k)}{\sin(\varphi_k) \cdot \cos(\varphi_k + \beta_k - \gamma_k)} d\gamma_k + \frac{k_s \cdot \cos(\beta - \gamma) \cdot \left(t_0 - r(1 + \sin\gamma)\right)}{\sin(\varphi) \cdot \cos(\varphi + \beta - \gamma)}, & t_0 > r(1 + \sin\gamma) \\ F_c = \displaystyle\int_{-\pi/2}^{\sin^{-1}\left(\frac{t_0}{r} - 1\right)} \frac{k_s \cdot \cos(\beta_k - \gamma_k) \cdot r\cos(\gamma_k)}{\sin(\varphi_k) \cdot \cos(\varphi_k + \beta_k - \gamma_k)} d\gamma_k & , t_0 \le r(1 + \sin\gamma) \end{cases} \tag{3.4}$$

$$\begin{cases} F_t = \displaystyle\int_{-\pi/2}^{\gamma} \frac{k_s \cdot \sin(\beta_k - \gamma_k) \cdot r\cos(\gamma_k)}{\sin(\varphi_k) \cdot \cos(\varphi_k + \beta_k - \gamma_k)} d\gamma_k + \frac{k_s \cdot \sin(\beta - \gamma) \cdot \left(t_0 - r(1 + \sin\gamma)\right)}{\sin(\varphi) \cdot \cos(\varphi + \beta - \gamma)}, & t_0 > r(1 + \sin\gamma) \\ F_t = \displaystyle\int_{-\pi/2}^{\sin^{-1}\left(\frac{t_0}{r} - 1\right)} \frac{k_s \cdot \sin(\beta_k - \gamma_k) \cdot r\cos(\gamma_k)}{\sin(\varphi_k) \cdot \cos(\varphi_k + \beta_k - \gamma_k)} d\gamma_k & , t_0 \le r(1 + \sin\gamma) \end{cases} \tag{3.5}$$

k_s is shear flow stress, β is friction angle, φ is shear angle, and r is tool edge radius. The term k_s in the equation represents the shear flow stress and is modeled based on material constitutive equation to be discussed later.

In order to overcome the difficulty of expressing the forces using the nominal tool rake angle, Liu K (2002) proposed an equivalent tool rake angle (Figure 3.3) and shear angle for the region around the tool edge radius. The equivalent tool rake angle (γ_e) is given by (3.6) and the equivalent shear angle is then derived from the equivalent rake angle as given in (3.7).

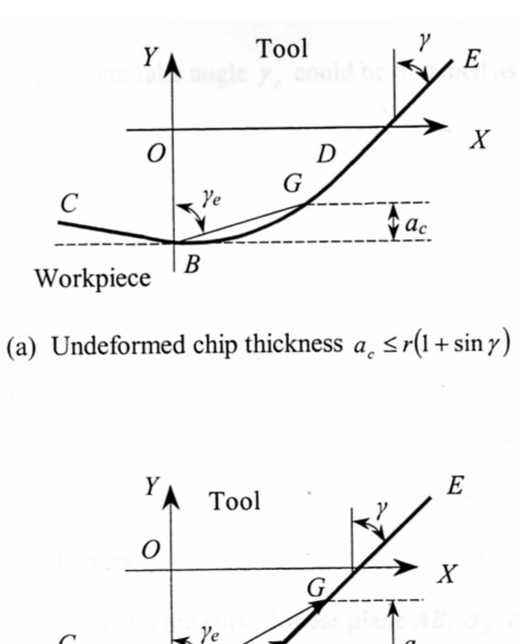

Figure 3.3 Equivalent rake angle for different undeformed chip thickness (Liu K., 2002)

$$\begin{cases} \gamma_e = -\dfrac{\pi}{2} + \tan^{-1}\left(\dfrac{t_0}{\sqrt{(2r-t_0)t_0}}\right) & , t_0 > r(1+\sin\gamma) \\ \gamma_e = -\dfrac{\pi}{2} + \tan^{-1}\left(\dfrac{t_0}{[r(1+\sin\gamma)-t_0]\tan\gamma + r\cos\gamma}\right) & , t_0 > r(1+\sin\gamma) \end{cases} \tag{3.6}$$

$$\tan \varphi_e = \frac{r_c \cos \gamma_e}{1 - r_c \sin \gamma_e} \tag{3.7}$$

The average normal stress per unit width on the shear plane can be obtained from the cutting and thrust forces using (3.8).

$$\sigma_s = \frac{(F_c \sin \varphi_e + F_t \cos \varphi_e) \sin \varphi_e}{t_0} \tag{3.8}$$

Similarly, the shear stress per unit width on the shear plane can also be obtained from the cutting and thrust forces as given by (3.9).

$$\tau_s = \frac{(F_c \cos \varphi_e - F_t \sin \varphi_e) \sin \varphi_e}{t_0} \tag{3.9}$$

3.3 Material Constitutive Model

The material constitutive model adopted in this work is based on Johnson-Cook's model (Johnson and Cook, 1983) which is used to describe the effect of strain, strain rate and temperature on the material flow stress, especially for metals. The applicability of this model for a brittle material such as single crystal silicon is based on the assumption that there is appreciable material flow during ductile regime machining. Moreover, it is also assumed that the strain, strain rate and temperature affect the chip formation process in ductile regime machining. A survey of constitutive equations used in machining

(Arsecularatne and Zhang, 2004) revealed that there is insufficient data in order to develop a reliable constitutive model for predictive theories in machining.

The Johnson-Cook's model relates the material flow stress to the changes in strain, strain rate and temperature and is given by

$$\sigma = [A + B \cdot \varepsilon^n][1 + C \cdot \ln \dot{\varepsilon}^*][1 - T^{*m}] \tag{3.10}$$

where σ is the material flow stress. A, B, C, m, and n are material constants, ε is the equivalent strain, $\dot{\varepsilon}^*$ is the dimensionless strain rate given by the ratio of $\dot{\varepsilon}/\dot{\varepsilon}_0$ where $\dot{\varepsilon}$ is the equivalent strain rate and $\dot{\varepsilon}_0$=1.0 sec^{-1}. The homologous temperature T^* is given by

$$T^* = \frac{T - T_r}{T_m - T_r} \tag{3.11}$$

The shear flow stress k_s in (3.4) and (3.5) can be computed as

$$k_s = \frac{1}{\sqrt{3}} \left([A + B \cdot \varepsilon^n] \left[1 + C \cdot \ln \frac{\dot{\varepsilon}}{\dot{\varepsilon}_0} \right] \left[1 - \left(\frac{T - T_r}{T_m - T_r} \right)^m \right] \right) \tag{3.12}$$

The constants *A, B, C, m, n* in (3.12) are defined for some materials in Johnson and Cook (1983). Unfortunately, the material constants for silicon (material used for machining tests) could not be found in any prior work. In order to use the Johnson-Cook model for determining the shear flow stress factor, an optimization procedure is used

which is discussed herein. The process of optimization (Ramesh, 2002) involved different techniques being utilized in order to arrive at a solution. The optimization process can be summarized by (3.13) which is basically a non-linear least squares method to minimize the difference between experimental and predicted force values.

$$Min:\sqrt{\left[\left(A+B\varepsilon^{n}\right)\left(1+C\ln\dot{\varepsilon}\right)\left(1-(T^{*})^{m}\right)*S_{1}-C_{1}\right]^{2}+\left[\left(A+B\varepsilon^{n}\right)\left(1+C\ln\dot{\varepsilon}\right)\left(1-(T^{*})^{m}\right)*S_{2}-C_{2}\right]^{2}} \quad (3.13)$$

where S_1 and S_2 are constants associated with simulated cutting and thrust force data based on tool properties and process conditions respectively. C_1 and C_2 are the experimentally measured values of cutting and thrust forces respectively. The optimization process was carried out utilizing the simplex (Nelder-Mead) method using Matlab®. This approach required an initial guess for the constants *A, B, C, m, n*. It must be pointed out that the results did not converge to a global optimum, but rather to a local optimum. Therefore the results were a direct function of either the initial values or the constraints. The values for constants using the Nelder-Mead search algorithm are shown in Table 3-2.

Table 3-2 Johnson-Cook constants for Si

A (MPa)	896.394
B (MPa)	529.273
C	0.4242
n	0.3758
m	1.0

3.4 Strain and Strain Rate

The process of plastic deformation imparts very high strains in the deformation zone and these strains are larger than most of the deformation processes. The strain-rate

is also very high in machining, as the strains are imparted in a narrow zone which is rapidly traversed. In the area of metal cutting, the strain and strain rate are typically computed using the platelet model of chip formation (Shaw, 1987) as shown in Figure 3.4.

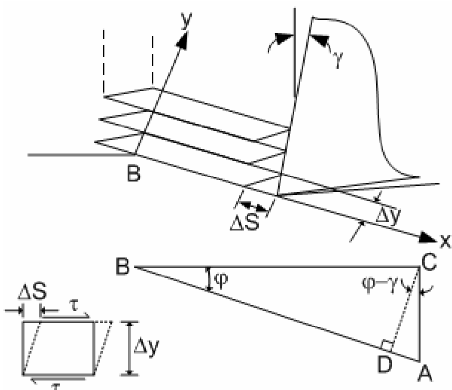

Figure 3.4 Determination of shear strain in cutting (Shaw, 1987)

The shear strain (γ_s) and shear strain-rate ($\dot{\gamma}$) are computed as given by (3.14) and (3.15) respectively where V is the cutting velocity and Δy is the thickness of the platelets.

$$\gamma_s = \frac{\cos\gamma}{\cos(\varphi-\gamma)\sin\varphi} \tag{3.14}$$

$$\dot{\gamma} = \frac{\cos\gamma}{\cos(\varphi-\gamma)}\frac{V}{\Delta y} \tag{3.15}$$

Another method to compute strain and strain-rate for metal cutting processes is given by Oxley (1989). The strain along the shear plane (tool-chip interface) is given by

$$\gamma_s = \frac{1}{2}\frac{\cos\gamma}{\sin\varphi\cos(\varphi-\gamma)} \tag{3.16}$$

where γ is the nominal rake angle of the tool and φ is the nominal shear angle. The strain rate along the tool-chip interface is given by

$$\dot{\gamma} = C\frac{V_s}{l} \tag{3.17}$$

where C is a constant, l is the length of the shear plane ($l = t_0/\sin\varphi$) and V_s is the shear velocity, which is related to the cutting velocity (V) by the following equation.

$$V_s = V\frac{\cos\gamma}{\cos(\varphi-\gamma)} \tag{3.18}$$

Although the above methods have been widely accepted and utilized, there is a need for computing the strain and strain-rate for micro machining where the tool can no longer be assumed to be perfectly sharp. Manjunathaiah and Endres (2000) proposed a model to compute the strain and strain rate for micro machining with an edge-radius tool. The strain and strain rate components used in this work are adopted from Manjunathaiah and Endres (2000). The scenario of micro machining used to derive expressions for strain and strain rate is depicted in Figure 3.5.

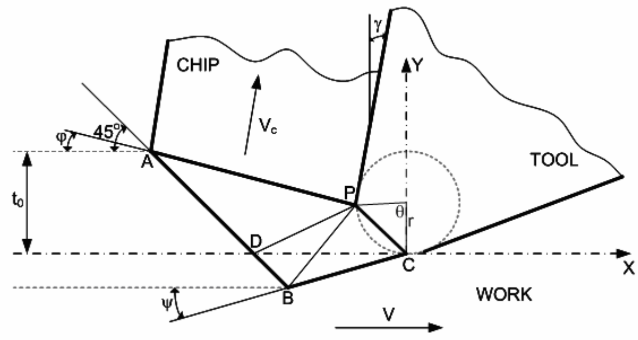

Figure 3.5 Geometry of cutting process (reproduced from Manjunathaiah and Endres, 2000)

The shear strain of the chip entering boundary *AD* is given by

$$\gamma_{chip} = \frac{\sqrt{2}\sin\theta_{PD}}{\sin(\pi/4+\theta_{PD})} + \frac{\cos(\gamma+\theta_{PD})}{\cos(\gamma-\varphi)\sin(\varphi+\theta_{PD})} \tag{3.19}$$

where θ_{PD} is the inclination of line *PD* (Figure 3.5) with the horizontal. As the angle θ_{PD} tends to zero, the expression reduces to Merchant's shear model. The strain on the machined surface can be written as

$$\gamma_{work} = \frac{\sqrt{2}\sin\theta_{PD}}{\sin\left(\frac{\pi}{4}+\theta_{PD}\right)} + \frac{\sin\left(\theta_{PD}+\frac{\theta}{2}\right)}{\sin\left(\theta_{PB}+\frac{\theta}{2}\right)\sin(\theta_{PB}+\theta_{PD})} + \frac{\sin\frac{\theta}{2}}{\sin\psi\sin\left(\psi+\frac{\theta}{2}\right)} \tag{3.20}$$

where ψ is the inclination of boundary *BC*. The effective strain can be written as weighted functions of the strains in the chip and work as

$$\gamma_{s(eff)} = \frac{\upsilon_{chip}\gamma_{chip} + \upsilon_{work}\gamma_{work}}{\upsilon_{chip} + \upsilon_{work}} \tag{3.21}$$

The shear strain rate is computed taking into account the deformation in the zone ABCP. The shear strain rate for the chip and workpiece are given by the following expressions.

$$\dot{\gamma}_{chip} = 2V \frac{\gamma_{chip}}{\sqrt{2}\sin(\pi/4+\theta_{PD})\overline{PD}}$$
$$\dot{\gamma}_{work} = 2V \frac{\gamma_{work}}{\sqrt{2}\sin(\pi/4+\theta_{PD})\overline{PD}+\frac{\sin(\psi+\theta/2)}{\sin\psi}\overline{PC}} \tag{3.22}$$

where $\overline{PC}$ and $\overline{PD}$ are the lengths of the points connecting PC and PD respectively. The effective shear strain rate is given as a weighted function of the strain rates of chip and work as given by

$$\dot{\gamma}_{eff} = \frac{\upsilon_{chip}\dot{\gamma}_{chip} + \upsilon_{work}\dot{\gamma}_{work}}{\upsilon_{chip}+\upsilon_{work}} \tag{3.23}$$

The strain and strain rate in (3.12) can be computed as $\varepsilon = \gamma_{s(eff)} / \sqrt{3}$ and $\dot{\varepsilon} = \dot{\gamma}_{eff} / \sqrt{3}$.

3.5 Fracture Toughness

Brittle materials are known to fail by crack propagation and ultimately fracture. Griffith proposed quantitative relationship in determining the fracture of cracked solids. Griffith observed that when a crack is introduced to a stressed plate, a balance is required between the decrease in potential energy and the increase in surface energy resulting from the presence of the crack (Hertzberg, 1976). The presence of cracks, defects, pores etc. present in brittle materials during their fabrication makes the analysis of stresses on

cracked solids very important. Moreover, the cracks are sources of stress concentration and hence would assume critical importance since the cracks propagate under the influence of stress and ultimately cause the material to fail by fracture.

The stress fields surrounding a crack tip can be divided into three major modes of loading that involve different crack surface displacements as shown in Figure 3.6. It should be pointed out that Mode I loading is encountered in many engineering applications. The presence of mixed Mode I-II (Figure 3.7) loading is observed when there is an inclined crack and the loading is axial. An example of Mode III loading is an instance of a notched round bar in torsion.

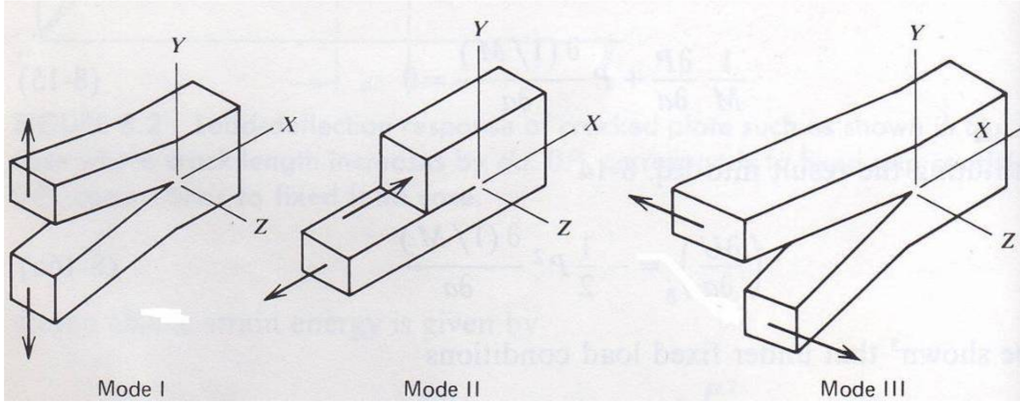

Figure 3.6 Basic modes of loading involving different crack surface displacements (Hertzberg, 1976)

Mode I – Opening or tensile mode, where the crack surfaces move directly apart.

Mode II – Sliding or in-plane shear mode, where the crack surfaces slide over one another in a direction perpendicular to the leading edge of the crack.

Mode III – Tearing or out-of-plane shear mode, where the crack surfaces move relative to one another and parallel to the leading edge of the crack.

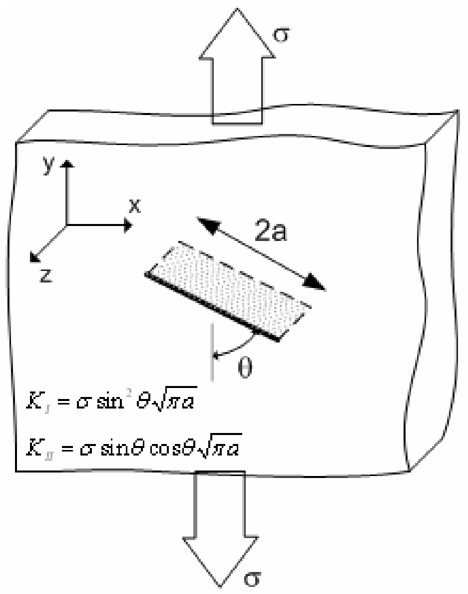

Figure 3.7 Crack inclined θ degrees from z axis. Mode I dominates when θ > 60° (Hertzberg, 1976)

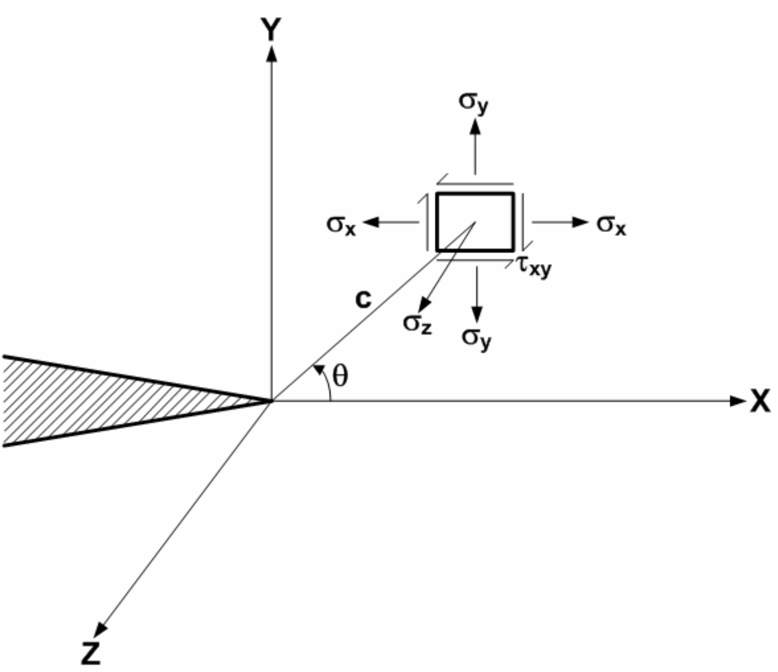

Figure 3.8 Distribution of stresses in the vicinity of crack tip (Hertzberg, 1976)

The stresses at the crack (Figure 3.8) tip can be defined based on the stress intensity factor (K), which characterizes the magnitude (intensity) of the stresses in the vicinity of an ideally sharp crack tip, using the following equations (Dowling, 1999).

$$
\begin{aligned}
\sigma_x &= \frac{K}{\sqrt{2\pi c}}\cos\frac{\theta}{2}\left[1-\sin\frac{\theta}{2}\sin\frac{3\theta}{2}\right] \\
\sigma_y &= \frac{K}{\sqrt{2\pi c}}\cos\frac{\theta}{2}\left[1+\sin\frac{\theta}{2}\sin\frac{3\theta}{2}\right] \\
\tau_{xy} &= \frac{K}{\sqrt{2\pi c}}\cos\frac{\theta}{2}\sin\frac{\theta}{2}\cos\frac{3\theta}{2} \\
\sigma_z &= 0 \qquad \text{(plane stress)} \\
\sigma_z &= \nu(\sigma_x+\sigma_y) \qquad (\text{plane strain}; \varepsilon_z = 0)
\end{aligned}
\tag{3.24}
$$

In (3.24), σ_x, σ_y and σ_z are normal stresses in the *X*, *Y* and *Z* directions respectively. For the special case of thin plates the normal stress in the *Z* direction does not increase appreciably and hence can be assumed to be zero. On the other hand, for thick sections the normal stress in *Z* direction creates a situation of triaxial stresses thereby restricting strain in the *Z* direction.

The stress intensity factor (K_I) and its relation to the fracture toughness (K_{Ic}) is very important when considering the fracture of brittle materials. Irwin's model (Irwin, 1957) for stress intensity factor considered both crack inclination and crack distribution density in the material because it is more than likely that the material that is being machined can have more than one defect. Consider a plate with cracks of length *2a* subjected to a stress σ at the boundary as shown in Figure 3.9.

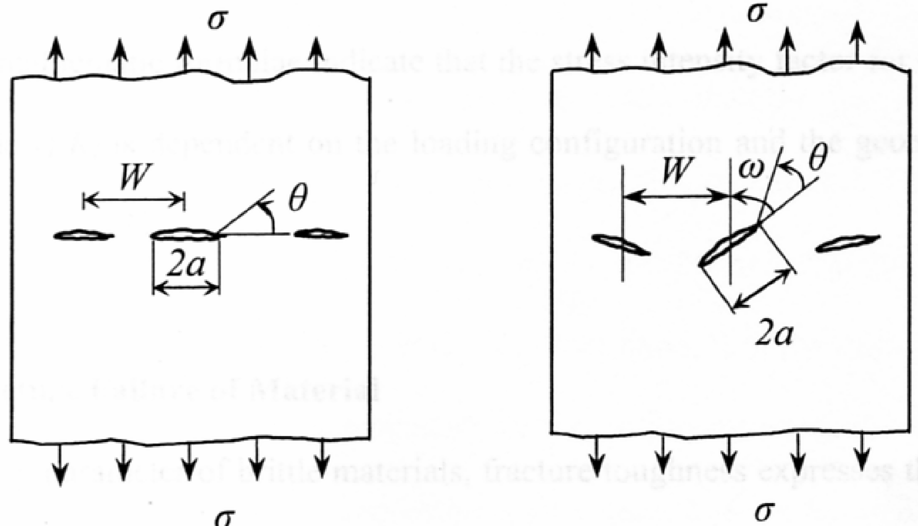

Figure 3.9 Plat with cracks (non-inclined (left) and inclined (right)) subject to uniform stress (Liu K., 2002)

The stress intensity factor for the scenario in Figure 3.9 is given by

$$K_I = F\sigma\sqrt{\pi a}\, f\left(\frac{a}{W}\right) \tag{3.25}$$

where F is the geometric factor and $f(a/W)$ is a function of the crack size and distribution which can be expressed as

$$f\left(\frac{a}{W}\right) = \left(\frac{W}{\pi a}\tan\frac{\pi a}{W}\right)^{1/2} \tag{3.26}$$

where a is the length of the crack, and W is width of the finite plate with an internal crack. The expression for the stress intensity factor in the opening mode is then given by (Liu K., 2002)

$$K_I = F\sigma\sqrt{\pi a}\left[1 + \frac{\pi^2 a^2}{3W^2} + \frac{2\pi^4 a^4}{15W^4} + \ldots\right]^{1/2} \sin^2\omega \tag{3.27}$$

where ω is the crack angle. An expression similar to (3.27), can be used to calculate the mode II stress intensity factor (Hertzberg, 1976) as given below.

$$K_{II} = F\sigma\sqrt{\pi a}\left[1+\frac{\pi^2 a^2}{3W^2}+\frac{2\pi^4 a^4}{15W^4}+...\right]^{1/2}\sin\omega\cos\omega \tag{3.28}$$

A combined stress intensity factor (Strenkowski and Hiatt, 1990) can be obtained by using (3.29). It should however be pointed out that in many cutting situations, mode I dominates and hence mode II can be neglected. Moreover, the fracture toughness values for mode II are not readily available in the literature and hence were not considered.

$$K = \sqrt{K_I^2 + 1.78K_{II}^2} \tag{3.29}$$

3.6 Comprehensive Model

The schematic shown in Figure 3.10 describes the procedure to compute the transition undeformed chip thickness. The stress intensity factor given in (3.27) is dictated by the nature of stresses in the tool-chip interface. The stress intensity factor in turn determines if the mode of material removal is plastic deformation or crack propagation along certain slip systems. When the stress intensity factor is less than the fracture toughness of the material and the resolved shear stress is greater than a critical value (also a material property), then the situation is conducive for plastic deformation to take place in the localized region of the tool-chip interface. On the contrary, if the stress intensity factor exceeds the fracture toughness of the material, then the material removal

occurs by propagation of cracks along certain favorable slip systems which ultimately leads to brittle fracture, resulting in an undesirable surface finish. Therefore, the transition between ductile and brittle modes of material removal occurs when the stress intensity factor equals the fracture toughness of the material.

Ductile-to-brittle transition in micro-machining exists due to competing factors between the minimum energy associated with volume effects (plastic deformation) and surface effects (brittle fracture). During the process of micro-machining there exists a high compressive stress beneath the tool edge which reduces the stress intensity such that the propagation of cracks is inhibited and material flow through plastic deformation becomes a more probable mode of material removal. Brittle failure in micro-machining can occur (i) during chip formation, (ii) due to the trailing tensile stress field, and (iii) due to lateral crack formation after tool pass (Patten et al., 2004). Fracture during chip formation and fracture behind the tool can occur due to large depth of cut or insufficient rake angle.

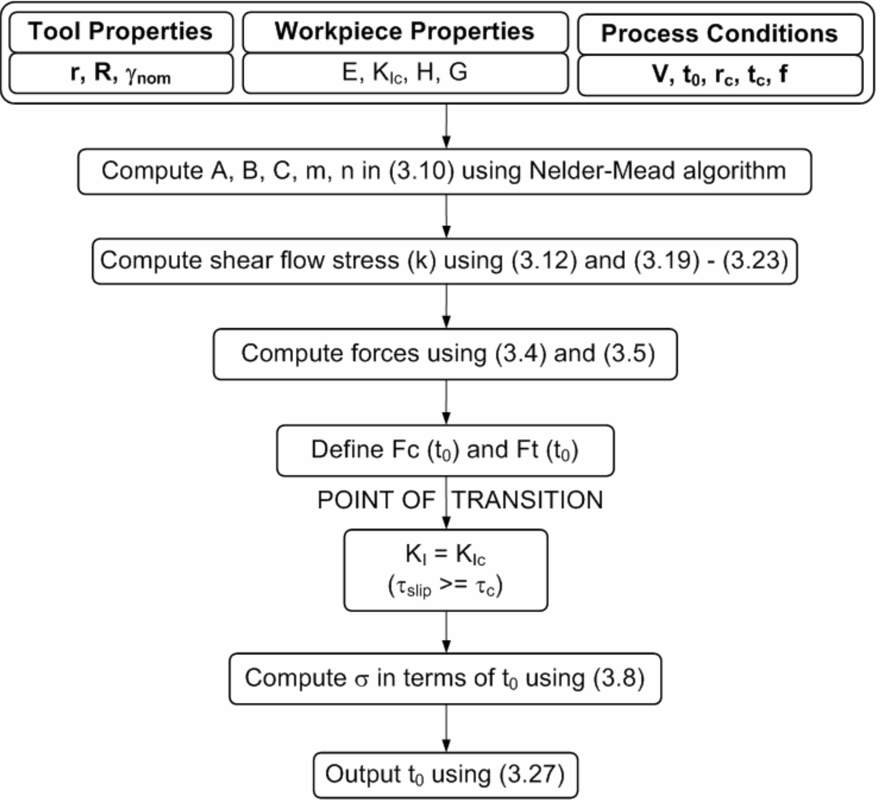

Figure 3.10 Schematic of comprehensive prediction model

The input to the model consists of properties of the workpiece including fracture toughness (K_{Ic}), elastic modulus (E), hardness (H), shear modulus (G) etc., tool geometry parameters including tool nose radius (R), tool edge radius (r) and nominal rake angle (γ_{nom}). The input to the model also includes process conditions such as undeformed chip thickness (t_0), cutting velocity (V), feed (f), cutting ratio (r_c) etc. The first step in the model computation involves the determination of constants A, B, C, m, n in the Johnson-Cook equation to compute the flow stress in (3.10) using the optimization procedure as discussed above. The shear flow stress is computed from (3.12) and (3.19)-(3.23). The cutting and thrust forces are determined using (3.4) and (3.5). The cutting and thrust forces are then defined as functions of undeformed chip thickness (F_c (t_0) & F_t (t_0)).

Comparing the stress intensity with the value of fracture toughness gives the value of the transition undeformed chip thickness. The undeformed chip thickness is also compared to the traditional model (Blake and Scattergood, 1990) as given in (2.4).

3.7 Experimental Set-Up

The experiments were performed on single crystal silicon using an ultraprecision lathe and a round nosed single crystal diamond tool. The details of the experimental set-up are given in this section.

Figure 3.11 Toshiba ULG-100C ultraprecision machine tool

Machine Tool: The end turning experiments were carried out on a Toshiba (ULG-100C) ultra-precision machine (Figure 3.11) with a position resolution of 1 *nm*. The maximum spindle speed achievable on this machine is 1500 *rpm*. The machine is also capable of achieving feed rates of 450 *mm/min*. The machine is fixed to shock reservoirs to make it vibration free and hence conducive for ultra-precision machining.

Workpiece Material: The workpieces used for the experiments were single crystal silicon wafers (Montco Silicon Technologies Inc.) with three different orientations viz. (100), (110), and (111). The wafers were polished on one side and were from the same lot. The (100) and (111) wafers were of a diameter of 50 *mm* and thickness of 0.5 *mm*. The (110) wafer was 100 *mm* in diameter and 0.5 *mm* in thickness. The (100) and (110) wafers were p-type while the (111) was an n-type wafer.

Tool: The cutting tool used was a single crystal synthetic diamond tool (round nosed) with a nominal rake angle of 0°, clearance angle of 7° and a nose radius of around 0.5 *mm*. A snapshot of the tool is shown in Figure 3.12.

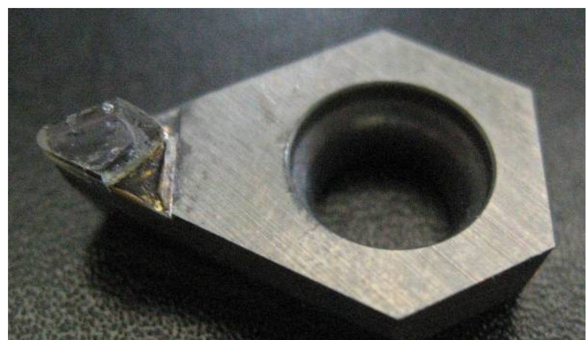

Figure 3.12 Single point synthetic diamond tool

End-Turning Operation: The silicon wafer (workpiece) was glued to an aluminum block (Figure 3.13) using heat-softened glue, which was then attached to the spindle through a vacuum chuck. The aluminum blocks were first machined to make the surface free of any waviness. It must be noted that no pre-trimming was performed on the silicon wafer before performing the actual cutting experiments. This may be an issue because the glue

on which the silicon wafer is held may not be applied evenly and hence the flatness of the wafer may be affected.

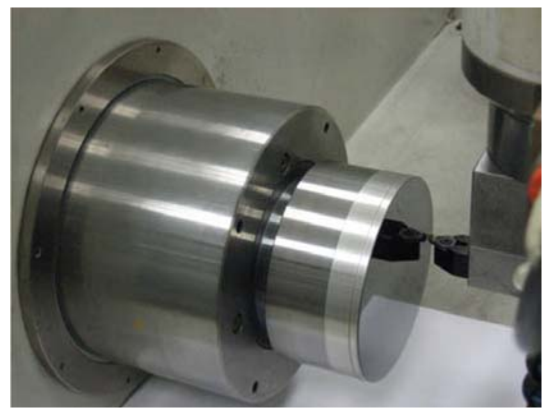

Figure 3.13 End turning set-up on the ultraprecision machine tool

3.8 Experimental Procedure and Results

3.8.1 Force Measurements

The experimental plan for validating the model is shown in Table 3-3. All three orientations of single crystal silicon were machined at two feeds and depth of cut ranging from 0.3 – 100 μm.

Table 3-3 Experimental plan for single crystal silicon

Workpiece	Feed (μm/rev)	Depth of Cut (μm)	Cutting Velocity (m/sec)
Silicon (100)	1	0.3, 1, 2.5, 5, 10, 20, 50, 100	1.1257
	2	0.3, 0.5, 0.8, 1, 2, 5, 10, 20	
Silicon (110)	1	0.3, 1, 2.5, 5, 10, 20, 50, 100	1.1257
	2	0.3, 0.6, 1, 2, 5, 10, 20, 25	
Silicon (111)	1	0.3, 1, 2.5, 5, 10, 20, 50, 100	1.1257
	2	0.3, 0.5, 0.8, 1, 2, 5, 10, 20	

The forces were measured using a three-axis dynamometer (Kistler 9256A1) and digitally recorded (Sony PC204Ax). The force data was then downloaded into a computer

using special software (PC Scan II). The forces were recorded at a sampling frequency of 24 KHz. The values of forces shown in the plots below were measured when the cutting had reached a steady state. The measured forces for feeds of 1 *μm/rev* and 2 *μm/rev* are shown in Figures 14-16 and Figures 17-18 respectively.

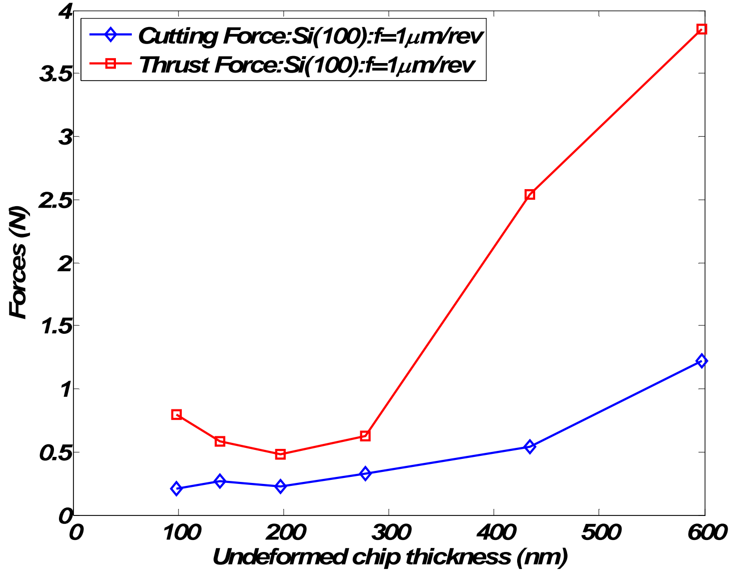

Figure 3.14 Experimental forces measured for Si (100) and f = 1 μm/rev

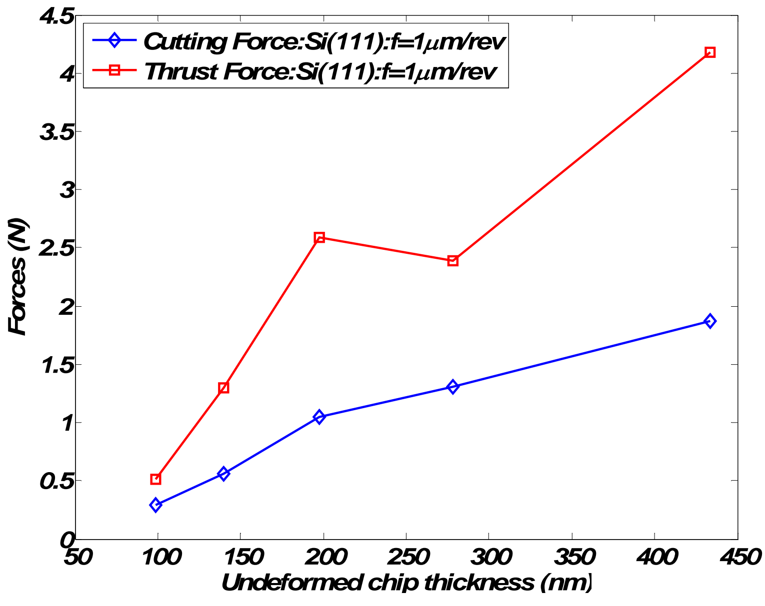

Figure 3.15 Experimental forces measured for Si (111) and f = 1 μm/rev

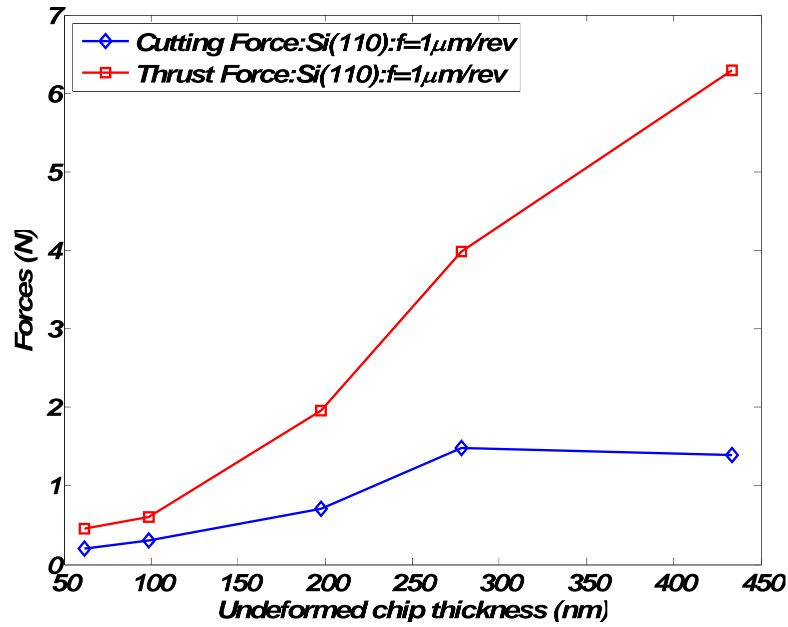

Figure 3.16 Experimental forces measured for Si (110) and f = 1 μm/rev

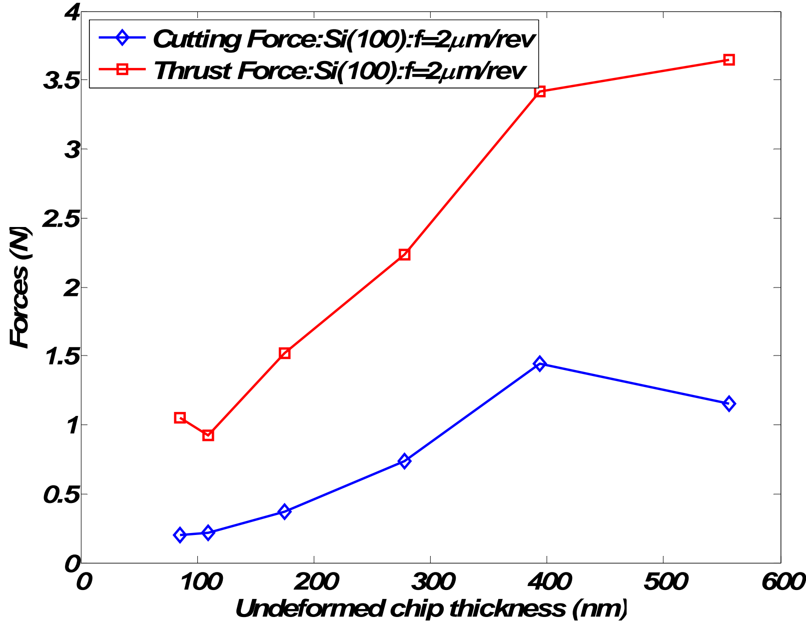

Figure 3.17 Experimental forces measured for Si (100) and f = 2 μm/rev

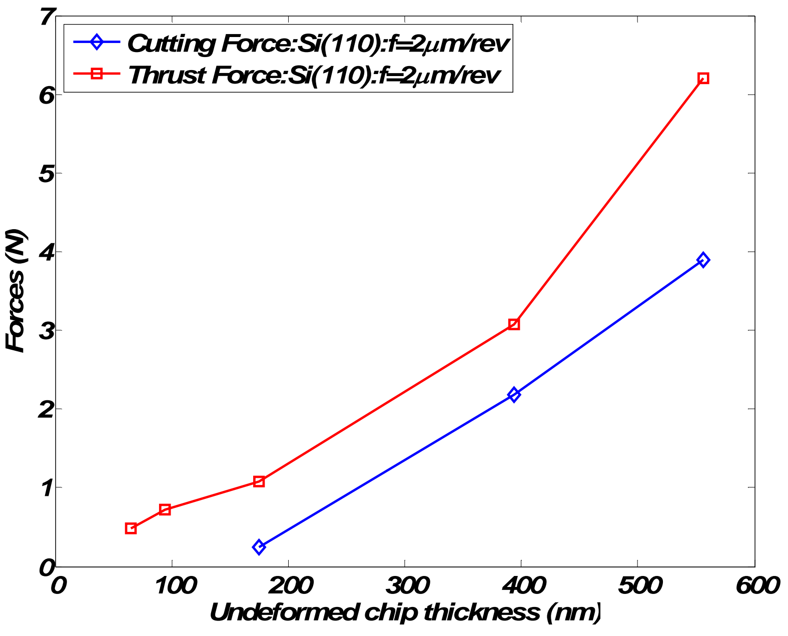

Figure 3.18 Experimental forces measured for Si (110) and f = 2 μm/rev

3.8.2 Surface Texture

The surface finish of the machined silicon wafers were investigated under a scanning electron microscope (SEM). The silicon wafer surface was not evenly cut throughout the circumference of the workpiece, as the tool lost contact with the workpiece for some portions of the workpiece. The reason for this, as stated earlier, could be from the unevenness caused by the glue which is used to secure the workpiece to the aluminum block on the spindle. In order to overcome this discrepancy the depth to which the tool actually cut the material was investigated using a Taylor Hobson surface profilometer. The maximum error in the depth of cut was found to be around 7% as shown in Table 3-4.

Table 3-4 Depth of cut measurements

Depth of cut measurements	Profile
Commanded depth – 2.0 µm Actual depth – 1.9372 µm Error – 3.14%	
Commanded depth – 10.0 µm Actual depth – 9.2983 µm Error – 7.07%	
Commanded depth – 20.0 µm Actual depth – 19.2982 µm Error – 7.02%	
Commanded depth – 50.0 µm Actual depth – 47.5877 µm Error – 4.83%	

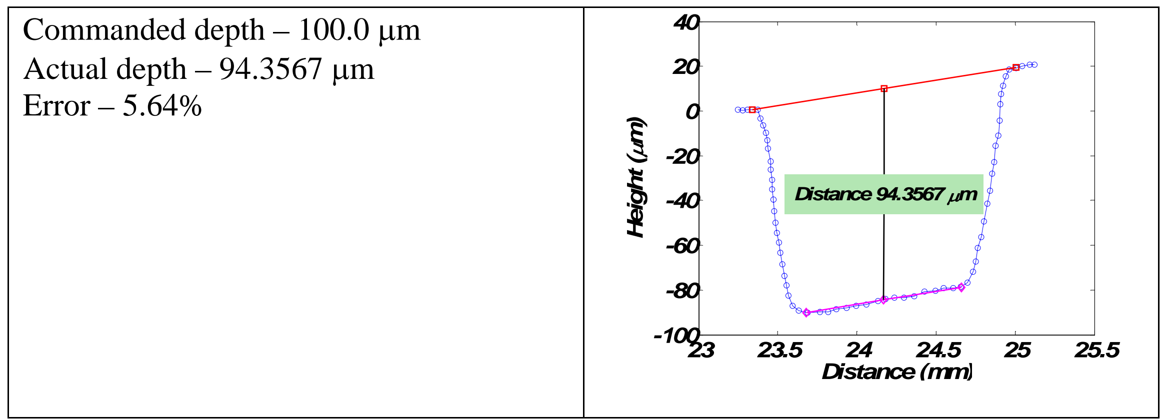

The texture of the machined surface was investigated using an SEM (LEO 1530). Figure 3.19 shows the surface texture for different values of undeformed chip thickness for Si (111) and f = 1 µm/rev.

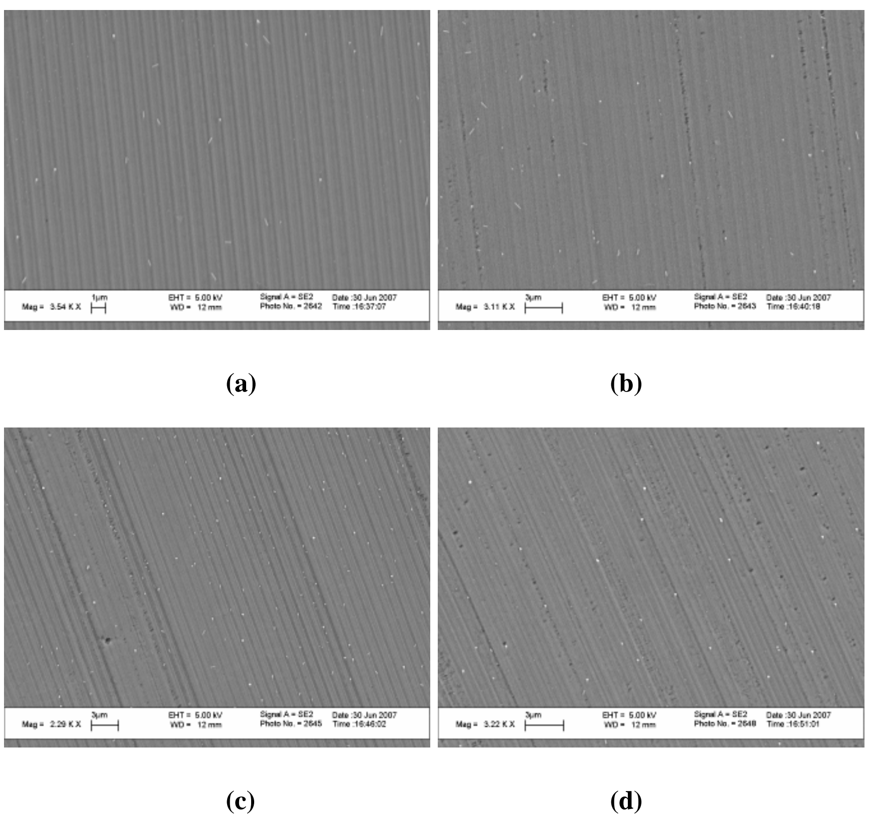

(a) (b)

(c) (d)

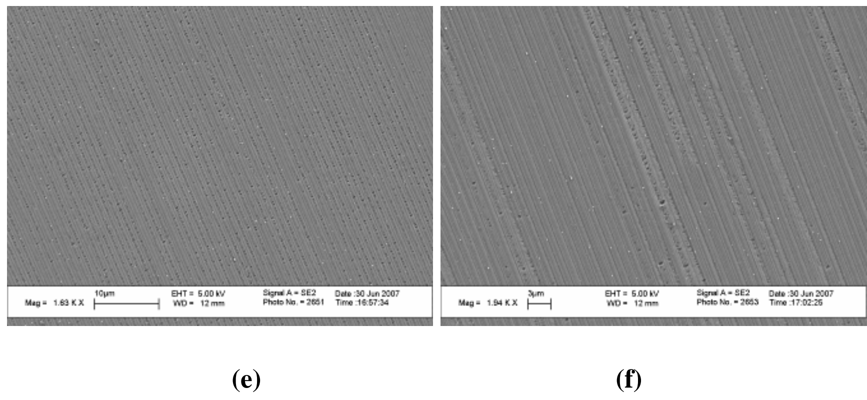

(e) **(f)**

Figure 3.19 Surface texture for undeformed chip thickness values of a) 62 nm, b) 99 nm, c) 140 nm, d) 197 nm, e) 434 nm, and f) 598 nm for Si (111) and f = 1 μm/rev

The surface texture in Figure 3.19a is very smooth without any damages such as cracks, micro-craters, surface pits etc. The lines across the surface are feed marks from the tool as it removes material from the surface. The surface in Figure 3.19b is largely smooth with very few micro crater features. As the undeformed chip thickness value increases, the surface has more pronounced craters and pits being formed on the surface as can be seen in Figure 3.19e and Figure 3.19f. From Figure 3.19 it can be seen that the transition probably occurs in the range of 60 – 100 nm.

3.8.3 Surface Roughness

The surface roughness of the machined silicon wafers is characterized by roughness parameters viz. peak-to-valley roughness (R_t) and average roughness (R_a). In the process of turning (regular turning or end turning) the theoretical surface roughness depends on the tool geometry and feed as shown in Figure 3.20.

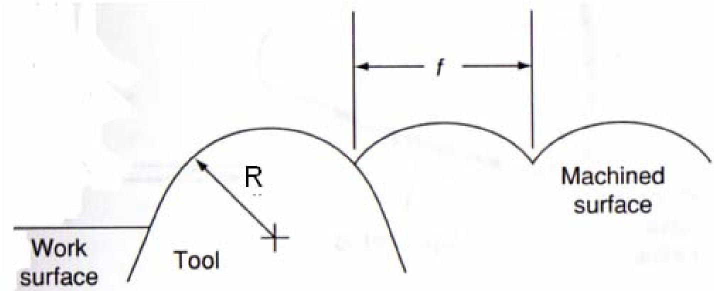

Figure 3.20 Roughness when turning with a tool having a nose radius

In the case of end turning of silicon, the tool has a finite nose radius and hence the roughness is a function of the feed *(f)* and the tool nose radius *(R)* and is given by (Stephenson and Agapiou, 2006):

$$R_t = \frac{f^2}{8R}$$
$$R_a = \frac{0.0321 f^2}{R} \tag{3.30}$$

The theoretical roughness values for the case of R = 0.5 *mm* and f = 1, 2 *μm/rev* are given in Table 3-5. The computed values suggest that a highly smooth surface finish is produced for the experimental conditions given in Table 3-3.

Table 3-5 Theoretical roughness for end turning of silicon

R (mm)	f (μm/rev)	R_a (nm)	R_t (nm)
0.5	1	0.0642	0.25
0.5	2	0.2568	1.00

The surface roughness for the machined surfaces was measured using a white light interferometer (Zygo NewView 100) and the results are shown in Figure 3.21,

Figure 3.22, Figure 3.23 for Si (100), Si (110) and Si (111) respectively. In Figure 3.21, the roughness values for a feed of 1 *μm/rev* is higher than for the case of the $f = 2$ *μm/rev*. This trend is opposite of the theoretical prediction which indicates that the roughness is directly proportional to the square of the feed. In Figure 3.22, the results are mixed in that some values for roughness are higher for f = 2 *μm/rev*. However, in Figure 3.23 the roughness values for the higher feed are greater than those obtained for the lower feed. The surfaces as viewed on a Zygo for Si (100) and $f = 1$ *μm/rev* are shown in Figure 3.24.

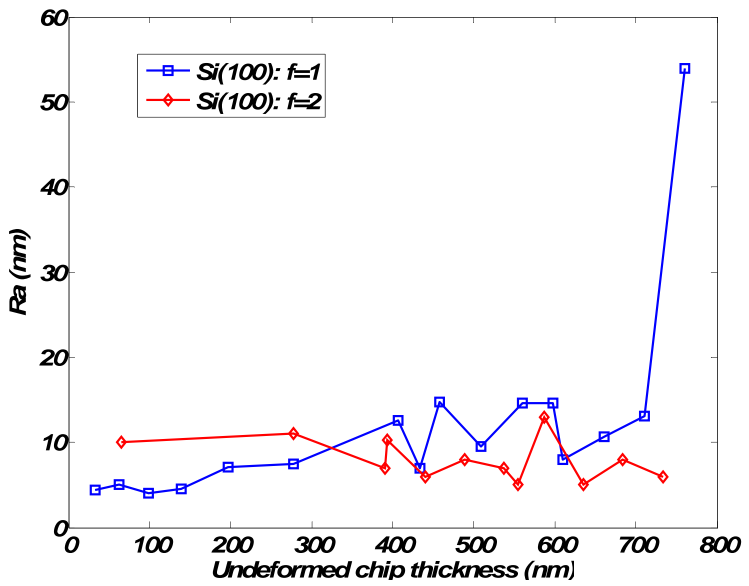

Figure 3.21 Surface roughness for Si (100)

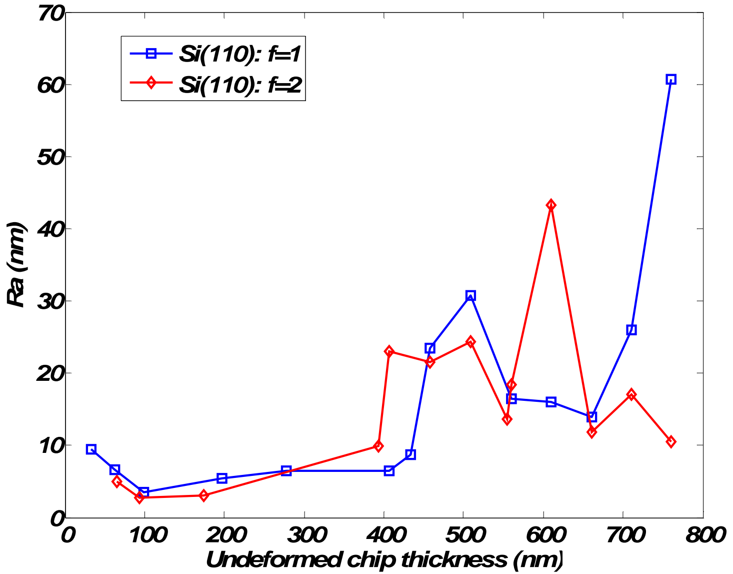

Figure 3.22 Surface roughness for Si (110)

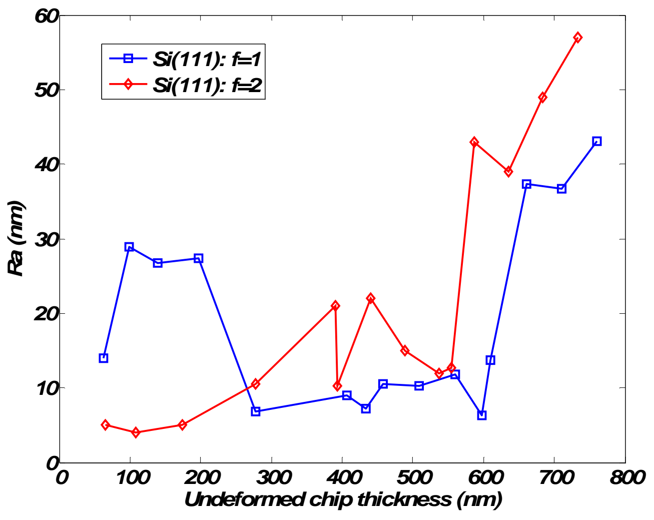

Figure 3.23 Surface roughness for Si (111)

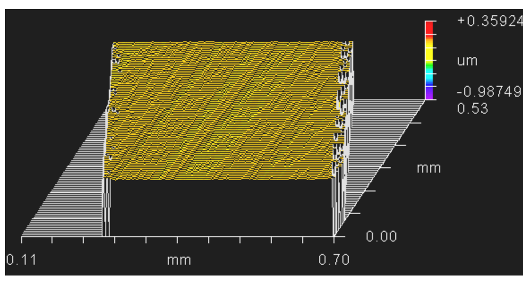

undeformed chip thickness – 34 nm (R_a = 4.44 nm)

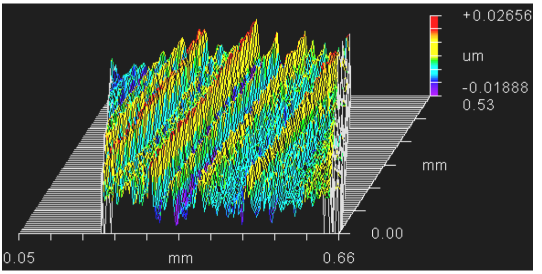

undeformed chip thickness – 62 nm (R_a = 5.05 nm)

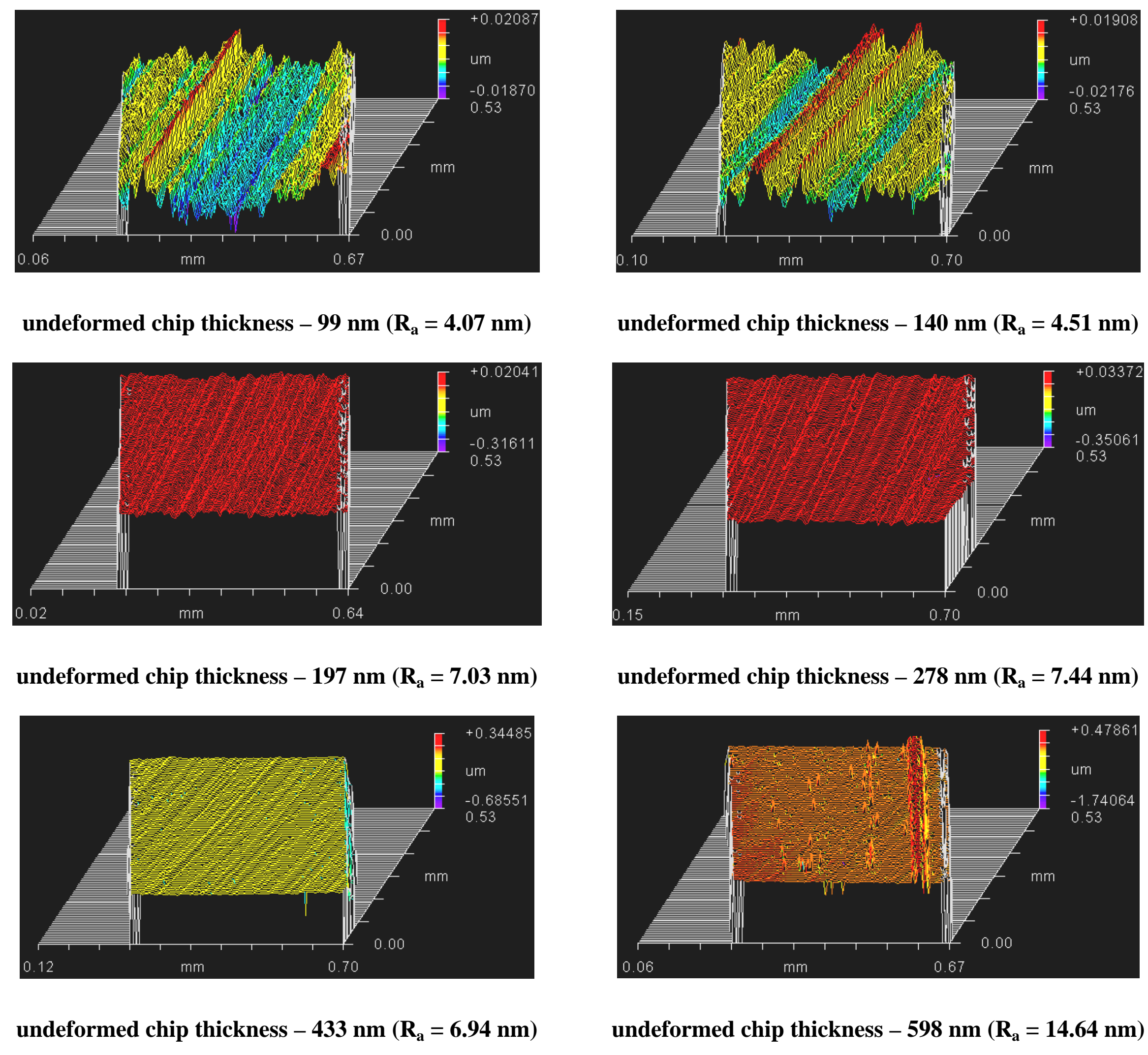

undeformed chip thickness – 99 nm (R_a = 4.07 nm)

undeformed chip thickness – 140 nm (R_a = 4.51 nm)

undeformed chip thickness – 197 nm (R_a = 7.03 nm)

undeformed chip thickness – 278 nm (R_a = 7.44 nm)

undeformed chip thickness – 433 nm (R_a = 6.94 nm)

undeformed chip thickness – 598 nm (R_a = 14.64 nm)

Figure 3.24 Surface roughness profiles for Si (100) and f = 1 μm/rev measured using Zygo

3.8.4 Chip Formation

The process of ductile-regime machining produces chips of two types viz. continuous ductile chips and discontinuous brittle chips. Continuous chips are formed when the mode of material removal is plastic deformation while discontinuous (brittle) chips are formed when the mode of material removal is fracture. In this experiment, it was found that there was evidence of continuous chip formation (Figure 3.26) indicating that plastic deformation occurred rather than brittle fracture. However, the process of

collecting chips was extremely difficult especially for very undeformed chip thickness values. The nature of the collected chips was investigated under the SEM.

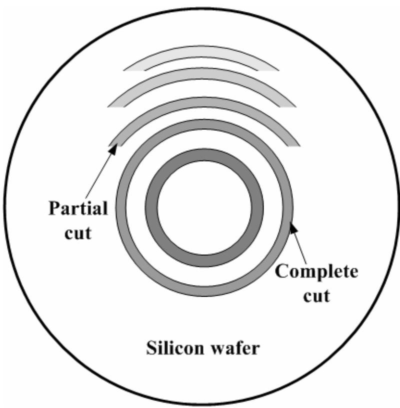

Figure 3.25 Schematic of cut silicon wafer surface

As stated earlier, the silicon wafer (workpiece) was mounted to an aluminum block using heat softening glue. Due to the presence of glue the surface was not flat and as a result the tool would contact the workpiece at specific locations only (Figure 3.25). It was thus very difficult to accurately pinpoint the exact undeformed chip thickness of the ductile chips. The chip could be formed at any region with the surface where the tool was in touch with the surface. Usually, in such situations, a pre-trimming cut is performed to ensure flatness of the surface. But performing a pre-trimming cut causes inconsistencies in the new surface and hence no pre-trimming was performed for this experiment.

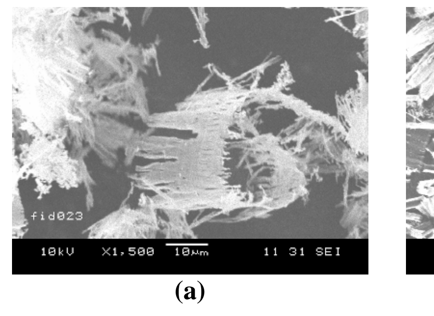

(a)

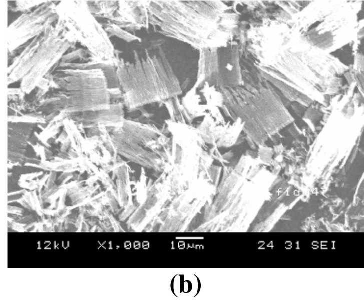

(b)

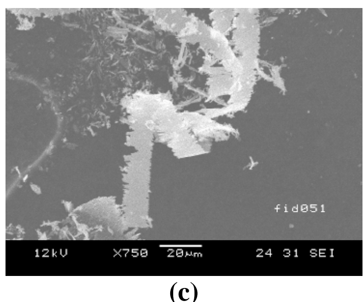

(c)

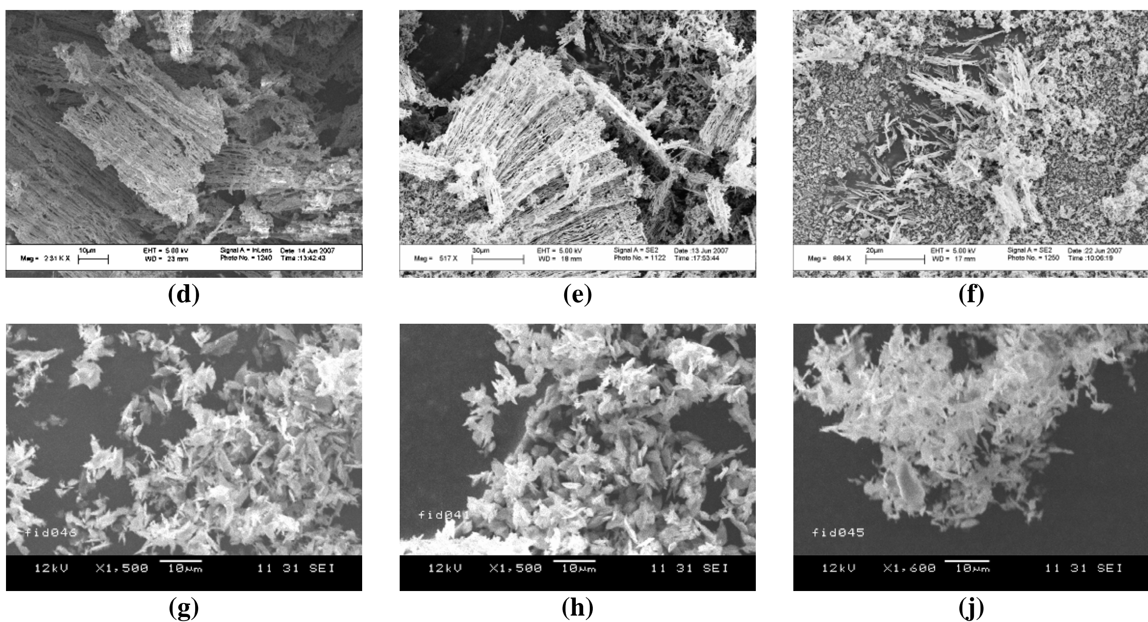

Figure 3.26 Types of chip formation in silicon machining: ductile ((a) – (c)), ductile-brittle ((d) – (f)), brittle ((g) – (j))

3.9 Simulation Results and Model Comparison

The determination of the undeformed chip thickness includes the determination of the constants for the Johnson-Cook model, the computation of forces and the determination of normal stresses on the shear plane. The constants for the Johnson-Cook equation, which describes the relationship between the material flow stress and strain, strain rate and temperature, was determined using an optimization procedure as described earlier.

The force model described above is for the case of orthogonal machining where the cutting edge is perpendicular to the direction of the cutting velocity. However, the experimental process investigated was end turning and hence the forces have to be transformed in order to make an effective comparison. Once the forces are obtained, the next step involves the determination of the stresses on the shear plane. The stress intensity factor due to these stresses is determined and compared to the fracture

toughness of the material which in this case is silicon. The critical undeformed chip thickness is obtained based on fact that the stress intensity factor equals the fracture toughness at the point of transition from the ductile to the brittle regime.

3.9.1 Determination of Forces

The terminology used in turning is different from that used in orthogonal machining and as stated earlier, a transformation between the forces of the two processes is required. The feed in turning is equivalent to depth of cut in orthogonal cutting and the depth of cut in turning is equivalent to width of cut in orthogonal cutting as shown in Figure 3.27. The depth of cut in orthogonal cutting is also known as undeformed chip thickness and is the term used in this thesis.

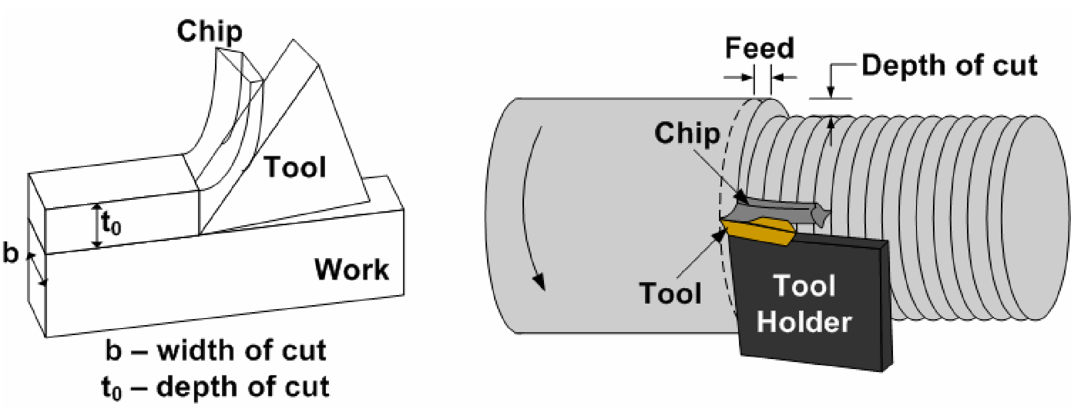

Figure 3.27 Orthogonal cutting vs. turning

Determination of Tool Edge Radius: The determination of tool edge radius involves a procedure outlined in Li et al. (2003b) and consists of the following steps: The first task involves indenting a new tool on a perfectly flat piece of copper. Copper was chosen as the indentation material as it had a high elastic modulus and low yield strength besides

having high machinability. The indentation on copper was performed at three different depths of 0.2, 0.5 and 0.8 μm. A sample photomicrograph of a 0.5 μm indentation is shown in Figure 3.28.

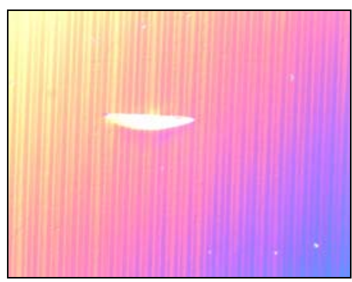

Figure 3.28 Indentation of tool on copper for edge radius measurement

The indentation on the copper workpiece is then measured on an atomic force microscope (AFM, SEIKO II SPA 500). The software associated with the AFM allows for the study of the tool edge profile as shown in Figure 3.29.

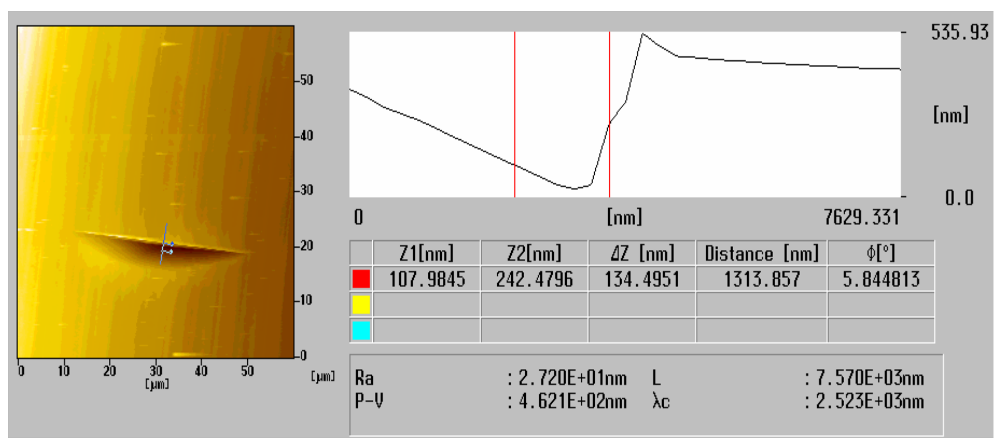

Figure 3.29 Measurement of tool edge radius on an AFM

The profile of the tool is then exported to matlab and a simple trigonometric procedure to fit a circle to three points along its edge radius is performed. The mathematical procedure

is explained for completeness. Consider a set of three points $P_1(x_1, y_1)$, $P_2(x_2, y_2)$ and $P_3(x_3, y_3)$ that lie along the radius of the tool as shown in Figure 3.30.

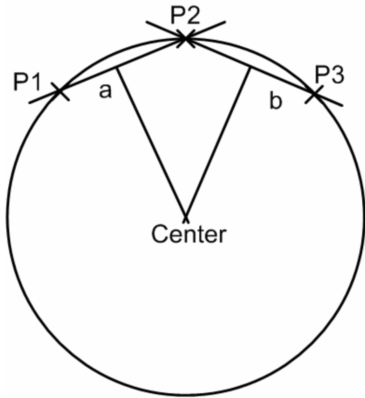

Figure 3.30 Fitting a circle to three points

The line '*a*' passes through the first two points P_1 and P_2. The line '*b*' passes through the next two points P_2 and P_3. The equations of these two lines are

$$y_a = m_a(x - x_1) + y_1 \quad and \quad y_b = m_b(x - x_2) + y_2 \tag{3.31}$$

where m_a and m_b are the slopes of the two lines. The slopes are given by the following equation

$$m_a = \frac{y_2 - y_1}{x_2 - x_1} \quad and \quad m_a = \frac{y_3 - y_2}{x_3 - x_2} \tag{3.32}$$

The centre of the circle is the intersection of the two lines perpendicular to and passing through the midpoints of the lines P_1P_2 and $P_2\ P_3$. The perpendicular of a line

with slope m has slope $-1/m$, thus equations of the lines perpendicular to lines '*a*' and '*b*' and passing through the midpoints of P_1P_2 and P_2P_3 are given by (3.33). These two lines intersect at the centre of the circle and hence solving for x gives (3.34). The value of y can be calculated by substituting the x value into one of the equations of the perpendiculars. The radius is the distance between any one of the points, for example the point P_1 and the center.

$$\begin{aligned} y_a^{'} &= -\frac{1}{m_a}\left(x - \frac{x_1 + x_2}{2}\right) + \frac{y_1 + y_2}{2} \\ y_b^{'} &= -\frac{1}{m_b}\left(x - \frac{x_2 + x_3}{2}\right) + \frac{y_2 + y_3}{2} \end{aligned} \tag{3.33}$$

$$x = \frac{m_a m_b (y_1 - y_3) + m_b (x_1 + x_2) - m_a (x_2 + x_3)}{2(m_b - m_a)} \tag{3.34}$$

The computation described above was carried out in Matlab®. The results of the computations are shown in Figure 3.31. The radius of the circle was affected by the choice of the three points along the profile of the tool. Hence a number of different points were chosen from different profiles and an average value was computed. The average edge radius for the tool used in the experimentation was computed to be 225 nm. But this measurement is not accurate because there is some amount of springback in the copper material after the process of indentation. The measurements obtained from the AFM are enlarged by a factor of 1.5 (Li et al., 2003b) and hence the compensated edge radius is 150 nm.

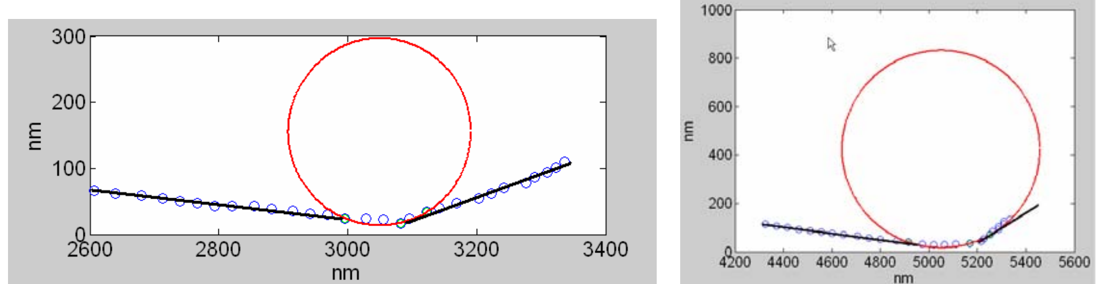

Figure 3.31 Computation of edge radius of the tool using Matlab®

Undeformed Chip Thickness vs Depth of Cut: The maximum undeformed chip thickness is computed based on the cutting tool geometry and the cutting conditions. It is related to the feed f, tool nose radius R and the depth of cut a_0. The two scenarios for determining the maximum undeformed chip thickness is shown in Figure 3.32. The centers O_1 and O_2 represent the centers of two consecutive cutting edges and the distance between the two centers represents the feed. For the machining conditions shown in Table 3-3, the undeformed chip thickness computation results are shown in Table 3-6.

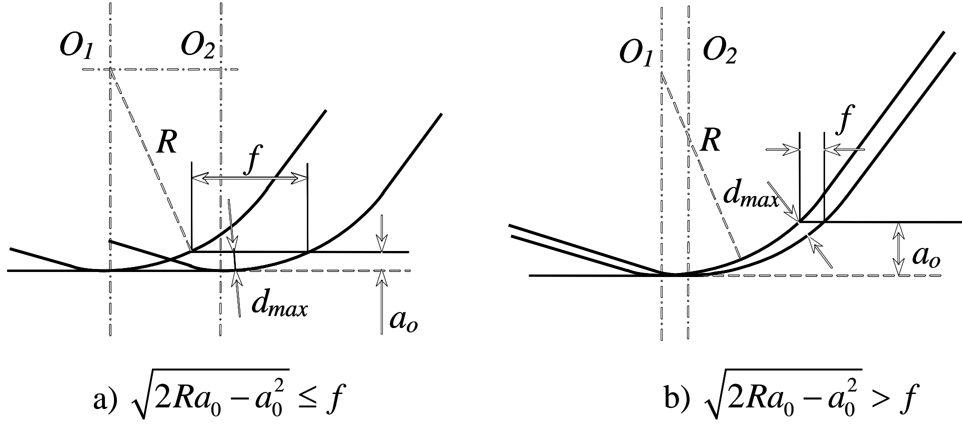

Figure 3.32 Schematic for determining maximum undeformed chip thickness (Liu K., 2002)

The equations for the two cases are given by the following:

$$d_{\max} = \begin{cases} a_0, & if\ \sqrt{2Ra_0 - a_0^2} \le f \\ R - \sqrt{R^2 + f^2 - 2f\sqrt{2Ra_0 - a_0^2}}, & if\ \sqrt{2Ra_0 - a_0^2} > f \end{cases} \tag{3.35}$$

Table 3-6 Computation of undeformed chip thickness (UCT)

Depth of cut (μm)	Feed (μm/rev)	R (mm)	$\sqrt{2Ra_0 - a_0^2}$ (m)	UCT (nm)
0.3	1	0.5	1.7318e-005	33.64
0.8	2	0.5	2.8273e-005	109.10
1	2	0.5	3.1607e-005	122.44
2	2	0.5	4.4677e-005	174.74
2.5	1	0.5	4.9937e-005	98.89
5	2	0.5	7.0534e-005	278.21
50	1	0.5	2.1794e-004	435.08
100	1	0.5	3.0000e-004	599.36

Effect of Tool Nose Radius: A tool with a nose radius, as opposed to a sharp tool, affects the chip flow direction and ultimately the cutting forces in turning. Oxley (1989) details the methodology to determine the chip flow direction and an equivalent side cutting edge angle which is then used to determine the cutting forces. The existence of tool nose radius presents two scenarios: (i) the depth of cut is such that only the round part of the nose is a part of cutting and (ii) the depth of cut is such that the cutting extends beyond the tool nose. The two scenarios of cutting with a nose radius tool are depicted in Figure 3.33.

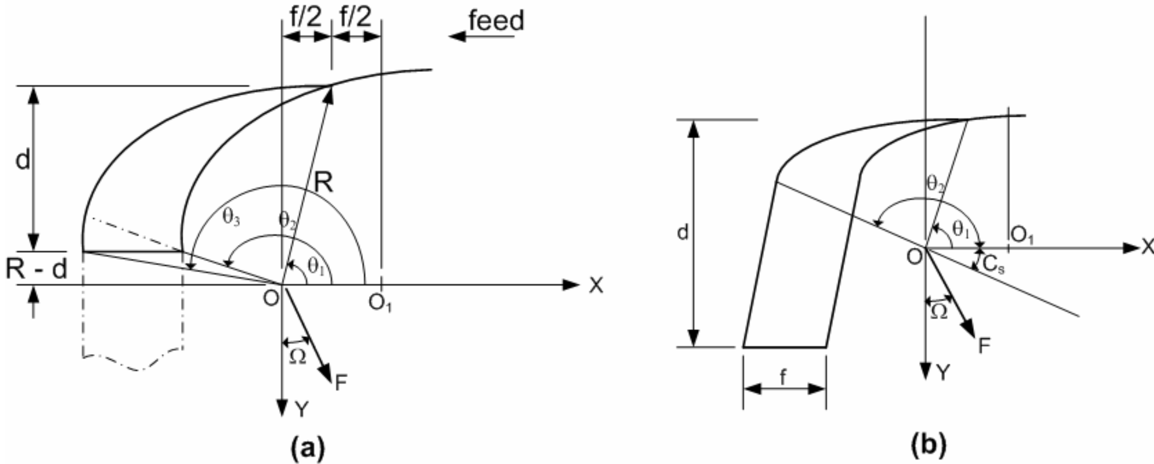

Figure 3.33 Geometry of chip flow for nose radius tools (Oxley, 1989)

Case I (Figure 3.33a), d < R (1 – sinC$_s$)

The first case involves cutting only along some part of the nose radius as the depth of cut is very small; this case is representative of micromachining conditions. The angle C_s is the side cutting edge angle which is usually a part of the tool manufacturer's specifications. The chip flow direction is given by

$$\Omega = \tan^{-1}\left(\frac{NUM}{DEN}\right) \tag{3.36}$$

where the *NUM* (numerator) and *DEN* (denominator) are given by the following equations:

$$\begin{aligned} NUM =& \left[-R\sin\theta\right]_{\theta_1}^{\theta_3} + \frac{1}{2}\left[\sin\theta(R^2 - f^2\sin^2\theta)^{1/2} + \frac{R^2}{f}\sin^{-1}\left(\frac{f}{R}\sin\theta\right)\right]_{\theta_1}^{\theta_2} + \\ &+ f\left[\frac{\sin(2\theta)}{4} + \frac{\theta}{2}\right]_{\theta_1}^{\theta_2} + \left[(R-d)\ln(\sin\theta)\right]_{\theta_2}^{\theta_3} \end{aligned} \tag{3.37}$$

$$DEN = \left[-R\cos\theta\right]_{\theta_1}^{\theta_3} + \frac{1}{2}\left[\cos\theta(R^2 - f^2\sin^2\theta)^{1/2} + \frac{R^2 - f^2}{f}\ln\left\{(f\cos\theta) + \right.\right.$$

$$\left.\left. + \left(R^2 - f^2\sin^2\theta\right)^{1/2}\right\}\right]_{\theta_1}^{\theta_2} + \frac{f}{4}\left[\cos(2\theta)\right]_{\theta_1}^{\theta_2} + \left[-(R-d)\theta\right]_{\theta_2}^{\theta_3} \qquad (3.38)$$

The limits of integration for the equations (3.37) and (3.38) are given by

$$\theta_1 = \cos^{-1}\left(\frac{f}{2R}\right)$$

$$\theta_2 = \pi - \tan^{-1}\left[\frac{R-d}{\left(2Rd - d^2\right)^{1/2} - f}\right] \qquad (3.39)$$

$$\theta_3 = \pi - \sin^{-1}\left(\frac{R-d}{R}\right)$$

Case II (Figure 3.33b), $d > R\,(1 - \sin C_s)$

The second case involves cutting at a depth which is greater than the tool nose radius. The chip flow direction is given by (3.36) where *NUM* and *DEN* is as follows:

$$NUM = \left[-R^2\sin\theta\right]_{\theta_1}^{\theta_2} + \frac{R}{2}\left[\sin\theta(R^2 - f^2\sin^2\theta)^{1/2} + \frac{R^2}{f}\sin^{-1}\left(\frac{f}{R}\sin\theta\right)\right]_{\theta_1}^{\theta_2} +$$

$$+ Rf\left[\frac{\sin(2\theta)}{4} + \frac{\theta}{2}\right]_{\theta_1}^{\theta_2} + \left[f\left\{d - R\left(1 - \sin C_s\right)\right\} - \frac{f^2}{4}\sin(2C_s)\right]\cos C_s \qquad (3.40)$$

$$DEN = \left[-R^2 \cos\theta\right]_{\theta_1}^{\theta_2} + \frac{R}{2}\left[\cos\theta(R^2 - f^2\sin^2\theta)^{1/2} + \frac{R^2 - f^2}{f}\ln\left\{(f\cos\theta) + \right.\right.$$

$$\left.\left. + \left(R^2 - f^2\sin^2\theta\right)^{1/2}\right\}\right]_{\theta_1}^{\theta_2} + \frac{Rf}{4}\left[\cos(2\theta)\right]_{\theta_1}^{\theta_2} + \left[f\left\{d - R(1 - \sin C_s)\right\} - \right. \tag{3.41}$$

$$\left. - \frac{f^2}{4}\sin(2C_s)\right]\sin C_s$$

The limits of integration for equations (3.40) and (3.41) are given by

$$\theta_1 = \cos^{-1}\left(\frac{f}{2R}\right)$$
$$\theta_2 = \pi - C_s \tag{3.42}$$

The equivalent side cutting edge angle (C_s^*) required for force computation is given in relation to the direction of chip flow by (3.43). Table 3-7 shows the results of the computation for the ship flow direction and the equivalent side cutting edge angle for some conditions.

$$C_s^* = \frac{\pi}{2} - \Omega \tag{3.43}$$

Table 3-7 Computation results for chip flow direction and equivalent side cutting edge angle

Depth of cut (μm)	Feed, f (μm/rev)	R (mm)	Ω (deg)	C_s^* (deg)
0.3	1	0.5	1.266	88.734
0.8	2	0.5	2.047	87.953
1	2	0.5	2.302	87.698
2	2	0.5	3.303	86.697
2.5	1	0.5	3.764	86.236
5	2	0.5	5.291	84.709
50	1	0.5	17.122	72.878
100	1	0.5	24.376	65.624

Width of Cut: The width of cut in orthogonal cutting is represented by the depth of cut in turning, but it is influenced by the presence of the tool nose radius, which is the case in the experiments discussed earlier. In order to determine the width of cut two methods were compared (Figure 3.34). From Figure 3.33a, it can be seen that only the tool nose section is involved in the cutting process and hence the width of cut can be approximated as the length of the arc. Therefore the length of the arc can be given by (Oxley, 1989):

$$w = R(\theta_3 - \theta_1) \tag{3.44}$$

Another analysis from Waldorf (2004) suggests replacing the orthogonal width of cut with the cutting edge length for a standard turning operation using (3.45). The method suggested by Waldorf is used in this thesis.

$$w = R\left(\frac{\pi}{2} - C_s^* + \sin^{-1}\left(\frac{f}{2R}\right)\right) + \frac{d - R(1 - \sin(C_s^*))}{\cos(C_s^*)} \tag{3.45}$$

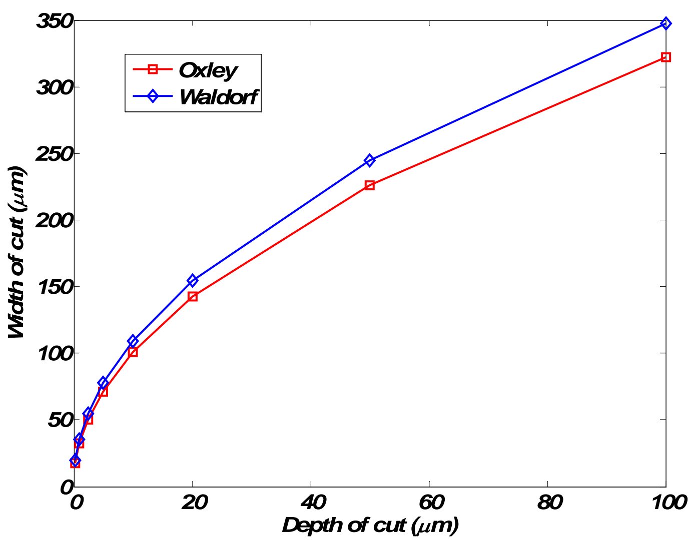

Figure 3.34 Comparison between Oxley and Waldorf for computing width of cut

Strain and Strain-rate: The shear strain and strain-rate are computed based on the model by Oxley (1989) and Manjunathaiah and Endres (2000). A comparison of the shear strain between the two models is shown in Figure 3.35a. The shear strain predicted between the two models is of the same order of magnitude and trend. But Oxley's model predicts a higher value for the shear strain. The comparison of shear strain-rate has a comparatively better agreement between the two models. The results shown in Figure 3.35b are of the same order of magnitude and trend, and Oxley's model predicts a higher value for shear strain-rate. As indicated earlier, Manjunathaiah and Endres' model is used in this thesis work.

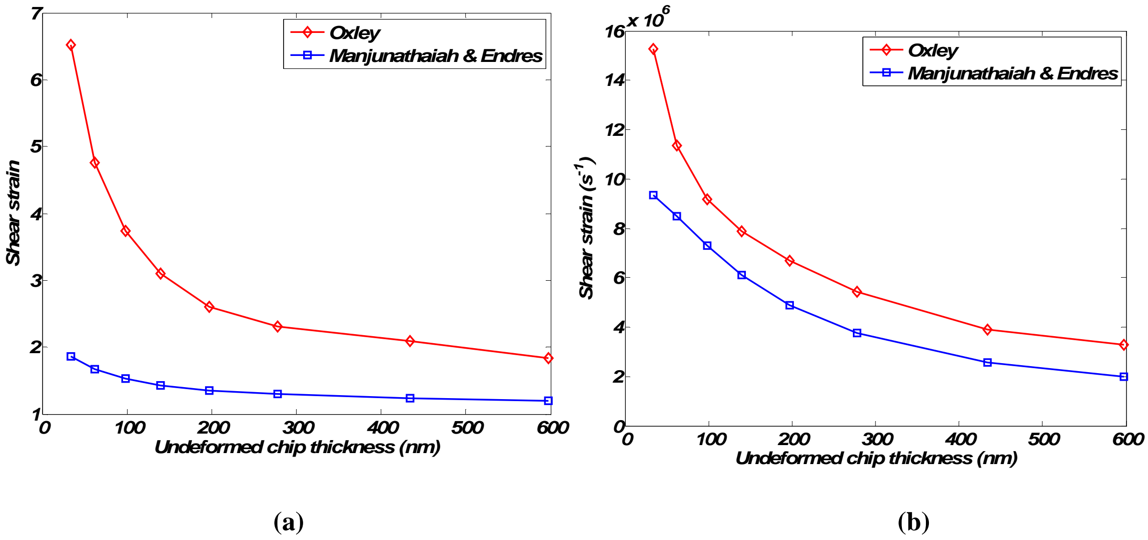

Figure 3.35 Comparison of (a) shear strain and (b) strain-rate for a nominal rake angle $\gamma = 0^o$ and cutting velocity V = 1.1257 m/sec

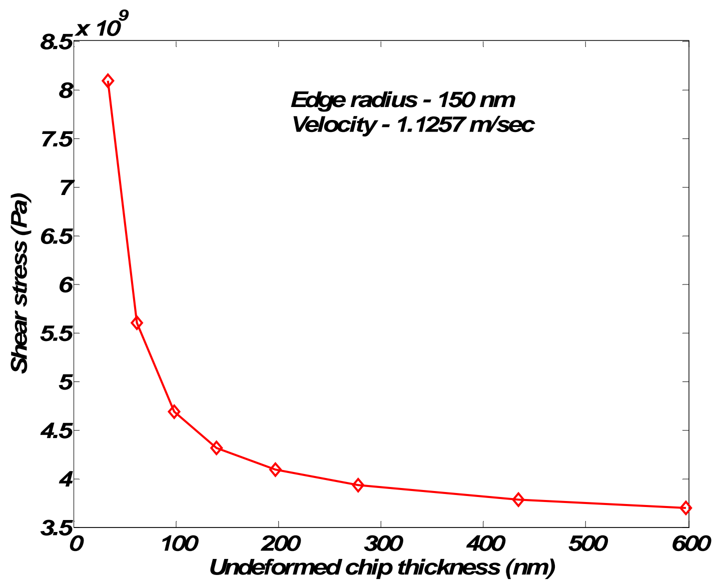

Figure 3.36 Shear flow stress vs undeformed chip thickness

Shear Flow Stress: The shear flow stress (k) is computed using (3.12) and the results are shown in Figure 3.36. The flow stress increases with decrease in undeformed chip thickness and the reasons for this trend are related to strain and strain-rate hardening.

Computation of Forces: The cutting and thrust forces are computed using (3.4) and (3.5). The term k_s, which denotes the shear flow stress, in the cutting and thrust force equations is computed as given by (3.12).

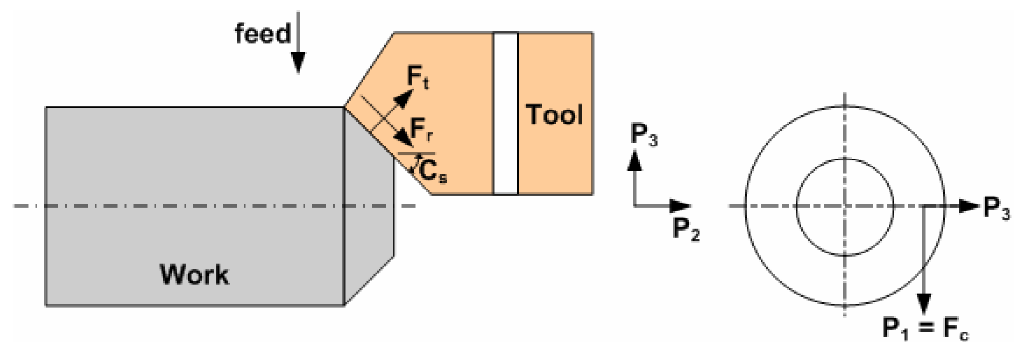

Figure 3.37 Oblique cutting geometry

In order to compare experimental and simulated forces, a transformation of the simulated forces is required. The reason for the transformation is that the force model developed is for orthogonal machining while the experimental forces were measured for end-turning experiments. Oxley (1989) gave a transformation methodology for oblique machining which is shown in Figure 3.37. The relationship between the cutting (F_c), thrust (F_t) and radial (F_r) forces and the three orientation axes P_1, P_2 and P_3 are given by the following equation

$$
\begin{aligned}
P_1 &= F_c \\
P_2 &= F_t \sin C_s + F_r \cos C_s \\
P_3 &= F_t \cos C_s - F_r \sin C_s
\end{aligned}
\tag{3.46}
$$

In our scenario, the machining is orthogonal and hence the radial force component is zero. The measured forces also had only two components in mutually orthogonal directions and the third component was very close to zero. The side cutting edge angle (C_s) in (3.46) is replaced by the equivalent side cutting edge angle (C_s^*) which is determined using (3.43). A comparison between experimental and predicted cutting and thrust forces for Si (111) and f = 1 $\mu m/rev$ is shown in Figure 3.38. The prediction agrees very well with experimental values.

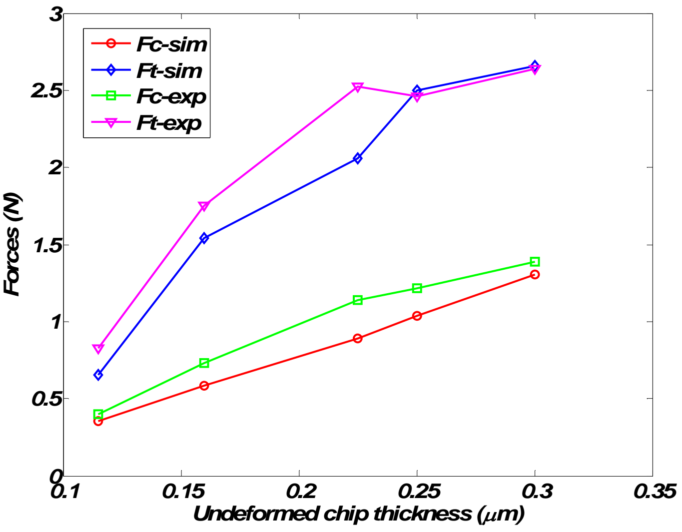

Figure 3.38 Comparison between experimental and predicted force values

Sensitivity Analysis: In order to determine the variation of forces with respect to input process parameter a sensitivity analysis was performed. A three-level, five factor full factorial design (3^5 = 243 runs) is adopted to determine the variation of output parameters to changes in the input data set. The design is summarized in Table 3-8.

Table 3-8 Full factorial design for sensitivity analysis

Factor	Low	Medium	High
Friction coefficient (μ)	0.2	0.3	0.4
Chip ratio (r_c)	0.25	0.3	0.35
Nominal rake angle (γ – degrees)	0	-20	-45
Tool edge radius (R – nm)	100	150	200
Undeformed chip thickness (t_0 – nm)	50	100	150
Responses – Cutting force (F_c), Thrust Force (F_t), Shear angle (φ)			

The main effects plots for the cutting force, thrust force, and shear angle are shown in Figure 3.39, Figure 3.40 and Figure 3.41 respectively. The results show that the cutting force is strongly influenced by the undeformed chip thickness and tool edge radius as expected. The coefficient of friction, chip ratio and nominal rake angle have a small influence on the cutting force. Due to the presence of tool edge radius the forces are influenced more by the effective rake angle, which is highly negative, compared to the nominal rake angle. The coefficient of friciton is usually a major contributor towards changes in cutting forces. But in this case the influence is not significant, which could be due to the very small values of cutting forces (<1 N).

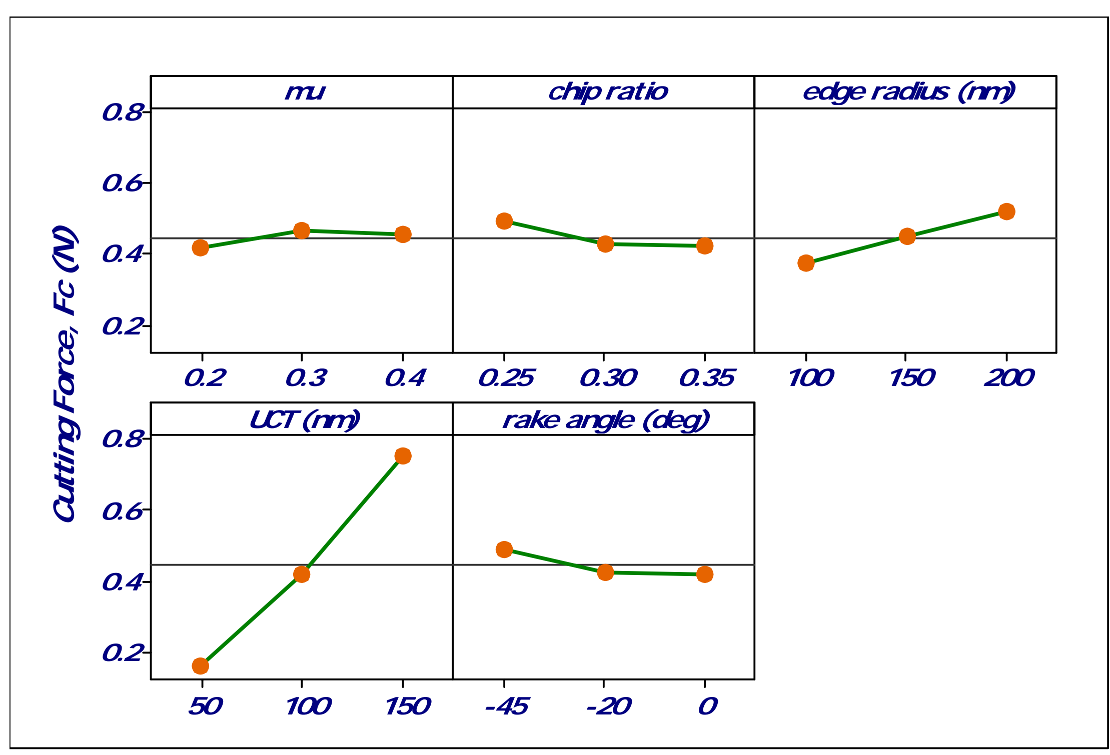

Figure 3.39 Main effects plot for cutting force (F_c)

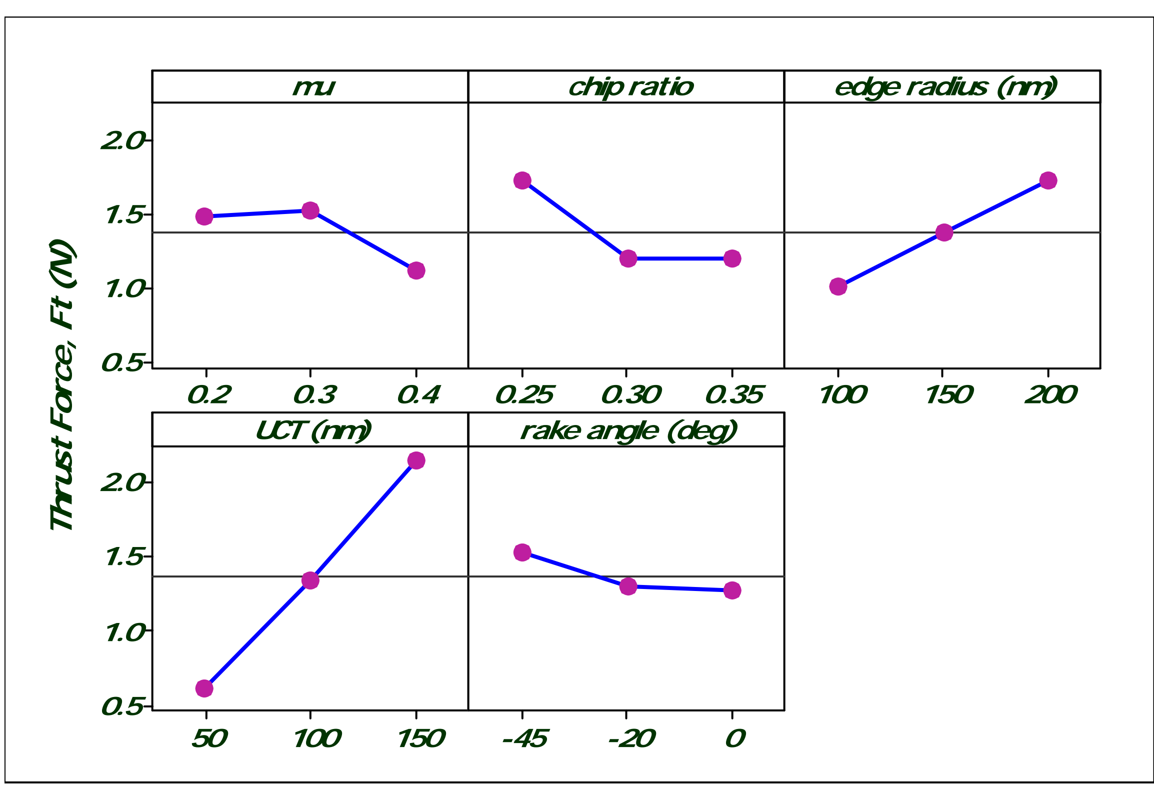

Figure 3.40 Main effects plot for thrust force (F_t)

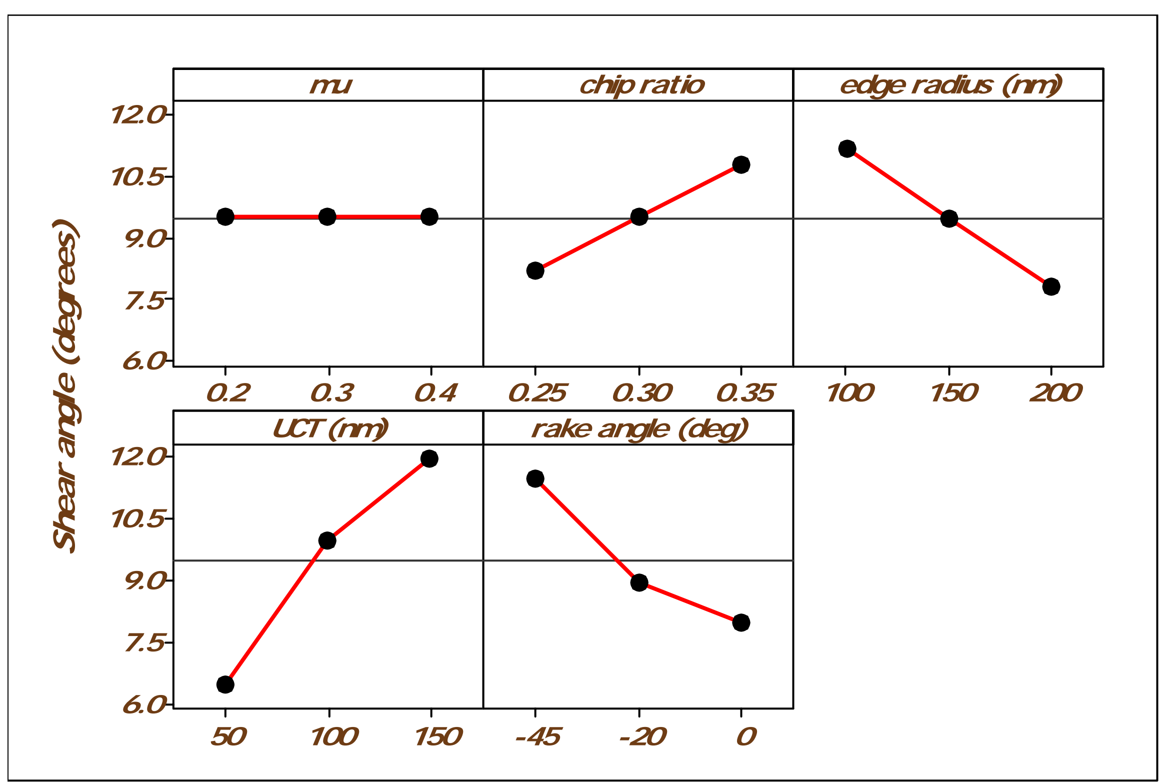

Figure 3.41 Main effects plot for shear angle (φ)

The thrust force is influenced strongly by the undeformed chip thickness and the tool edge radius as expected. The thrust force increases with decrease in coefficient of friction and is also influenced by the cutting ratio and rake angle to an extent. The shear angle is influenced strongly by rake angle, chip ratio, undeformed chip thickness and tool edge radius. However, the coefficient of friction does not seem to influence the shear angle. It should also be pointed out that the effect of interaction between two or more of the input factors on the response factors were minimal.

3.9.2 Determination of Transition Undeformed Chip Thickness

The transition undeformed chip thickness occurs when the stress intensity factor equals the fracture toughness of the material as stated earlier. The stress intensity factor

involves determining the normal stresses on the shear plane, which is in turn dependent on the forces. Therefore, the forces are first defined as fucntions of the undeformed chip thickness. The fit performed on the cutting and thrust forces revealed a cubic relationship between the forces and the undeformed chip thickness as given in (3.47) and as plotted in Figure 3.42.

$$\begin{aligned} F_c &= 0.004934t_0^3 + 0.01286t_0^2 + 0.3691t_0 + 0.8253 \\ F_t &= 0.07592t_0^3 - 0.2306t_0^2 + 0.6578t_0 + 2.074 \end{aligned} \tag{3.47}$$

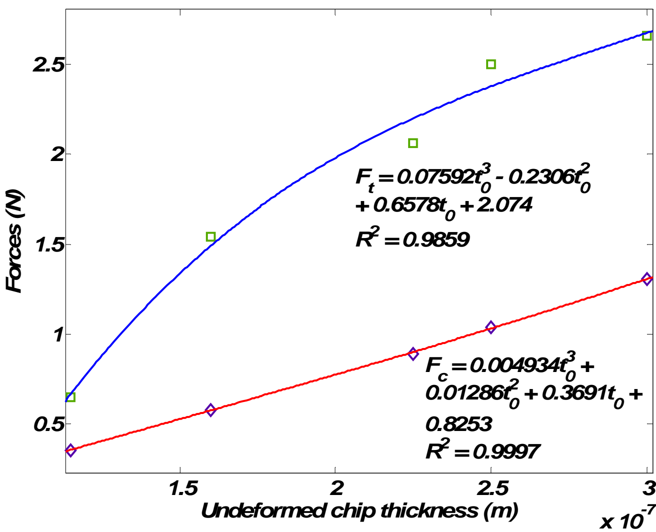

Figure 3.42 Cutting and thrust forces as fucntions of t_0

The force relations are then input into (3.8) to compute the normal stresses as a function of the undeformed chip thickness as shown in (3.48).

$$\sigma_s = \frac{\begin{bmatrix} \left(0.004934t_0^3 + 0.01286t_0^2 + 0.3691t_0 + 0.8253\right)\sin\varphi_e + \\ +\left(0.07592t_0^3 - 0.2306t_0^2 + 0.6578t_0 + 2.074_t\right)\cos\varphi_e \end{bmatrix}\sin\varphi_e}{t_0.w} \tag{3.48}$$

The normal stress is input into the stress intensity factor equation (3.25) where the geometric factor F is assumed as unity. The minimum flaw size *a* (Lawn and Evans, 1977) is proportional to the square of the ratio of the fracture toughness to the hardness of the material as in (3.49). The Knoop hardness value for silicon is given as H = 850 kg/mm^2 (Table 3-1). The flaw size was assumed to be a tenth of a nanometer which is reasonable as the wafer surface is well polished to remove all defects.

$$a = \beta \left(\frac{K_{Ic}}{H} \right)^2 \tag{3.49}$$

where β is a dimensionless scaling factor. The stress intensity factor is then compared with the fracture toughness K_{Ic} = 0.82 $MPa.m^{(1/2)}$ (Table 3-1) and the resulting equation is solved for t_0 which is the transition undeformed chip thickness.

$$K_{Ic} = K_I \Rightarrow 0.82e06 = \frac{\begin{bmatrix} \left(0.004934t_0^3 + 0.01286t_0^2 + 0.3691t_0 + 0.8253\right)\sin\varphi_e + \\ +\left(0.07592t_0^3 - 0.2306t_0^2 + 0.6578t_0 + 2.074_t\right)\cos\varphi_e \end{bmatrix} \sin\varphi_e}{t_0.w} \sqrt{\pi a} \tag{3.50}$$

The transition undeformed chip thickness solved using the above procedure was found to be **62.37 nm**. The value determined is very reasonable as can be seen from the quality of surfaces generated as shown in Figure 3.19.

For the sake of a reference, the transition undeformed chip thickness as formulated in (Blake and Scattergood, 1990) is used. The critical undeformed chip thickness is given by

$$t_c = \Psi \frac{E}{H}\left(\frac{K_{Ic}}{H}\right)^2 \tag{3.51}$$

where Ψ is a dimensionless constant dependent on the indentation geometry. Substituting values for material properties in (3.51) the values of transition undeformed chip thickness are computed as 33nm, 66 nm and 110 nm for Ψ values of 0.15, 0.3 and 0.5 respectively.

Effect of Cutting Velocity: The effect of cutting velocity on the transition undeformed chip thickness is studied. The change in velocity impacts the force functions and in turn affects the transition undeformed chip thickness. An increase in the velocity resulted in an increase in the value of the transition undeformed chip thickness as shown in Figure 3.43.

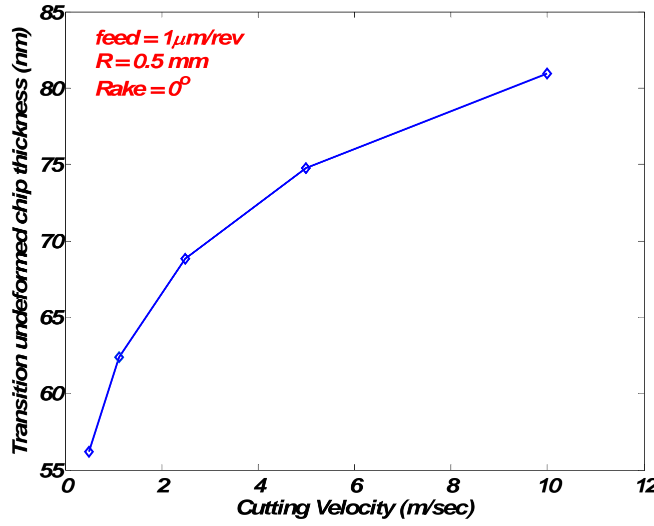

Figure 3.43 Effect of cutting velocity on transition undeformed chip thickness

This phenomenon could be attributed to thermal effects at higher velocities, as there may be a softening effect at the tool tip. It must be pointed out here that the plot was generated using the model and hence the effect of cutting velocity on the transition undeformed chip thickness must be experimentally verified.

Effect of Rake Angle: The effect of the nominal tool rake angle on the transition undeformed chip thickness was studied. The simulation was performed assuming different rake angle from 0° to -45°. The transition undeformed chip thickness values derived is shown in Table 3-9. The results show that the transition undeformed chip thickness increases with an increase in the tool rake angle. This trend is similar to the results reported in (Blake and Scattergood, 1990) for both germanium and silicon. The increase in the transition value is due to the fact that a more negative rake angle tool creates a state of compressive stress ahead of the tool and thus plays a vital role in suppressing the propagation of fracture. From this analysis, it can be concluded that a more negative rake angle tool is favorable for performing ductile regime machining at higher undeformed chip thickness values, which in-turn enhances material removal rates.

Table 3-9 Effect of nominal tool rake angle on transition undeformed chip thickness

Rake angle (deg)	Transition undeformed chip thickness (nm)
0	62.37
-15	66.51
-30	79.46
-45	135.1

The results obtained from the model for variation of transition undeformed chip thickness with changes in cutting velocity and nominal rake angle can be represented as a

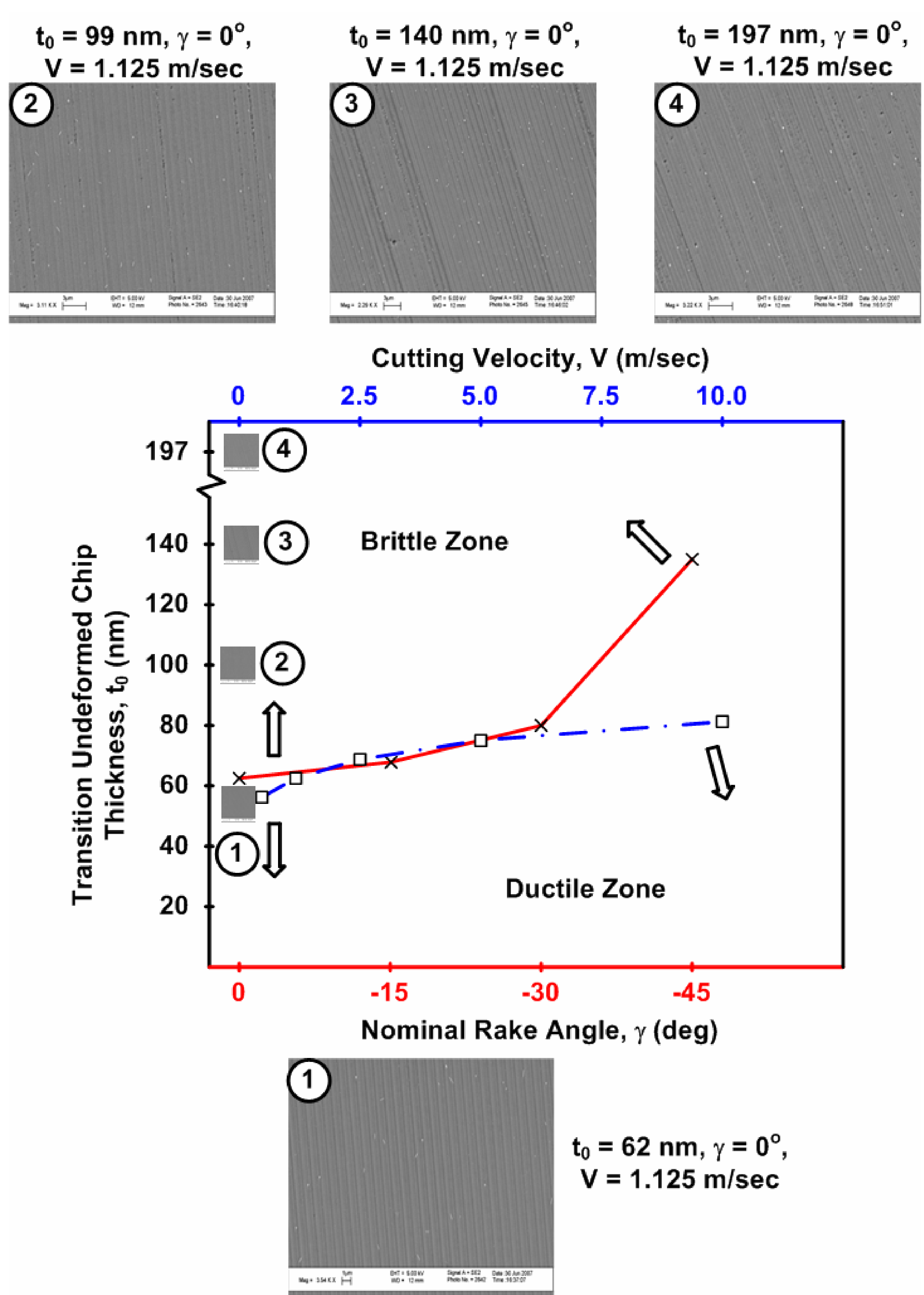

Figure 3.44 Transition undeformed chip thickness map for single crystal silicon

transition undeformed chip thickness map as shown in Figure 3.44. The transition undeformed chip thickness map can be interpreted as follows. The variation of the transition undeformed chip thickness with change in rake angle is shown as a solid (red) curve with x-marks as plot symbols. The area below this red curve represents machining in the ductile mode while the area above represents brittle mode machining. For a nominal rake angle of 0°, three sample machined surfaces are shown in Figure 3.44. The surface for t_0 = 62 nm which is below the red curve shows a ductile mode of material removal while the surfaces for t_0 = 99 nm, t_0 = 140 nm and t_0 = 197 nm which is above the red curve show cracks and pits on the machined surface indicating a brittle mode material removal. A similar interpretation can be performed for change in the transition undeformed chip thickness with a variation in cutting velocity which is represented by a dash-dot (blue) curve with squares as plot symbols. Again, the area below the blue curve represents material removal in the ductile mode while the area above the curve represents ductile mode material removal.

3.10 Summary

An analytical model for predicting the transition undeformed chip thickness in ductile regime machining has been developed. The process of ductile regime machining depends on a variety of factors including tool geometry, process conditions and workpiece material properties. The model had been developed keeping in mind the factors affecting the material response. The model has been validated by performing single point cutting experiments on single crystal silicon.

The process of cutting polycrystalline brittle materials is more challenging as compared to single crystal materials as the effect of microstructure including grain size, grain boundary and crystallographic orientation, affects the performance of the machining process. In the next chapter, a model is outlined to determine the variation of the cutting forces due to the effects of microstructure during cutting of polycrystalline brittle materials.

CHAPTER 4

Ultraprecision Machining of Polycrystalline Brittle Materials

Materials such as metals, alloys and ceramics are normally produced as polycrystalline aggregates, composed of many individual crystals (grains). These grains are usually microscopic in size and may vary from less than a micrometer to hundreds of micrometers. There are some prominent exceptions to this rule such as single crystal semiconductor materials, gems, certain fibers etc. Ductile materials such as steel, copper etc. are usually machined as polycrystalline aggregates, but brittle materials are machined more as single crystals. The applications in the semiconductor and optical industries require highly homogenous substrates for fabrication and hence single crystals are used. But there is a need for an ability to substitute single crystals with their polycrystalline counterparts, as there are technical difficulties in growing large-diameter single crystal materials. The polycrystalline materials are usually composed of differently oriented single crystals. If the orientations of the single crystals are random, a large volume of the polycrystalline material can be taken to be isotropic. But in reality, most polycrystalline materials have some orientation or alignment to their crystallites, which must be considered for accurate prediction of their behavior and characteristics. This is especially true for precision and ultraprecision machining where the process parameters are of the same order of magnitude as the grain size. This chapter deals with the microstructural issues involved in ultraprecision machining, especially single point diamond cutting of polycrystalline brittle materials.

There are two factors that need to be considered while analyzing the properties of aggregates: (i) the properties of the single crystal of the material, and (ii) the way in which the single crystals are assembled to form the polycrystalline aggregate. As stated earlier, the grains in polycrystalline aggregates may be randomly oriented in relation to a selected frame or they may cluster, to a lesser or greater degree, about some particular orientation or orientations. The materials which have grains clustering about some orientation are said to have a preferred orientation or texture. Therefore, when a material has texture, this means that the orientations of its grains are nonrandom (Cullity, 1978).

The process of machining brittle materials is difficult as pointed out in the previous chapter because their fracture toughness is low and hence they are easily prone to fracture. The problem is further compounded if the brittle materials are polycrystalline aggregates. The reason for the complexity arises due to the presence of different sizes of grains that the tool encounters, the grain boundaries and the changes in orientation of the different grains (Figure 4.1). All these factors, termed as microstructure effects, need to be considered in order to predict the quality of the surface that is produced during machining.

Yan et al. (2006) demonstrated machining of polycrystalline germanium (*p*-Ge) which is used for optical applications. From their experiments it was concluded that uniformly ductile-cut smooth surfaces could be produced across all crystals at very small undeformed chip thickness values. Bhattacharya et al. (2005) similarly demonstrated the possibility of machining polycrystalline brittle materials using ultraprecision single point cutting. The results provided evidence of high pressure phase transformation of the chips, which were amorphous with remnants of crystallites embedded in them.

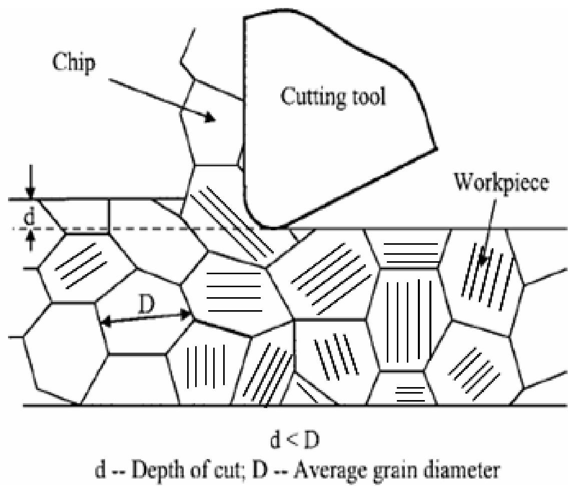

Figure 4.1 Microstructure effects in machining (adopted from Zhou et al. (2001))

The focus of this chapter is on the effect of microstructure on the cutting and thrust forces during the process of machining. The forces are affected by material properties (shear flow stress), tool geometry (rake angle, tool nose and edge radius), process conditions (cutting velocity, undeformed chip thickness, feed etc.), and microstructure effects (grain size, grain boundary, misorientation). The inherent process that aids machining through chip formation is plastic deformation that occurs along the shear plane. On an atomic level in micro-machining, plastic deformation occurs by motion of dislocations under the influence of a shear stress. The motion of dislocations is the reason for both the cutting and ploughing actions during micro-machining of brittle materials. It should be pointed out that the motion of dislocation is limited in a brittle material as compared to a ductile material.

This chapter introduces the concept of dislocation followed by details of a physics based model adopted to relate the flow stress of a material to its microstructural characteristics. The model is validated by two sets of experiments, one involving polycrystalline germanium and the other being polycrystalline silicon carbide. The

chapter is concluded by discussing results, drawing conclusions and laying a foundation for future directions in the area of machining brittle materials.

4.1 Defects in Crystals – Dislocations and Grain Boundaries

Crystals of both metals and ceramics by nature have defects in them. The defects in a crystal can be classified as point defects, line defects and surface defects. Of these defects, dislocations and grain boundaries are of interest in this project. Dislocation is a line defect and can be thought of as the boundary between slipped and unslipped regions of a slip plane which is created by the action of shear stress.

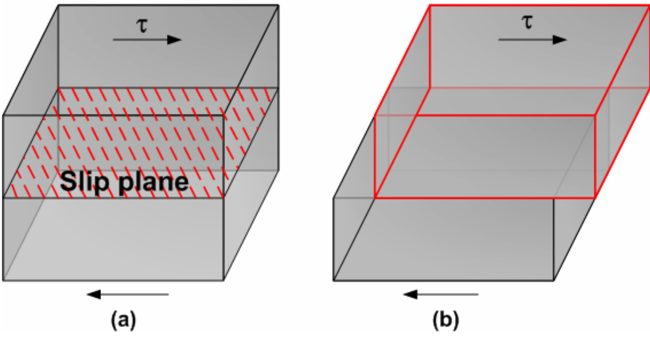

Figure 4.2 Movement of a solid cube along a slip plane (a) cube showing anticipated slip plane (b) slipped cube showing relative displacement (Hertzberg, 1976)

Figure 4.2 depicts the motion of a cube along a slip plane and the relative displacement of the cube. The applied shear stress (τ) based on an assumed sinusoidal variation in energy can be given by (4.1) where τ_m is the maximum theoretical shear strength of crystal, x is the distance atoms are moved and b is the distance between equilibrium positions.

$$\tau = \tau_m \sin\frac{2\pi x}{b} \tag{4.1}$$

It can be shown that the theoretical shear strength of the materials is proportional to $G/2\pi$ where G is the shear modulus of the material. In reality, the maximum theoretical shear strength is more in the range of *G/30*.

Dislocations can be further classified as edge dislocations and screw dislocations. Edge dislocation can be thought of as the border of an extra plane of atoms as shown in Figure 4.3a. Screw dislocations can be explained by assuming that a perfect crystal is cut as shown in Figure 4.3b. The crystal is then displaced parallel to the cut and finally reconnected into the configuration as shown.

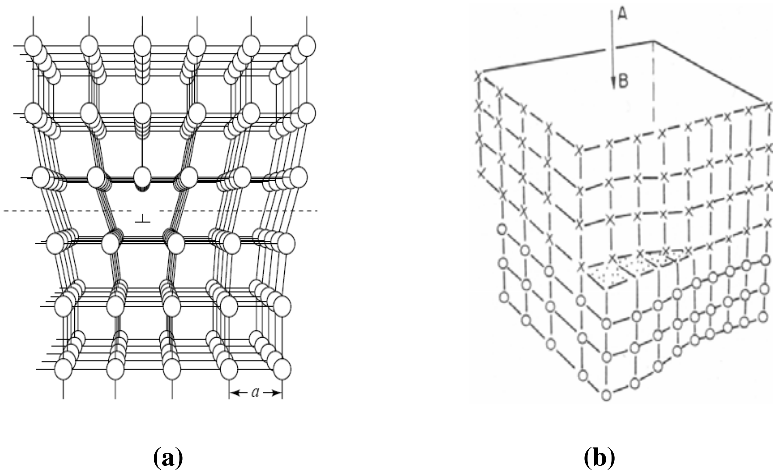

(a) **(b)**

Figure 4.3 Schematic of edge (left) and screw (right) dislocations

Plastic deformation occurs through mechanism of slip, which is the motion of dislocations (Figure 4.4) on a slip plane in a particular slip direction. The combination of slip plane and slip direction is commonly referred to as slip system. Depending on the atomic arrangement, the number of possible slip systems varies from *3* for hexagonal

close-packed (*hcp*) crystals to *12* for face-centered cubic (*fcc*) crystals and as much as *48* for body centered cubic (*bcc*) crystals.

The presence of dislocations reduces the shear stress required to cause slip. On the other hand, the motion of dislocations can be impeded by the presence of grain boundaries and impurities or due to dislocations becoming entangled and interfering with each other. The impediment to the motion of dislocations causes an increase in the shear stress required for slip. This increase in the overall strength of the material is termed as work or strain hardening.

An important characteristic associated with dislocations is the distance and direction by which atoms on the upper side of the slip plane move relative to the atoms on the lower side. This distance is termed the Burgers vector (*b*) of the dislocation.

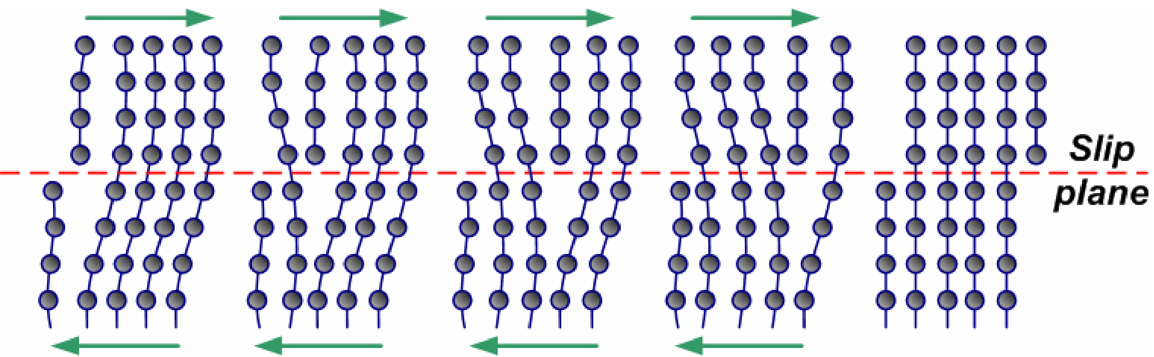

Figure 4.4 Movement of edge dislocation across the crystal lattice under shear stress (Kalpakjian and Schmid, 2003)

Grain boundaries are another class of surface defects and are formed due to the change in orientation of lattice planes by large angles. During the process of grain growth or nucleation individual grains eventually impinge on each other and form surfaces separating them known as grain boundaries (Figure 4.5). The grain boundaries affect the

motion of dislocations and hence have an impact on the strength of the material. They can be low angle, medium angle and high angle grain boundaries.

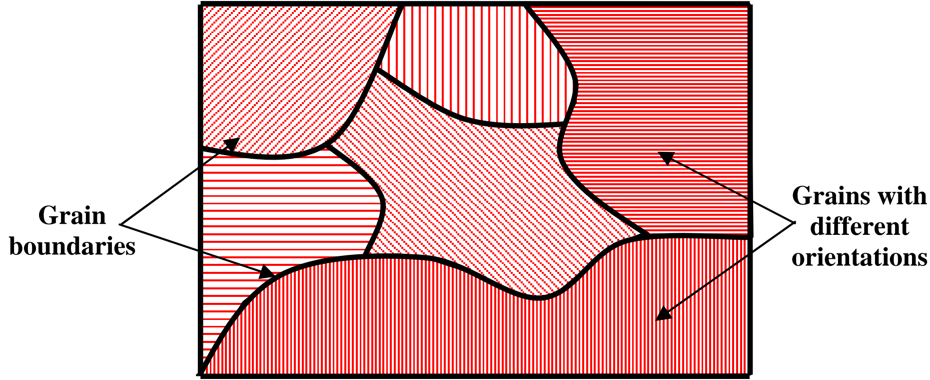

Figure 4.5 Grains and grain boundaries

4.2 Modeling Microstructure Effects

In order to model the microstructure effects in machining, the effects of grain size, grain boundaries, and crystallographic orientation must be considered, since the machining parameters, such as the depth of cut are of the same order as the grain size, as depicted in Figure 4.1. As the tool moves across the grains, it encounters different crystallographic orientations, different grain sizes, and grain boundaries. All of these factors influence the output process parameters such as forces and surface finish.

The effects of grain size, grain boundaries, and crystallographic orientation are captured by a model proposed by Hughes et al. (2000). This model determines the microstructural effects on flow stress based on the analysis of dislocation density. The dislocation boundaries are classified into geometrically necessary boundaries (*GNB*) and incidental dislocation boundaries (*IDB*). The *GNB*s separate regions that deform by different slip system combinations, strain amplitudes, and strain. The ordinary cell

boundaries are *IDB*s that form by trapping of glide dislocations. To develop the variation of flow stress with change in misorientation and grain size, the contribution of dislocations is considered herein. The total dislocation density (ρ_t) can be expressed as:

$$\rho_t = \rho_o + \rho_b \tag{4.2}$$

where ρ_o is the dislocation density in the volume between boundaries and ρ_b is the dislocation density per unit volume. The total dislocation density can also be expressed in terms of misorientation and the grain boundary spacing as:

$$\rho_t = \frac{k\theta_{av}}{D_{avg}b} \tag{4.3}$$

where k is a constant, θ_{av} is the average misorientation, b is the Burgers vector, and D_{avg} is the average grain boundary spacing. The misorientation can be found by analysis of local crystallography using Kikuchi patterns (Liu Q., 1994). The contribution of IDBs (σ_{IDB}) to the flow stress can be expressed as:

$$\sigma_{IDB} = M\alpha Gb\sqrt{\rho_t} = M\alpha Gb\sqrt{\frac{k\theta_{av}}{D_{avg}b}} \tag{4.4}$$

where α and k are constants, M is the Taylor factor based on crystal orientation, and G is the shear modulus.

The overall flow stress taking into account both *IDB*s and *GNB*s can be given by the following equation (Hughes and Hansen, 2000):

$$\sigma = \sigma_o(\varepsilon, \dot{\varepsilon}, T) + M\alpha Gb\sqrt{\frac{k\theta_{av}}{D_{avg}b}} + K_{HP}(\varepsilon, \dot{\varepsilon}, T)D^{-1/2} \tag{4.5}$$

where D is the grain size, K_{HP} is the Hall-Petch coefficient and σ_o is substituted by (3.10) which describes flow stress as a function of strain, strain-rate, and temperature. The last part of the equation represents the effect of grain size on the relative hardening of the material as given by Hall-Petch (Hall, 1951 & Petch, 1953). In a polycrystalline aggregate the grain size distribution is never uniform (Figure 4.6) and is best described by a lognormal distribution such as:

$$f(D) = \frac{1}{\sqrt{2\pi}\sigma D}\exp\left(-\frac{1}{2}\left(\frac{\ln(D)-\mu}{\sigma}\right)^2\right) \tag{4.6}$$

where μ and σ are the mean and standard deviation of the variable's logarithm.

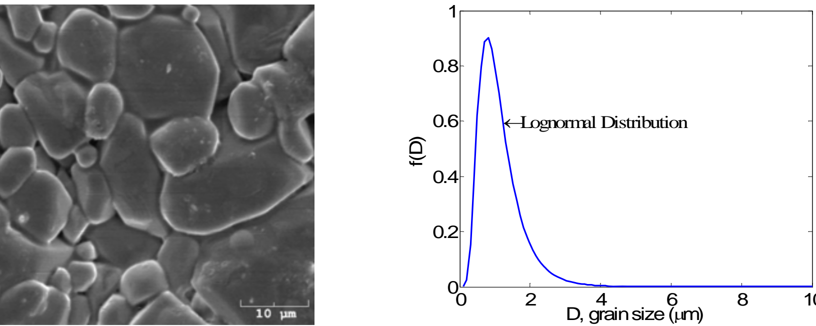

Figure 4.6 Sample grain structure of Alumina (Al_2O_3) & lognormal distribution for grain size

The flow stress obtained in (4.5) can be related to shear flow stress (plane strain condition (Oxley, 1989)) as in (4.7).

$$k = \frac{\sigma}{\sqrt{3}} \tag{4.7}$$

The value k can then be utilized in (3.4) and (3.5) to determine the forces. Thus, the effects of microstructure, including grain size, grain boundaries, and crystal orientation have been captured and modeled to reflect on cutting and thrust forces.

In order to validate the model, two experimental cases were analyzed. The first involved data obtained from Yan et al. (2004) for machining polycrystalline germanium (*p*-Ge). The second case involved performing single point diamond turning on polycrystalline silicon carbide (*p*-SiC).

4.3 Ultraprecision Machining of Polycrystalline Germanium

This section describes the application of the model given above to machining polycrystalline germanium. The experimental data is taken from Yan et al. (2004) and the model is validated for the given process conditions. A sensitivity analysis is performed to determine the effect of input process parameters on the shear angle and the forces in the cutting and thrust directions.

4.3.1 Experimental Procedure

The experimental data used in this work was obtained from Yan et al. (2004). The experiments were performed on polycrystalline germanium using an ultraprecision lathe, the details of which are given in Table 4-1.

Table 4-1 Machining conditions for polycrystalline germanium (Yan et al., 2004)

Basic operation	Face turning
Workpiece	Polycrystalline germanium (*p*-Ge)
Cutting tool	SCD (straight nosed) tool
Rake angle	-20°
Relief angle	6°, 26°, 51°
Cutting speed	5 m/sec
Cutting edge angle (κ)	$0.15 – 1.45^o$
Feed	7 – 37.5 μm/rev

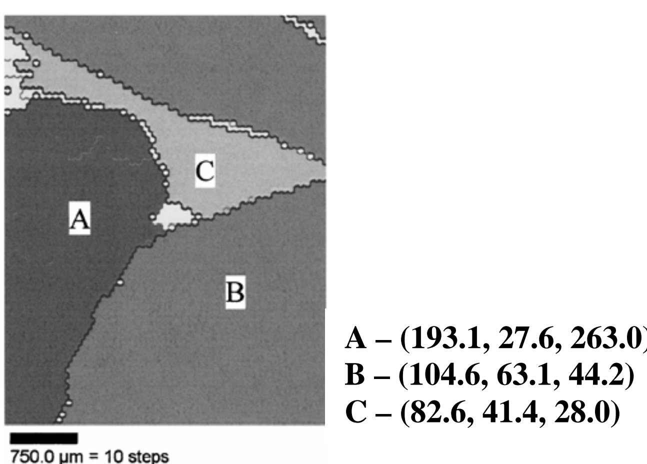

Figure 4.7 Grain map of *p*-Ge obtained using Orientation Imaging Microscopy (OIM) and corresponding Euler angles for the three grains (reproduced from Yan et al., 2004)

The microstructure of *p*-Ge, for the purposes of this experiment, consisted of three grains (*A, B, C*) with an approximate size of 1-3 mm. Since the grains are larger than typical grain sizes in polycrystalline materials, each individual grain may be considered as a single crystal. It should be pointed out here that the experimental data for grains *A*

and *B* were used for the purposes of comparison, as the data for grain C was not available in Yan et al. (2004). The orientations of the three grains along with their grain boundaries are captured using an orientation-imaging microscopic system and are shown in Figure 4.7. The machining model for the experimental set-up is shown in Figure 4.8. The relationship between undeformed chip thickness (h), feed (f) and cutting edge angle (κ) is given by the following equation.

$$h = f \cdot \sin \kappa \tag{4.8}$$

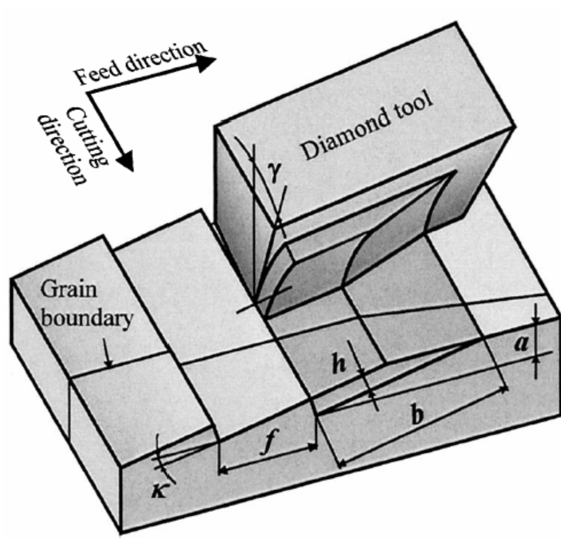

Figure 4.8 Machining model: a – depth of cut; h – undeformed chip thickness; f – feed; b – width of cut; κ – cutting edge angle (reproduced from Yan et al., 2004)

4.3.2 Experimental Force Measurements

The measured forces extracted from Yan et al. (2004) in the principal cutting and thrust directions for the given conditions are shown in Figure 4.9. The three undeformed chip thicknesses considered were 42, 131, and 693 nm. From the figure, the thrust force for *Grain A* decreases with an increase in undeformed chip thickness, which is not

expected. The cutting force for *Grain A* and the cutting and thrust forces for *Grain B* increase for an increase in undeformed chip thickness of up to around 131 nm, which is expected. But there is a fall off beyond that for an increase in undeformed chip thickness to 693 nm. The reason for the drop off is at 693 nm the surface produced is through brittle fracture rather than by ductile removal. The energy associated with brittle fracture is lower than that involved in ductile deformation and hence lower forces are observed.

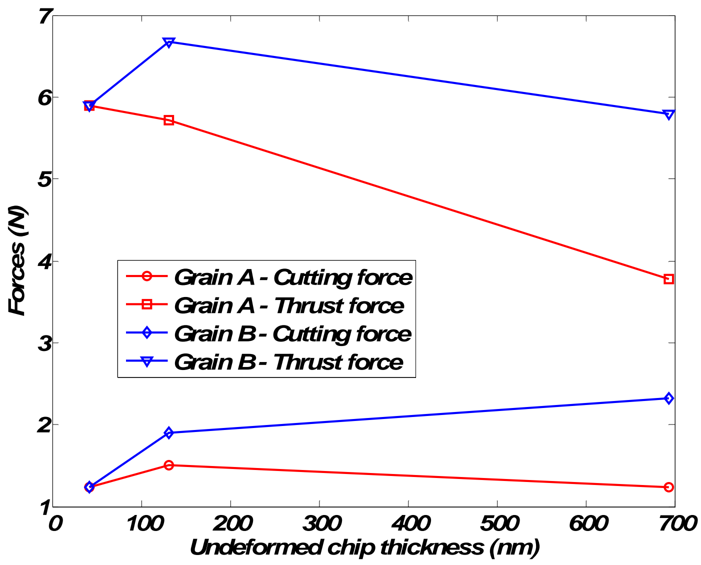

Figure 4.9 Experimental force data extracted from Yan et al., (2004)

4.3.3 Prediction of Forces

The prediction of forces requires the use of the force model developed in chapter 3. The cutting and thrust forces are computed by first determining the flow stress. The flow stress is obtained from the Johnson-Cook material constitutive model along with the effects of microstructure which requires the evaluation of misorientation. The forces are then compared to experimental values obtained from Yan et al., (2004). The force variations between two adjacent grains are also compared with the experimental results.

A sensitivity analysis is also performed to study the variation in cutting force, thrust force and shear angle while changing input process parameters such as rake angle, chip ratio, undeformed chip thickness etc.

4.3.3.1 Material Constitutive Model

The Johnson-Cook material model described in chapter 3 is used for germanium. As mentioned earlier, the constants (*A, B, C, m, n*) for the model were not available, and hence an optimization procedure described in chapter 3 was employed to determine the constants. The applicability of this model for a brittle material such as germanium is based on experimental results from Yan et al. (2004) that show appreciable material flow during ductile regime machining. This can be verified from the continuous chip formation and the texture of the surface generated. Moreover, it is also assumed that the strain, strain rate, and temperature affect the chip formation process during machining of polycrystalline germanium.

The optimization approach involved utilizing the simplex (Nelder-Mead) method, which required an initial guess for the constants *A, B, C, m,* and *n*. The results converged to a local optimum, but not necessarily a global optimum. Therefore, the results were a direct function of either the initial values or the constraints. The results of the optimization procedure, including three sets of optimum values, are given in Table 4-2. The third set of optimum values was used in this work.

Table 4-2 Results of optimization process for determining material constants in JC model

A(MPa)	B(MPa)	n	C	m
1441.63	611.44	0.567	0.0646	1.555
767.8	856.2	0.702	0.0828	4.101

3305.57	89.07	0.0621	0.03167	0.00038

4.3.3.2 Misorientation

The grain map studied by Yan et al. (2004) is schematically represented as shown in Figure 4.10. The misorientation in the different grains results in the formation of grain boundaries. The cutting direction is such that the tool passes from *Grain A* to *Grain B*.

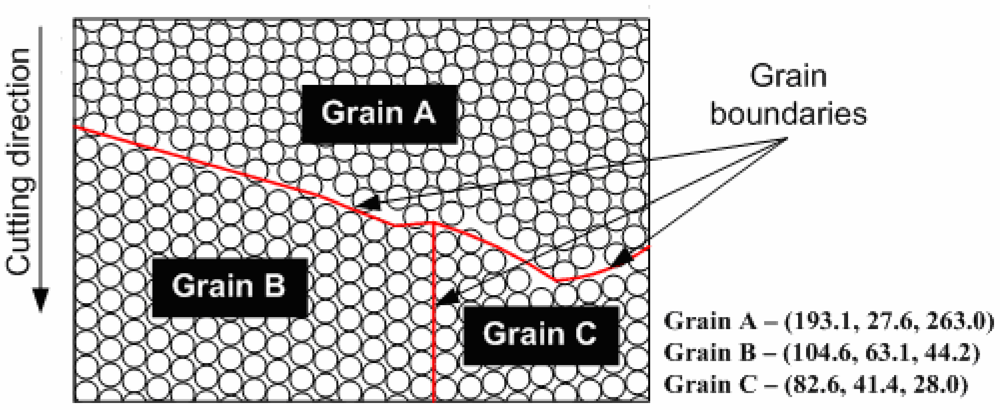

Figure 4.10 Schematic of the grain map in polycrystalline germanium

The misorientation, which is the relative rotation between the orientations of two neighboring lattices, is computed based on Euler angles ($\varphi_1, \Phi, \varphi_2$) provided in Yan et al. (2004) for the various grains and as given in Figure 4.10. The rotations to align the orientation of a grain to a reference axis (say, sample axis) can be given by the rotation matrix *M* in (4.10). The rotation matrices for grains *A* and *B* are obtained from *M* using the given Euler angles as g_A and g_B (Figure 4.11) respectively. The rotation matrix M is obtained by performing three individual rotations given in (4.9).

$$M = m_1 m_2 m_3$$

$$m_1 = \begin{pmatrix} \cos\varphi_1 & \sin\varphi_1 & 0 \\ -\sin\varphi_1 & \cos\varphi_1 & 0 \\ 0 & 0 & 1 \end{pmatrix}$$

$$m_2 = \begin{pmatrix} 1 & 0 & 0 \\ 0 & \cos\Phi & \sin\Phi \\ 0 & -\sin\Phi & \cos\Phi \end{pmatrix} \quad (4.9)$$

$$m_3 = \begin{pmatrix} \cos\varphi_2 & \sin\varphi_2 & 0 \\ -\sin\varphi_2 & \cos\varphi_2 & 0 \\ 0 & 0 & 1 \end{pmatrix}$$

$$M = \begin{pmatrix} \cos\varphi_1\cos\varphi_2 - \sin\varphi_1\sin\varphi_2\cos\Phi & \sin\varphi_1\cos\varphi_2 + \cos\varphi_1\sin\varphi_2\cos\Phi & \sin\varphi_2\sin\Phi \\ -\cos\varphi_1\sin\varphi_2 - \sin\varphi_1\cos\varphi_2\cos\Phi & -\sin\varphi_1\sin\varphi_2 + \cos\varphi_1\cos\varphi_2\cos\Phi & \cos\varphi_2\sin\Phi \\ \sin\varphi_1\sin\Phi & -\cos\varphi_1\sin\Phi & \cos\Phi \end{pmatrix} \quad (4.10)$$

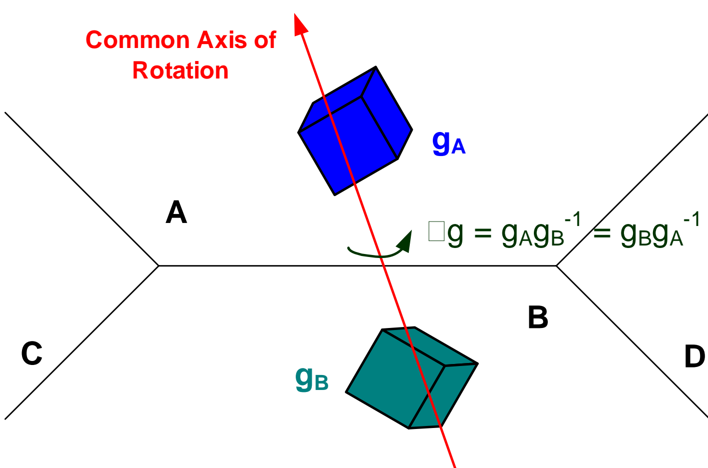

Figure 4.11 Schematic of misorientation between two grains

The misorientation between grains *A* and *B* is given by:

$$\Delta g = g_A g_B^{-1} \quad (4.11)$$

The angle of misorientation (θ) can be obtained from the following equation:

$$\theta = \min \left| \cos^{-1} \left\{ \frac{(tr(T_i \Delta g)) - 1}{2} \right\} \right| \tag{4.12}$$

where tr is the trace of Δg and T_i is the symmetry operator and i = 1..24. The trace (tr) of a matrix is simply the sum of its diagonal terms. The symmetry operator T_i can be defined as follows (Randle, 1993):

Table 4-3 Matrices representing the 24 symmetry operations for the cubic system

$T_i - 1{:}6$	$\begin{matrix} 1 & 0 & 0 \\ 0 & 1 & 0 \\ 0 & 0 & 1 \end{matrix}$	$\begin{matrix} \bar{1} & 0 & 0 \\ 0 & \bar{1} & 0 \\ 0 & 0 & \bar{1} \end{matrix}$	$\begin{matrix} 0 & 0 & \bar{1} \\ 0 & 1 & 0 \\ 1 & 0 & 0 \end{matrix}$	$\begin{matrix} \bar{1} & 0 & 0 \\ 0 & 1 & 0 \\ 0 & 0 & \bar{1} \end{matrix}$	$\begin{matrix} 0 & 0 & 1 \\ 0 & 1 & 0 \\ \bar{1} & 0 & 0 \end{matrix}$	$\begin{matrix} 1 & 0 & 0 \\ 0 & 0 & \bar{1} \\ 0 & 1 & 0 \end{matrix}$
$T_i - 7{:}12$	$\begin{matrix} 1 & 0 & 0 \\ 0 & \bar{1} & 0 \\ 0 & 0 & \bar{1} \end{matrix}$	$\begin{matrix} 1 & 0 & 0 \\ 0 & 0 & 1 \\ 0 & \bar{1} & 0 \end{matrix}$	$\begin{matrix} 0 & \bar{1} & 0 \\ 1 & 0 & 0 \\ 0 & 0 & 1 \end{matrix}$	$\begin{matrix} \bar{1} & 0 & 0 \\ 0 & \bar{1} & 0 \\ 0 & 0 & 1 \end{matrix}$	$\begin{matrix} 0 & 1 & 0 \\ \bar{1} & 0 & 0 \\ 0 & 0 & 1 \end{matrix}$	$\begin{matrix} 0 & 0 & 1 \\ 1 & 0 & 0 \\ 0 & 1 & 0 \end{matrix}$
$T_i - 13{:}18$	$\begin{matrix} 0 & 1 & 0 \\ 0 & 0 & 1 \\ 1 & 0 & 0 \end{matrix}$	$\begin{matrix} 0 & 0 & \bar{1} \\ \bar{1} & 0 & 0 \\ 0 & 1 & 0 \end{matrix}$	$\begin{matrix} 0 & \bar{1} & 0 \\ 0 & 0 & 1 \\ \bar{1} & 0 & 0 \end{matrix}$	$\begin{matrix} 0 & 1 & 0 \\ 0 & 0 & \bar{1} \\ \bar{1} & 0 & 0 \end{matrix}$	$\begin{matrix} 0 & 0 & \bar{1} \\ 1 & 0 & 0 \\ 0 & \bar{1} & 0 \end{matrix}$	$\begin{matrix} 0 & 0 & 1 \\ \bar{1} & 0 & 0 \\ 0 & \bar{1} & 0 \end{matrix}$
$T_i - 19{:}24$	$\begin{matrix} 0 & \bar{1} & 0 \\ 0 & 0 & \bar{1} \\ 1 & 0 & 0 \end{matrix}$	$\begin{matrix} 0 & 1 & 0 \\ 1 & 0 & 0 \\ 0 & 0 & \bar{1} \end{matrix}$	$\begin{matrix} \bar{1} & 0 & 0 \\ 0 & 0 & 1 \\ 0 & 1 & 0 \end{matrix}$	$\begin{matrix} 0 & 0 & 1 \\ 0 & \bar{1} & 0 \\ 1 & 0 & 0 \end{matrix}$	$\begin{matrix} 0 & \bar{1} & 0 \\ \bar{1} & 0 & 0 \\ 0 & 0 & \bar{1} \end{matrix}$	$\begin{matrix} \bar{1} & 0 & 0 \\ 0 & 0 & \bar{1} \\ 0 & \bar{1} & 0 \end{matrix}$

The misorientation angle computed for all 24 cases is shown in Table 4-4. The minimum angle is chosen as the misorientation angle and in the case of *p*-Ge the misorientation angle between grains *A* and *B* was 29.61°.

Table 4-4 Misorientation angles for all 24 symmetry operations for the cubic system

T_i – 1:6	92.8747	161.7773	152.0444	139.3250	99.8213	157.7542
T_i – 7:12	130.7944	77.1693	163.0383	122.5533	68.3914	171.9841
T_i – 13:18	103.4769	156.5837	121.8150	113.2006	164.0581	***29.6097***
T_i – 19:24	147.7595	174.4250	169.2047	101.2774	114.6135	108.3125

4.3.3.3 Shear Strain and Strain-rate

The shear strain and strain-rate are computed based on the model by Oxley (1989) and Manjunathaiah and Endres (2000). A comparison of the shear strain between the two models is shown in Figure 4.12a. The shear strain predicted between the two models is of the same order of magnitude and trend. But Oxley’s model predicts a higher value for the shear strain. The comparison of shear strain-rate between the two models is shown in Figure 4.12b and from the plot it is clear that the values are of the same order of magnitude and trend and Oxley’s model predicts a higher value for shear strain-rate. For the purpose of force prediction for machining *p*-Ge, the model proposed by Oxley is used.

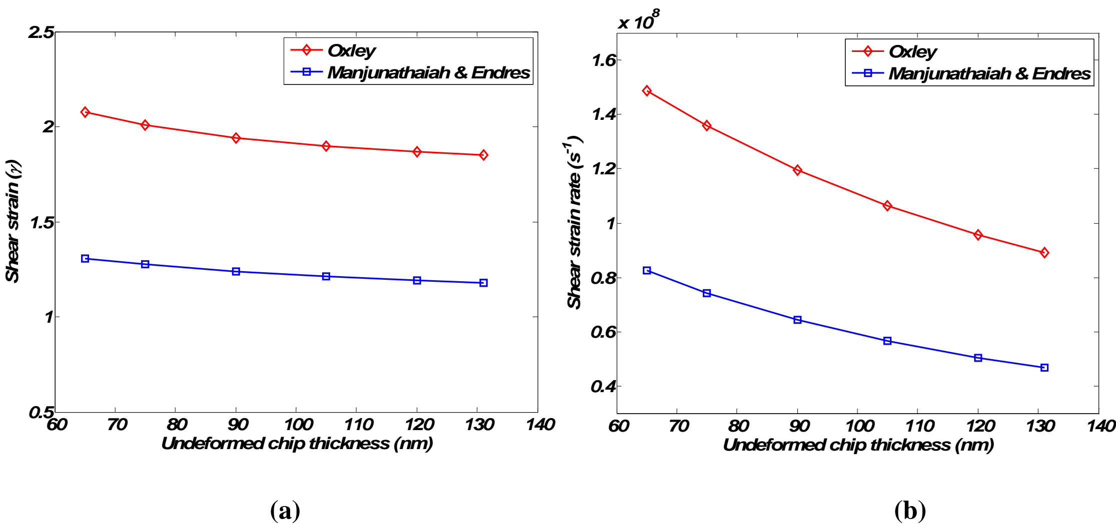

Figure 4.12 Comparison of (a) shear strain and (b) strain-rate for a nominal rake angle γ = -20° and cutting velocity V = 5 m/sec

4.3.3.4 Force Prediction

The procedure for predicting the forces is the same as detailed in chapter 3. The shear strain and strain-rate discussed previously are used in the Johnson-Cook's equation to determine the flow stress. The constants for the Johnson-Cook's equation are given in Table 4-2. The equivalent rake angle is computed for an undeformed chip thickness and tool edge radius angle as discussed in chapter 3. The shear angle is computed knowing the equivalent rake angle and chip ratio. The friction coefficient is initially assumed to be 0.1 and its sensitivity on forces is discussed in the next section. The effects of microstructure were not considered in this case. It should also be pointed out here that the effect of temperature was not modeled separately.

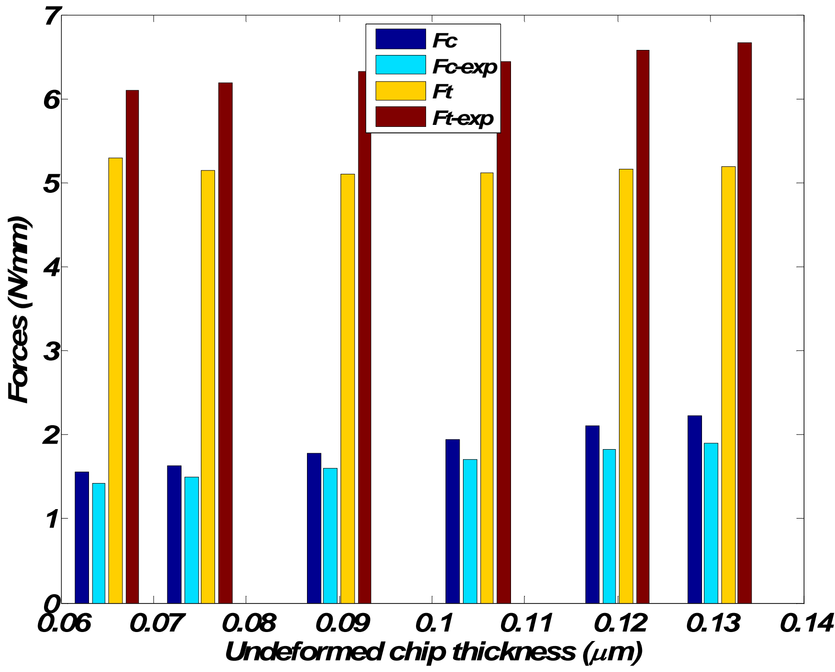

Figure 4.13 Comparison of predicted forces with corresponding experimental values

The predicted forces (*Grain B*) for a range of undeformed chip thickness from 65 – 131 nm are shown in Figure 4.13. The forces have been computed using the Johnson-

Cook's constitutive model values (Table 4-2) for flow stress which include the effects of strain and strain-rate. From the figure, it can be seen that the cutting forces are predicted reasonably well while the thrust forces are under predicted to about 22% maximum error although the trend is well captured. The reasons for this deviation could be associated with the determination of constants in the JC model, accurate determination of the tool edge radius, process conditions such as friction, and the effects of microstructure.

In order to capture microstructure effects, including the grain boundary and misorientation, (4.5) was employed. This equation for flow stress includes effects of grain size, grain boundary, strain, strain rate, and temperature. As mentioned before, the grain size for *p*-Ge is of the order of 1-3 mm and hence each individual grain can be considered as a single crystal with the given orientation. Therefore, the first two terms in the flow stress equation are considered for the case of *p*-Ge which includes the effects of strain, strain rate, and crystallographic orientation. The constants used in (4.5) are as shown in Table 4-5.

Table 4-5 Constants used in (4.5)

Constants	Value	Reference
M	3.0	Taylor factor – The value varies from 1.732 – 3.67 (Conrad, 2004)
k	4	constant depending on geometry of boundary (Liu Q. et al., 1998)
α	0.5	constant – ranging from 0.2 – 0.5 (Conrad, 2004)
θ	29.61^{o}	misorientation angle – computed using (4.12)
b	3.99e-10 m	burgers vector for Ge (Frost and Ashby, 1982)
D_{avg}	1 mm	grain boundary spacing – assumed equal to grain size
G	52–67 GPa	shear modulus, Frost and Ashby, 1982

Figure 4.14 shows a comparison between cutting and thrust forces for grains *A* and *B* as a ratio for various undeformed chip thickness values. The bars represent a ratio

of the forces for grain *B* to grain *A*. The forces were obtained assuming that the tool enters the material through *grain A* and then moves over the boundary to *grain B*. The forces for *grain A* were obtained assuming the misorientation angle $\theta = 0^{o}$ and the forces for grain *B* was obtained using $\theta = 29.61^{o}$ which is the relative misorientation between grains *A* and *B*. The plot shows that the ratios of experimental forces match reasonably well with the predicted forces in both the cutting and thrust directions. It should however be noted that in Figure 4.14, the comparison is of the ratios of the forces between grain *A* and grain *B*. The exact magnitude of experimental forces may still be different from the predicted values as can be seen in Figure 4.13.

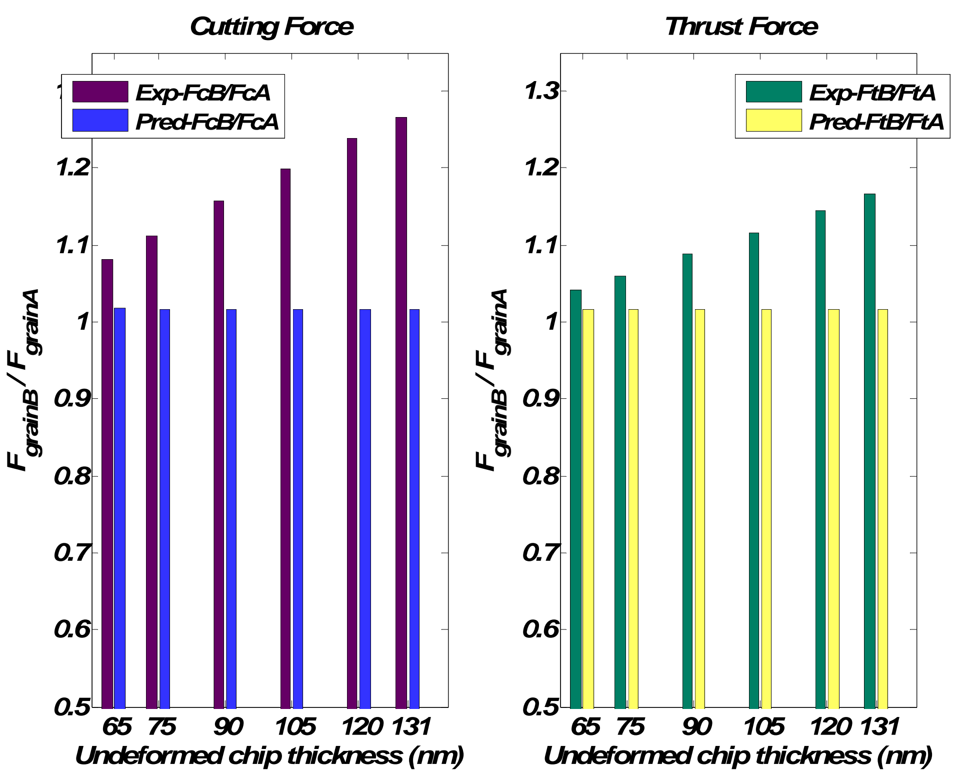

Figure 4.14 Force comparison for grains *A* and *B*

4.3.3.5 Sensitivity Analysis

In order to further investigate the reasons for deviation of the predicted force values from the experimental results, a sensitivity analysis is performed to evaluate the impact of process parameters on the predicted forces. A three-level, six factor fractional factorial design (3_{IV}^{6-2} = 81 runs) is adopted to determine the variation of output parameters to changes in the input data set. The design is chosen such that all the main effects are not aliased with other higher order interactions. The design is summarized in Table 4-6.

Table 4-6 Design of experiments for sensitivity analysis

Factor	Low	Medium	High
Friction coefficient (μ)	0.1	0.2	0.3
Chip ratio (r_c)	0.3	0.4	0.5
Nominal rake angle (α – degrees)	0	-20	-45
Tool edge radius (r – nm)	50	75	100
misorientation angle (θ – degrees)	10	20	30
Undeformed chip thickness (t_0 – nm)	50	100	150
Responses – Cutting force (F_c), Thrust Force (F_t), Shear angle (φ)			

The main effects plots for the cutting force, thrust force, and shear angle are shown in Figure 4.15, Figure 4.16, and Figure 4.17 respectively. The results show that the cutting force is strongly influenced by the tool edge radius, undeformed chip thickness, and friction coefficient. The rake angle also affects the cutting, but the variation is more pronounced for highly negative rake angles. The effect of chip ratio is small and misorientation angle does not affect the cutting force as can be seen from the approximately horizontal lines in Figure 4.15.

The thrust force is strongly influenced by the edge radius, as expected, and also by the undeformed chip thickness. As in the case of the cutting force, the thrust force is

also influenced by highly negative rake angles. The influence of friction coefficient on thrust force is much less compared to cutting force as can be seen in Figure 4.16. The chip ratio does influence the thrust forces to a large extent, as opposed to its influence on the cutting force.

The shear angle is strongly influenced by the chip ratio and the nominal rake angle as suggested by (3.2). In addition, the shear angle is also influenced by the tool edge radius and the undeformed chip thickness. The friction coefficient and the misorientation angle have no influence on the shear angle as shown in Figure 4.17. It should also be pointed out that the effect of interaction between two or more of the input factors on the response factors were minimal.

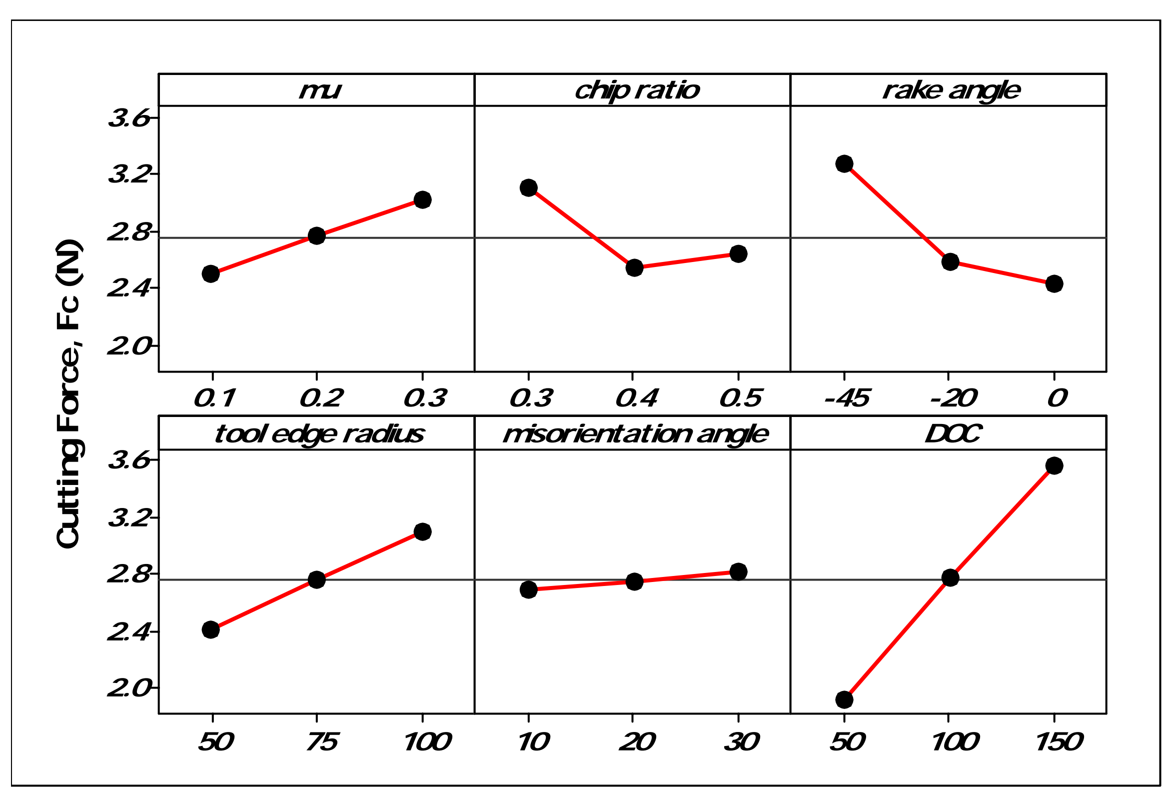

Figure 4.15 Main effects plot for cutting force (F_c)

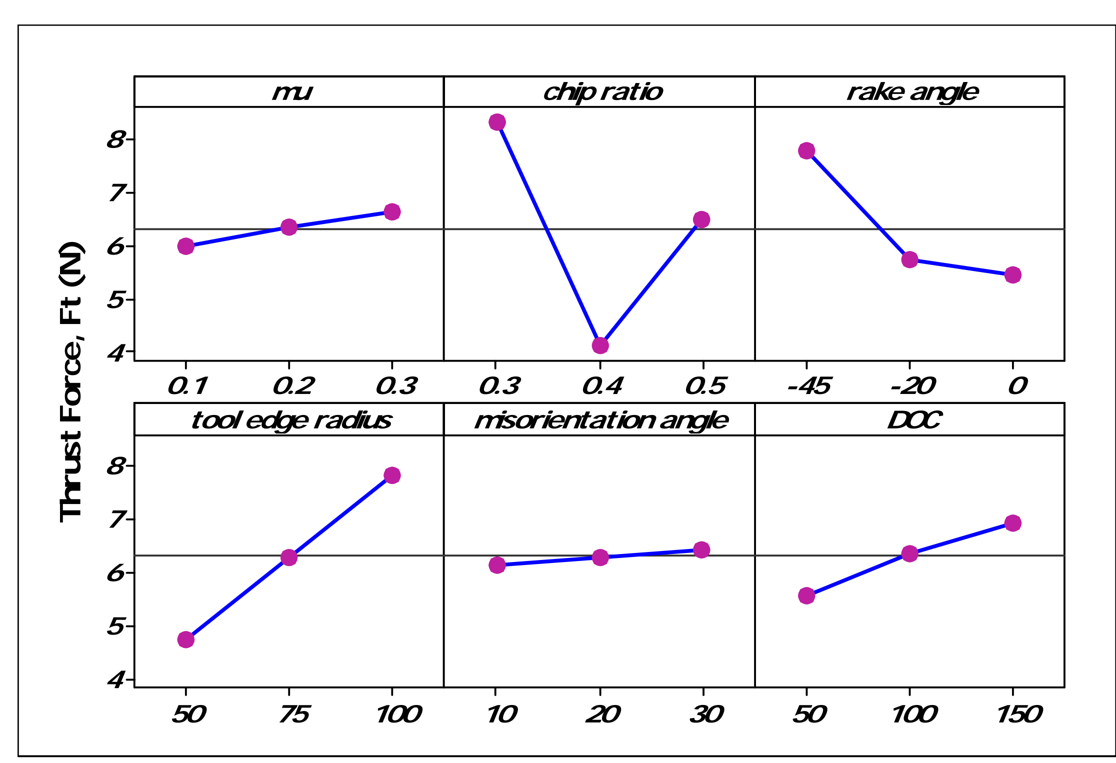

Figure 4.16 Main effects plot for thrust force (F_t)

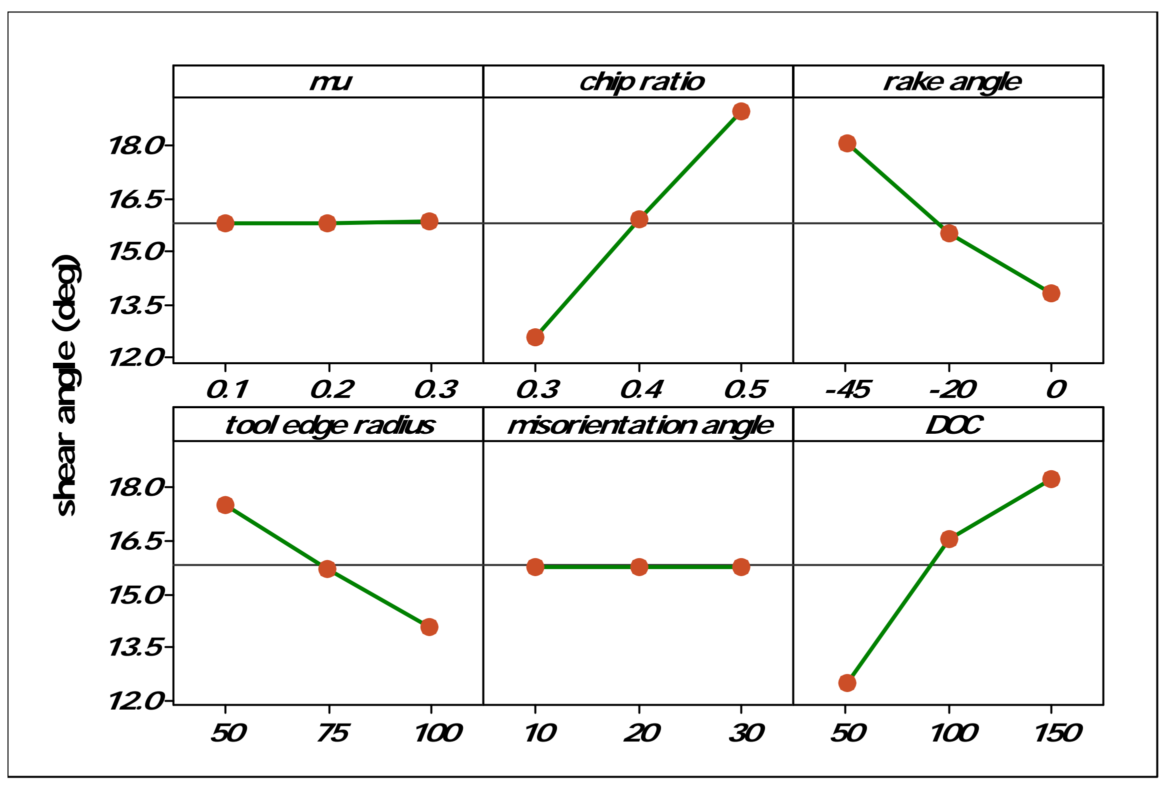

Figure 4.17 Main effects plot for shear angle (φ)

4.3.4 Summary

The effect of microstructure to include grain size, grain boundary, and misorientation on the forces in micro-scale machining has been modeled using the principles of dislocation theory. The cutting forces involved in the machining of *p*-Ge have also been modeled and compared to experimental results. A new set of material constants for the Johnson-Cook model has been derived for *p*-Ge by the process of optimization using experimental results. The following can be observed from the analysis and experiments.

- The cutting forces compare well in both magnitude and trend, while the thrust forces have a deviation in terms of their magnitude though the trend is captured well.
- The ratio of the cutting to thrust force from *Grain A* to *Grain B* agrees reasonably well with the experimental results, indicating that there is an effect of microstructure on the forces.
- The forces are also influenced by the undeformed chip thickness, rake angle, tool edge radius, and friction coefficient. The chip ratio does not have a strong influence on the cutting force, but influences the thrust forces considerably.
- The shear angle is strongly influenced by the rake angle and chip ratio as expected. The coefficient of friction and the misorientation angle do not have any impact on the shear angle.

4.4 Ultraprecision Machining of Polycrystalline Silicon Carbide

The *p*-SiC (Morgan Advanced Ceramics Inc.) used in this work has a cubic structure and was manufactured using a chemical vapor deposition (CVD) process.

Moissanite 3C (mineral name of SiC) was grown as 2 inch diameter wafers with a thickness of 0.5 mm. The material crystal structure, shown in Figure 4.18, has a lattice constant (*a*) of 0.4348 nm and belongs to the space group F-43m (ICSD, 2006).

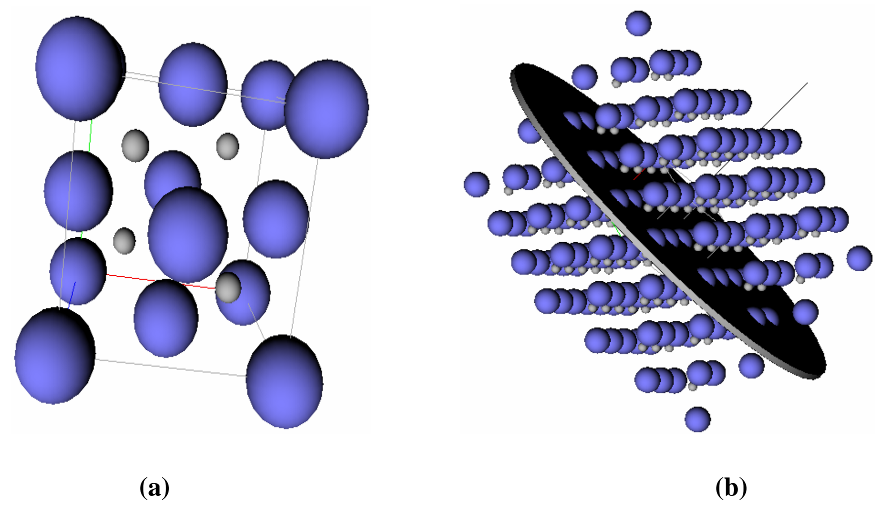

(a) (b)

Figure 4.18 (a) Crystal structure of silicon carbide (left) with the blue atoms representing silicon and the gray atoms representing carbon (b) Multiple unit cells with 100 plane.

Silicon carbide is typically used in high temperature applications such as components for high temperature chambers and etch chambers, gas distribution plates, and also as optical molds and electrostatic chucks. The material is extremely brittle and tough with a high melting point and hardness.

This section details the cutting experiments performed on polycrystalline silicon carbide (*p*-SiC) in order to further validate the model described above. The experimental procedure along with results are discussed and compared with simulated force data. The effect of microstructure on the flow stress and in-turn the forces are also discussed.

4.4.1 Experimental Procedure

The micro cutting experiments on polycrystalline silicon carbide (*p*-SiC) were performed using an ultraprecision lathe and a round nosed single crystal diamond tool. The machine tool and machining set-up are similar to the experimental set-up used for machining silicon described in chapter 3 and are schematically shown in Figure 4.19. The silicon carbide wafer is glued on to an aluminum block using a heat softening glue which in-turn is held on a vacuum chuck. The machining conditions for cutting p-SiC are shown in Table 4-7.

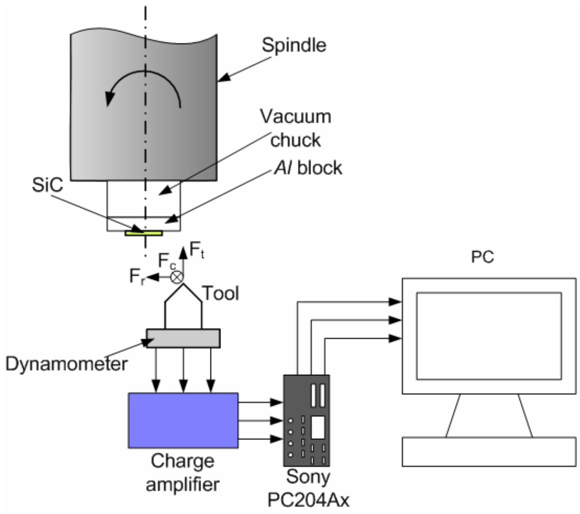

Figure 4.19 Schematic of machining setup and cutting force measurement system

Table 4-7 Machining conditions for polycrystalline silicon carbide

Basic operation	Face turning
Workpiece	Poly-crystalline silicon carbide (*p*-SiC)
Cutting tool	SCD (round nosed) tool
Rake angle	0°
Relief angle	7°
Nose radius	0.5 mm
Cutting speed	1 m/sec
Feed	0.25 µm/rev
Depth of cut (µm)	0.5, 1.0, 5.0, 10.0, 50.0, 100.0, 300.0

4.4.2 Experimental Force Measurements

The cutting forces were measured using a three-axis dynamometer (Kistler 9256A1) and were digitally recorded (Sony PC204Ax). The force data were then downloaded into a computer using special software (PC Scan II). The forces were recorded at a sampling frequency of 24 KHz. The process conditions used for cutting *p*-SiC are shown in Table 4-7. The measured cutting and thrust forces are plotted as shown in Figure 4.20. The undeformed chip thickness is related to the feed (f), tool nose radius (R) and the depth of cut (a_0) as outlined in chapter 3. The undeformed chip thickness for a feed $f = 0.25$ $\mu m/rev$ and $R = 0.5$ mm and different depths of cut are given in Table 4-8.

Table 4-8 Undeformed chip thickness (UCT) for various depths of cut

Depth of cut, a_0 (μm)	UCT (nm)
0.5	11.12
1.0	15.74
5.0	35.21
10.0	49.69
50.0	108.92
100.0	149.96
300.0	229.12

Figure 4.20 Measured cutting and thrust forces for *p*-SiC

4.4.3 Grain Size Measurement

Most engineering materials are, by nature, polycrystalline and consist of three-dimensional aggregate of individual grains, each of which has a different crystal orientation in space. The individual grains are generally of different sizes and shapes. In order to measure the size of the individual grains, many methods have been proposed (Figure 4.21). The first method, termed as caliper diameter method, defines the grain size as the distance between two parallel tangent planes which touch the surfaces of a randomly oriented grain. The second method involves overlaying a set of lines of known length (L) on the image of the sample showing grain boundaries. The number of times a line intercepts a grain boundary is counted as N_L and the grain size is given by $D = L/N_L$. Finally, the number of grains per unit volume of the sample could simply be counted as N_V and the grain size is then given by $D = N_V^{-1/3}$.

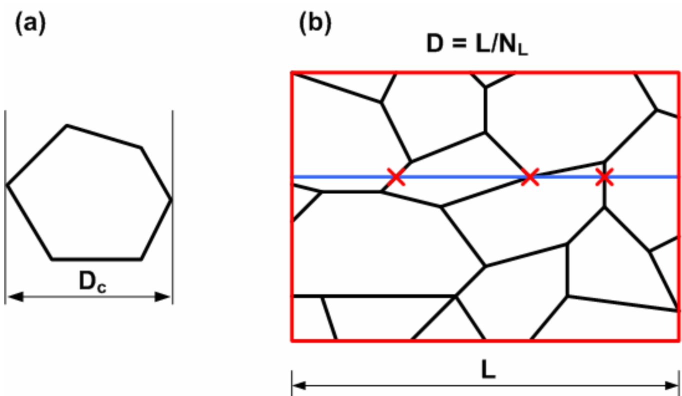

Figure 4.21 Methods for measuring grain size (a) caliper method (b) line intercept method (Brandon & Kaplan, 1999)

The grain size for *p*-SiC was determined using the caliper method. The sample was first scribed using a diamond tip to initiate crack propagation from the surface and was then fractured. The fractured section of the specimen was then examined under the

SEM. The resulting boundaries of the grains were marked as shown in Figure 4.22 and the average grain diameter was determined as 4.7 μm.

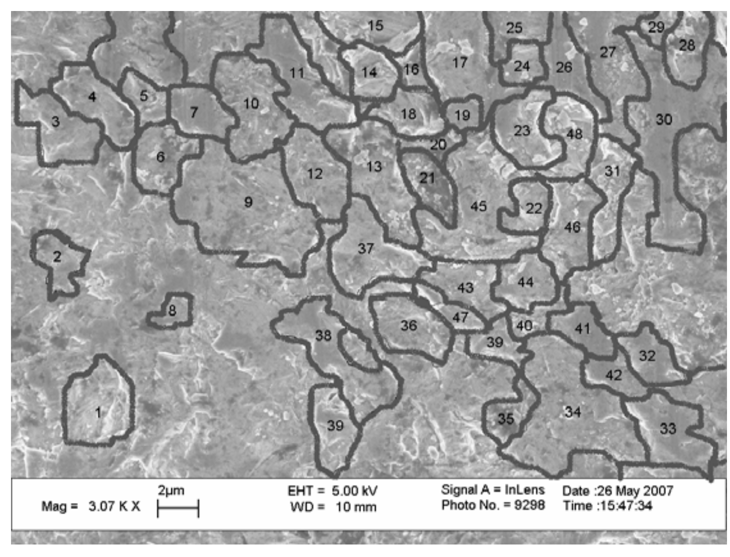

Figure 4.22 Grain size measurements for *p*-SiC

In order to determine the mean and standard deviation of the grain size distribution, which is lognormal as defined in (4.6), the expectation and variance of the distribution have to be defined. The expected value E(D) is given by

$$E(D)=\sum_i p_i D_i \tag{4.13}$$

where p_i is the probability of grain size D_i in the distribution. The variance (Var(D)) can be defined in terms of the expected value as

$$Var(D)=E(D^2)-\left[E(D)\right]^2 \tag{4.14}$$

The mean and the standard deviation can be derived from the expected value and the variance as given by (4.15).

$$\mu = \ln(E(D)) - \frac{1}{2}\ln\left(1 + \frac{Var(D)}{\left(E(D)\right)^2}\right)$$
$$\sigma^2 = \ln\left(1 + \frac{Var(D)}{\left(E(D)\right)^2}\right) \tag{4.15}$$

The distribution of the grain size measurement for *p*-SiC is shown in Figure 4.23a. The expected value and the variance for the grain size data set were computed to be 4.583 and 3.272 respectively. The mean and the standard deviation for the lognormal grain size distribution were computed using (4.15) as 1.4499 and 0.3807 respectively. Therefore the lognormal distribution for the grain size of *p*-SiC is given by (4.16) and shown in Figure 4.23b.

$$f(D) = \frac{1}{0.3807 \cdot \left[\sqrt{2\pi}D\right]} \exp\left(-\frac{1}{2}\left(\frac{\ln(D) - 1.4499}{0.3807}\right)^2\right) \tag{4.16}$$

4.4.4 Surface Texture and Chip Formation

The surface texture for *p*-SiC, both uncut and machined materials, was observed using SEM and the images are shown in Figure 4.24. The uncut surface as received from the vendor was not polished to remove any surface defects, but was finished by grinding as shown by the grind marks in Figure 4.24a. The material removal was not completely ductile, but more of a mixed mode (both ductile and brittle) as seen in images (b), (c) and

(d) of Figure 4.24. The feed was set at $f = 0.25\ \mu m/rev$ and the undeformed chip thickness were in the range of 10 – 35 nm. The areas where the material was removed by ductile mode suggest the presence of high compressive stress beneath the tool thereby preventing crack propagation. Polycrystalline silicon carbide has low fracture toughness and hence the machined surfaces have surface pits and craters on them after the tool passes in some areas.

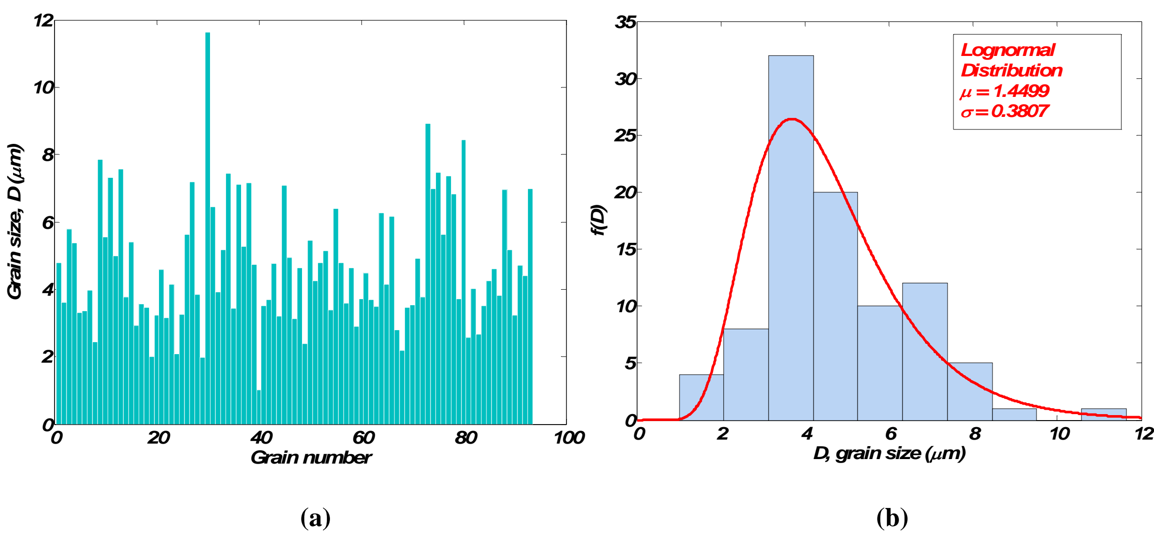

(a) (b)

Figure 4.23 (a) *p*-SiC grain size measurement results (b) lognormal distribution for grain size

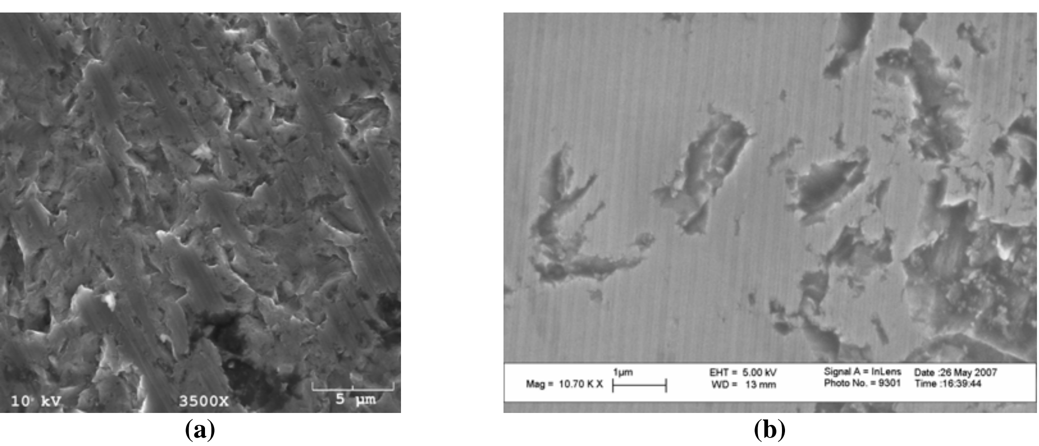

(a) (b)

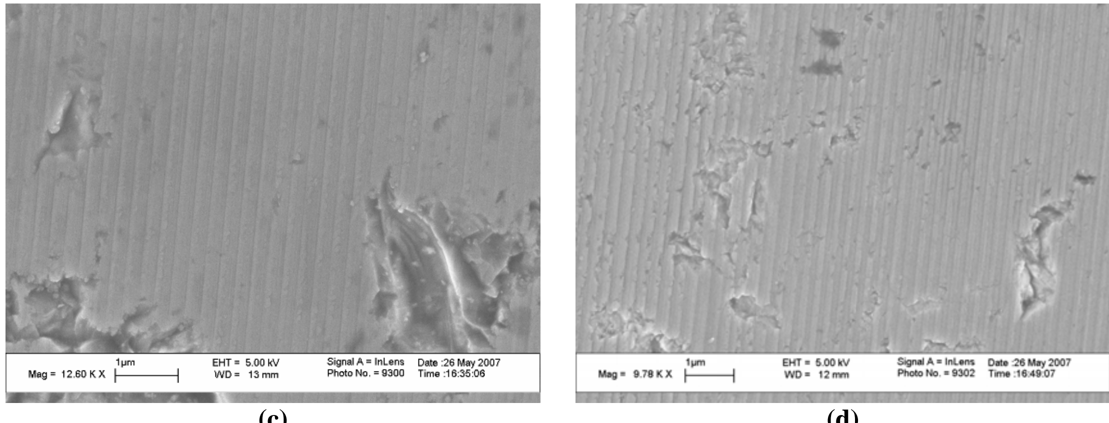

Figure 4.24 (a) SiC wafer as received (b) UCT = 11.11 nm (c) UCT = 15.74 nm (d) UCT = 35.20 nm

4.4.5 Prediction of Forces

The prediction of cutting and thrust forces requires the determination of the shear flow stress which can be obtained using the Johnson-Cook material model. The forces are then evaluated and compared to experimentally measured values. The effect of grain size, grain orientation on the flow stress is also studied. Finally a sensitivity analysis is performed to study the variation of the forces with changes in the input process parameters.

4.4.5.1 Material Constitutive Model

The Johnson-Cook material model discussed in chapter 3 is adopted for silicon carbide. The material model for a brittle material such as silicon carbide is predominantly determined by its fracture characteristics. The applicability of a ductile material model for a fracture mode dominant brittle material is based on the fact that some amount of tangible plastic flow occurs when the undeformed chip thickness is sufficiently small. Failure in a brittle material is due to two competing mechanisms viz., plastic deformation and brittle fracture via crack propagation. Plastic deformation is a volume defect whereas

brittle fracture is an area effect. Therefore, at very small scales less energy is required for the material to deform by plastic deformation than by brittle fracture and the reverse is true for large scale deformation. In the process of microcutting of *p*-SiC, it is assumed that less energy is required for the material to deform plastically than by brittle fracture and hence the Johnson-Cook material model is adopted. It must however be stated that there is a need for a better material model for SiC to describe the response of a brittle material to changes in strain, strain-rate and temperature.

The optimization technique described earlier to determine constants for the Johnson-Cook equation did not produce any reasonable results for the constant *n*. Therefore, the constants were determined by resorting to a trial-and-error method. The predicted forces were compared to the experimental results in order to arrive at the solution for the constants which is shown in Table 4-9.

Table 4-9 Johnson-Cook constants for SiC

A (Pa)	1.4e+09
B (Pa)	2.5e+09
C	0.2
n	0.6
m	1.0

4.4.5.2 Shear Strain and Strain-rate

The strain and strain-rate are computed using two methods as described in chapter 3. The strain and strain-rate results are plotted in Figure 4.25a and Figure 4.25b respectively. The strain predicted using Oxley's (1989) method is higher than the strain predicted by Manjunathaiah and Endres (2000). But the trend for both the methods is the same. The strain-rates predicted by both methods have the same trend, but the Oxley

method predicts a higher value. The values computed using Oxley's method is used in this work.

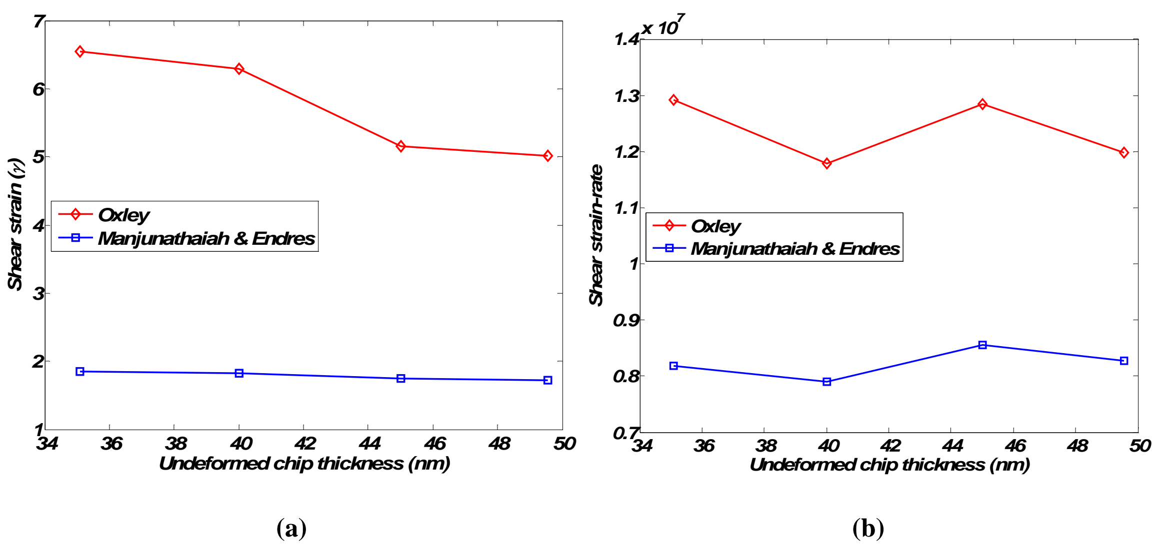

(a) (b)

Figure 4.25 (a) Strain and (b) Strain-rate computation for *p*-Sic

4.4.5.3 Force Prediction

The cutting and thrust forces are predicted using the procedure laid out in chapter 3. The flow stress is computed using the Johnson-Cook equation with constants given in Table 4-9 and shear strain and shear strain-rate as described in the previous section. The forces are compared only for the undeformed chip thickness range of 15 – 50 nm as the nature of deformation is dominated by brittle fracture for higher values. The forces for higher undeformed chip thickness cannot be predicted using this model, as the material model assumes that there is tangible plastic flow. As pointed out earlier, fracture is a more favorable mode of deformation for higher values of undeformed chip thickness. The force values computed using this model, for higher values of undeformed chip thickness, would be far greater than the measured values, as higher energy (and hence forces) is required to remove materials plastically than by brittle fracture. A comparison of the

predicted and experimental forces is shown in Figure 4.26. It should be pointed out that the turning forces were transformed in order to be compared with the measured force values using the procedure discussed in chapter 3. The effect of microstructure was not taken into account, but is discussed separately in the next section. The effect of temperature was also not considered, as the cutting speed in the experiments was small. The predicted forces agree well in both magnitude and trend with the measured experimental forces.

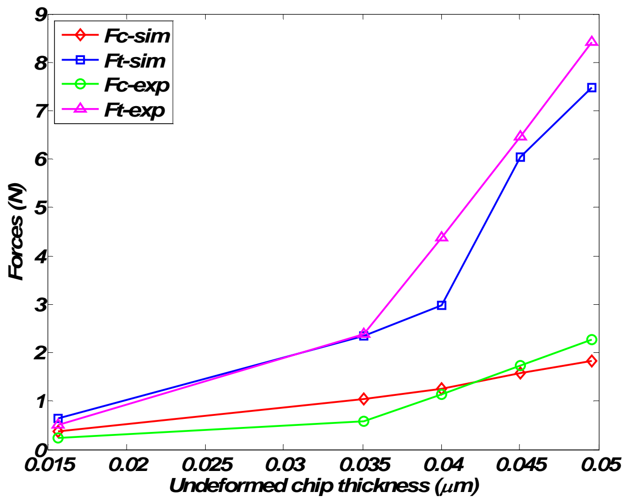

Figure 4.26 Comparison of measured and predicted cutting and thrust forces for *p*-SiC

4.4.5.4 Effect of Microstructure

The effect of grain size, grain boundary and crystallographic orientation on the flow stress and the forces in turn is discussed in this section. The grain size for most materials including p-SiC assumes a lognormal distribution and the average grain size for p-SiC was found to be 4.7 μm as discussed earlier. The effect of grain size on the flow stress as given in (4.5) requires the computation of K_{HP} which is termed as the Hall-Petch

coefficient. The Hall-Petch coefficient is based on the material properties of SiC and is computed using the following relationship (Nes et al., 2005):

$$K_{HP} = M\sqrt{\frac{\tau_b 4Gb}{(1-\upsilon)\pi}} \tag{4.17}$$

where M is the Taylor factor, τ_b is the critical grain boundary stress, G is the shear modulus and υ is the poisson ratio. The material properties of SiC are given in Table 4-10. The critical grain boundary shear stress is given by (von Blackenhagen et al., 2001)

$$\tau_b = 0.057 \cdot G \tag{4.18}$$

The value of K_{HP} is computed as 3.0129 $MPa.m^{1/2}$ assuming M = 3. The variation of grain size causes a variation in the normal flow stress according to the Hall-Petch relation given by (4.19). In order to isolate the effect of grain size variation, the normal flow stress in (4.5) is redefined as

$$\sigma = \sigma_o(\varepsilon, \dot{\varepsilon}, T) + K_{HP} D^{-1/2} \tag{4.19}$$

where σ_o is given by the Johnson-Cook equation defined in chapter 3. The grain size D in the above equation follows a lognormal distribution as given by (4.6). The resulting normal stress is also distributed in a lognormal manner due to the variation of D. The plot in Figure 4.27a shows the variation of normal stress as a function of grain size (D). The

red (dashed) line represents the normal stress without the consideration of the grain size effect. This stress only includes the effects of strain and strain-rate as given by the Johnson-Cook equation. The blue (solid) line indicates the probability density function of the normal stress as a function of grain size. The black (dashdot) vertical line indicates the grain size with the highest probability (D = 3.43 μm). The green (dotted) line indicates the variation of the normal stress as a function of grain size. The normal stress varies inversely with the square root of the grain size and so an increase in grain size results in a decrease in the normal flow stress. This increase in normal stress for smaller grain size is due to the fact that grain boundaries act as barriers to the motion of dislocations. The contribution of Hall-Petch relation to the overall flow stress ranges between 3 – 10 %. A more conventional plot of the normal stress as a function of the inverse of the square root of grain size is shown in Figure 4.27b.

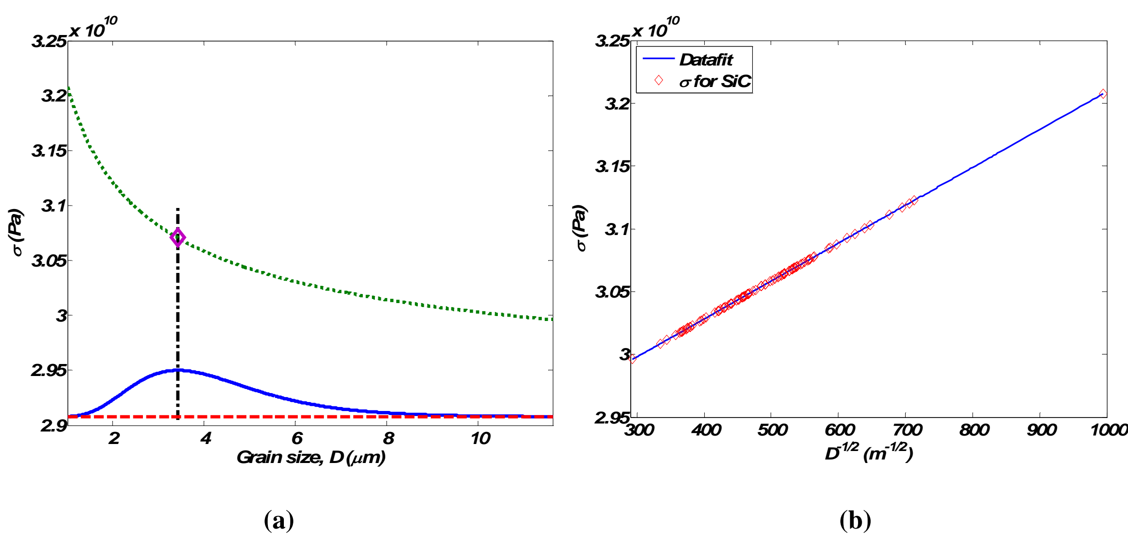

Figure 4.27 (a) Variation of normal flow stress with grain size, D (b) conventional plot of normal stress versus square root of grain size

Table 4-10 Properties of silicon carbide

Property	Value/Representation	Reference
Chemical composition	SiC	
Burgers vector (*b*)	0.308 *nm*	Suzuki et al., 1995
Crystal structure	Many crystalline forms	
Density (ρ)	3.2 g/cm^3	Kovacs, 1998
Melting point	2730 ^oC	
Coefficient of thermal expansion (CTE)	3.3 x 10^{-6} K^{-1}	Kovacs, 1998
Thermal conductivity (*k*)	3.5 *W/cm.K*	Kovacs, 1998
Young's modulus (*E*)	450 *GPa*	Morgan Advanced Ceramics Inc., Data Sheet
Hardness (*H* – Vickers)	2800 Kg/mm^2	Morgan Advanced Ceramics Inc., Data Sheet
Fracture toughness (K_{Ic})	2.94 $MPa.m^{1/2}$	Morgan Advanced Ceramics Inc., Data Sheet
Poisson ratio (υ)	0.183 – 0.192	Shackelford and Alexander, 2001
Yield strength (σ_0)	21.0 *GPa*	Kovacs, 1998
Shear modulus (*G*)	192 *GPa*	Suzuki et al., 1995

In addition to the grain size, grain boundaries and crystallographic orientation also affect the characteristic response of the material to deformation. Polycrystalline aggregates typically either have their individual grains oriented randomly with respect to a reference or tend to cluster about some particular orientation(s). A polycrystalline material characterized by clustering of grains towards particular orientation(s) is termed to have a preferred orientation or texture. In order to determine if the *p*-SiC sample had texture associated with it, an X-ray diffraction (XRD) analysis was performed.

Diffraction occurs when a beam of X-rays is incident on a set of crystal planes as shown in Figure 4.28. From the figure, two geometrical facts can be inferred: (i) The incident beam, the normal to the reflecting plane and the diffracted beam are always coplanar. (ii) The angle between the diffracted beam and the transmitted beam is always 2θ. The requirement for diffraction to occur is that the wavelength of the wave motion is

of the same order of magnitude as the repeat distance between scattering centers. This requirement follows from Bragg's law which can be given by the following relation:

$$\lambda = 2d \sin\theta \tag{4.20}$$

where λ is the wavelength of x-rays, d is the distance between two adjacent crystal planes and θ is the Bragg angle.

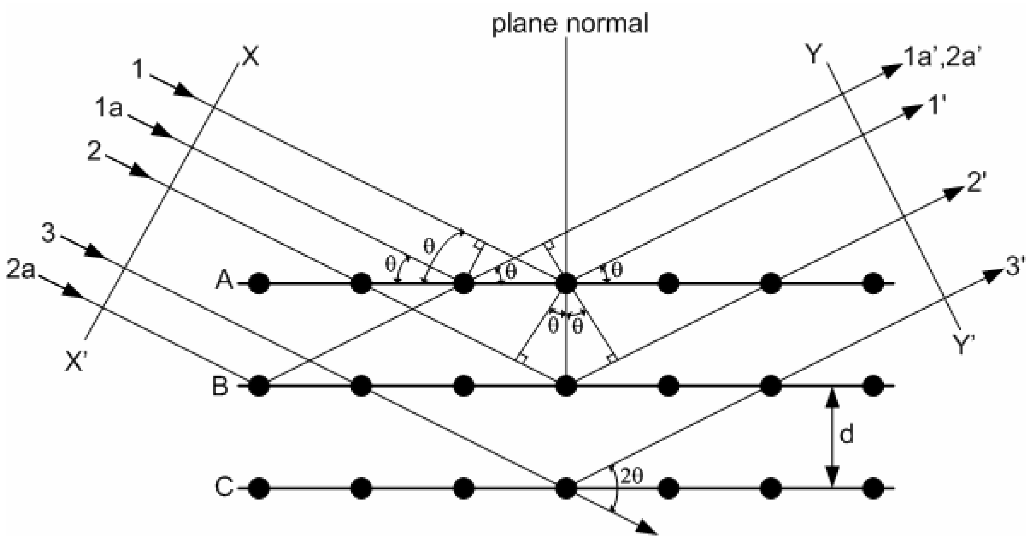

Figure 4.28 Diffraction of X-rays by a crystal (Cullity, 1978)

The XRD experiments for p-SiC were performed on X'Pert PRO MRD instrument (PANalytical) as shown in Figure 4.29. The instrument has a four-axis goniometer that is used to set the sample in a particular orientation relative to X-ray beam. The detector is a parallel plate collimator having a poly-capillary lens with a nickel filter.

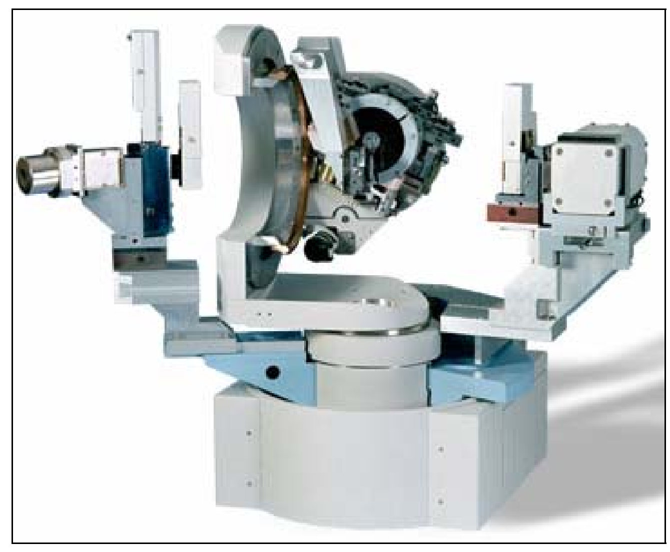

Figure 4.29 X'Pert PRO MRD instrument (PANalytical)

The XRD experiment was performed on a 10x10x0.5 mm *p*-SiC sample and the relationship between scattered intensity (*I*) and 2θ (Bragg angle) was studied. For a crystalline material the curve of I vs. 2θ is almost zero everywhere except at certain angles where high sharp maxima occur representing the diffracted beams. A similar curve for *p*-SiC is given in Figure 4.30 which shows that the polycrystalline silicon carbide material does exhibit texture or preferred orientation.

The effect of crystallographic orientation on the material flow stress required the determination of misorientation distribution by performing electron back scattering diffraction (EBSD) experiments and studying kikuchi patterns. The process of preparing the sample for EBSD experiments involved the use of different surface preparation techniques as shown in Table 4-11. It must be mentioned that despite the different surface preparation techniques, none of them resulted in a definite kikuchi pattern and hence the misorientation could not be determined. Therefore a sensitivity analysis was performed

by varying the misorientation angle over the range of 0 – 62.8° (Mackenzie, 1958) for cubic crystals.

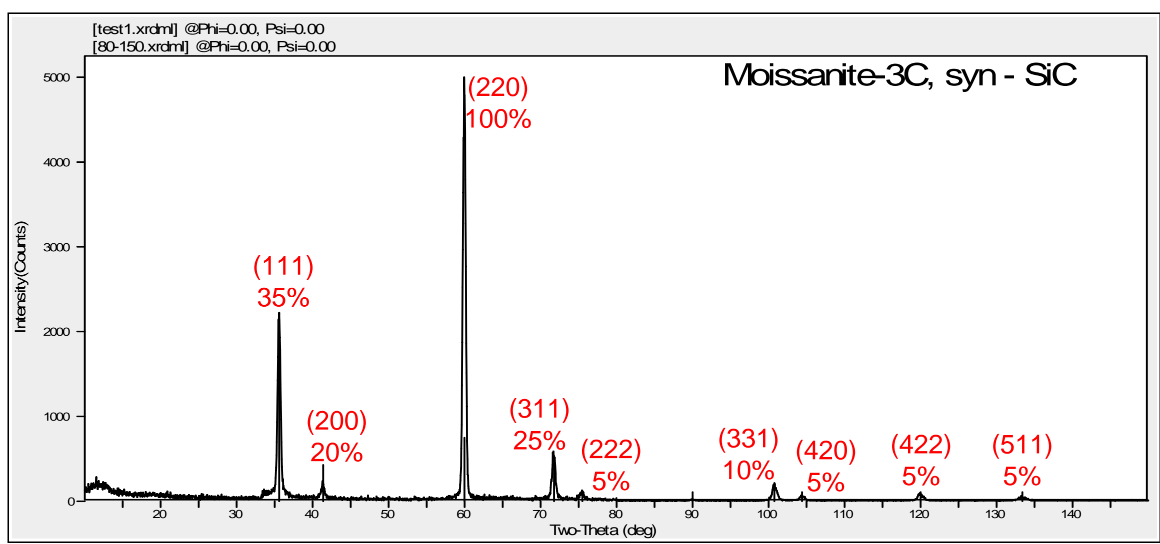

Figure 4.30 Intensity (*I*) vs. 2*θ* for *p*-SiC

Table 4-11 Sample preparation techniques for EBSD experiments

Sample	Method	Time
1	P1200 grit grinding disc	30 min
	9 μm diamond suspension	30 min
	3 μm diamond suspension	30 min
	1 μm diamond suspension	30 min
	0.05 μm polishing suspension (Al_2O_3)	30 min
2	0.05 μm colloidal silica (vibratory polisher)	15 hrs
3	0.05 μm polishing suspension – Al_2O_3 (vibratory polisher)	20 hrs
4	Ion milling	--

4.4.5.5 Effects of microstructure on cutting and thrust forces

The effect of microstructure on the normal flow stress is discussed in the previous section. The forces are also affected the same way as the shear flow stress, as they are

derived from them as discussed in the force model in chapter 3. The cutting and thrust force values are plotted in Figure 4.31 both while excluding and including the effects of microstructure (grain size, grain boundary and crystallographic orientation). The plot shows that the force variation is only around 9 – 11 % of the nominal values. The values of constants considered while computing the flow stress from (4.5) are: $M = 3$, $k = 4$, $\theta_{av} = 30^{o}$, and $\alpha = 0.5$ (constants are defined in Table 4-5).

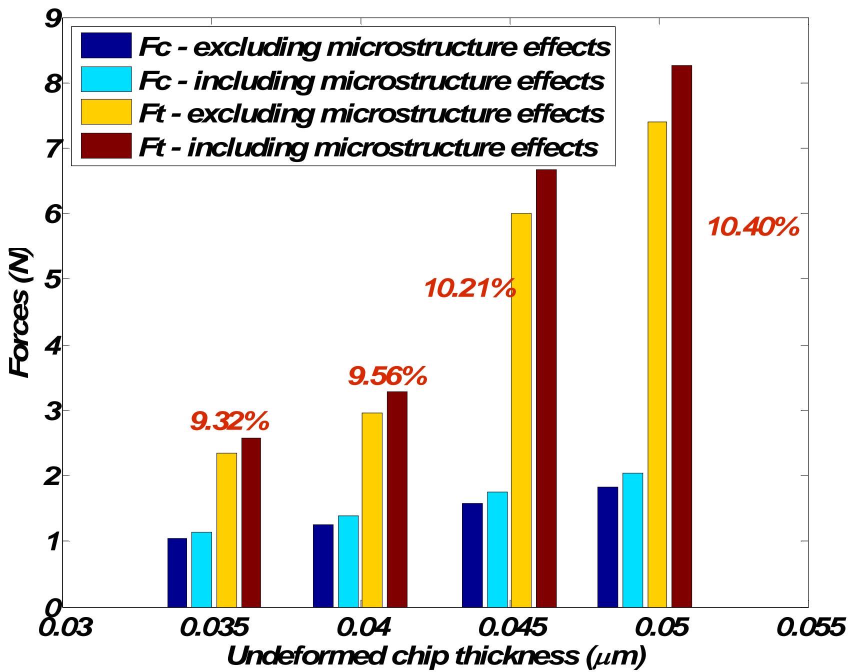

Figure 4.31 Force comparisons illustrating the effects of microstructure

A sensitivity analysis is performed to study the effects of microstructure on the resulting cutting and thrust forces. The analysis is performed by employing a three-level, five factor full factorial design ($3^5 = 243$ runs) as shown in Table 4-12. The input process parameters for this analysis are: undeformed chip thickness, $t_0 = 49.54$ nm; coefficient of friction, $\mu = 0.27$; and nominal rake angle, $\gamma = 0^{o}$.The results of the analysis are shown in

Figure 4.36 and Figure 4.37, corresponding to cutting forces and thrust forces respectively. The results show that the grain size, misorientation angle and α have a significant influence while the Taylor factor (M) and k representing the geometry of the boundary have lesser influence on the forces. The scale of the y-axis of the plots for both the cutting and thrust forces can be misleading. These forces represent the variation when the given input factor levels are changed and should not be confused with the force variation when the effects of microstructure are considered (Figure 4.31). The microstructural effects can cause a variation of around 10% as discussed previously.

Table 4-12 Design of experiments analysis for *p*-SiC

Factor	Low	Medium	High
Taylor factor (M)	2.5	2.75	3
constant – geometry of boundary (k)	2	3	4
Constant (α)	0.2	0.35	0.5
Grain size (D – μm)	2.0	5.0	8.0
Misorientation angle (θ – degrees)	10	30	50
Responses – Cutting force (F_c), Thrust Force (F_t)			

In order to determine if the effect of microstructure did cause a variation in the cutting and thrust forces, the forces data was further analyzed. The plots in Figure 4.32a and Figure 4.32b show the force data for a period of 0.5 *sec* and one revolution respectively (N = 616.1 *rpm*). From the plots it is difficult to categorize the variations as those arising from a variation in grain size. The force data was recorded at a frequency of 24 KHz and the cutting velocity was held constant at 1 m/sec. The average grain size of the silicon carbide sample was determined to be 4.7 μm. The tool would, at this grain size level, pass through 2e+05 grains every second. Therefore, in order to detect any force

variation at such small grain size levels, the sampling frequency would have to be higher or the cutting speed reduced by at least two orders of magnitude. Hence a comparison between experimental force variation and the results of simulation would not be valid.

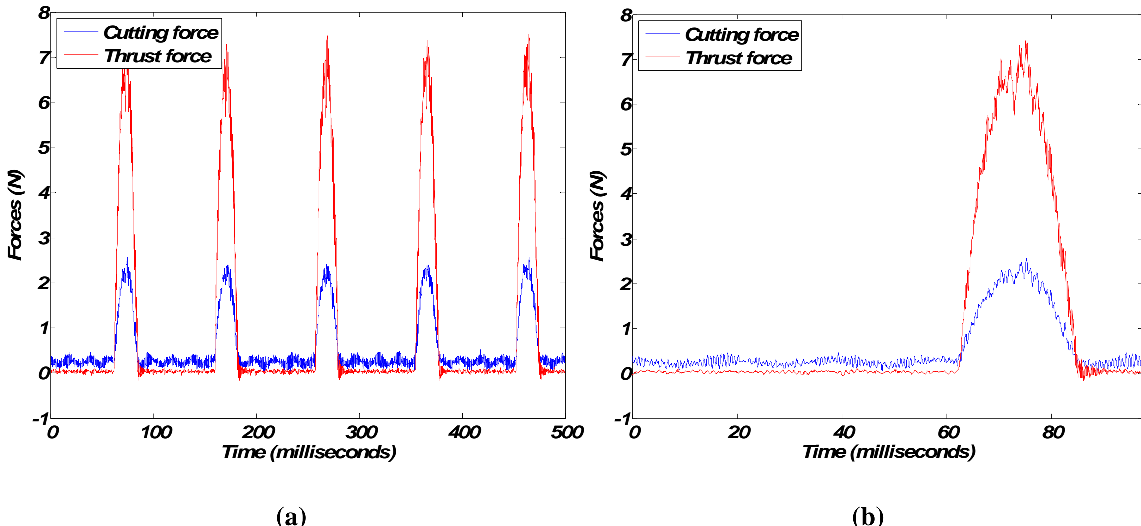

(a) (b)

Figure 4.32 Force variations for a period of (a) 0.5 sec and (b) one revolution

In order to further investigate the effect of microstructure, a molecular dynamics (MD) simulation of machining polycrystalline SiC was performed by Cai and Li (2007). The results of the simulation are discussed here briefly. The *p*-SiC has a cubic structure which is modeled using Tersoff potential and the interaction between *p*-SiC and the diamond tool (considered rigid) is described by Morse potential. The simulation considers *p*-SiC being composed of two grains *A* and *B* which are differ in their orientation by 30 degrees as shown in Figure 4.33.

The workpiece dimensions for the MD simulation was $46a \times 20a \times 4a$, where a is the lattice constant. The environment temperature was 293 K and the cutting velocity was 20 m/sec. The tool edge radius (r) was 2.5 nm while the undeformed chip thickness was set at 2 nm. The deformation zone near the grain boundary is shown in Figure 4.34. The

deformation zone in Grain A is larger compared to Grain B. The springback for Grain A is also greater than Grain B. The difference in the responses between the two grains also shows up in the cutting and thrust forces. The forces for Grain B are greater than that of Grain A as shown in Figure 4.35. The results of the MD analysis also demonstrate the effect of grain boundary on the cutting and thrust forces as predicted by the model discussed in the previous section. It must be noted that the force levels in MD simulations are many orders of magnitude smaller than the actual measured forces.

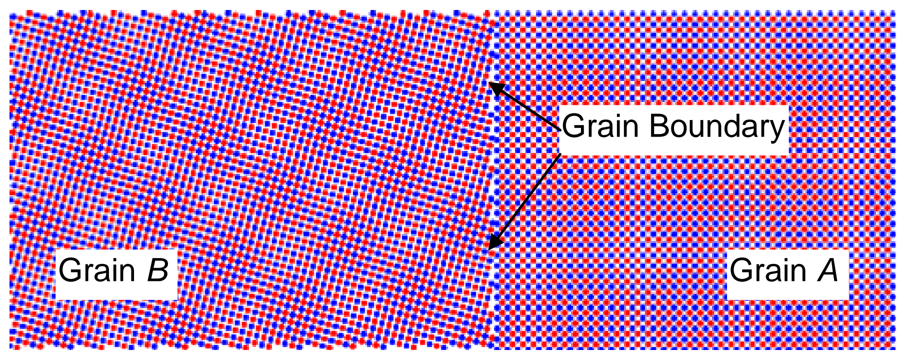

Figure 4.33 Simulation representation of two grains of *p*-SiC

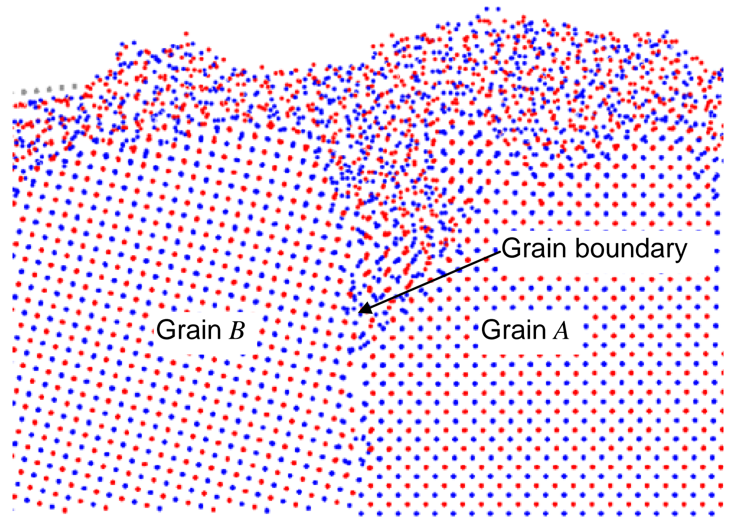

Figure 4.34 Deformation in the grain boundary zone

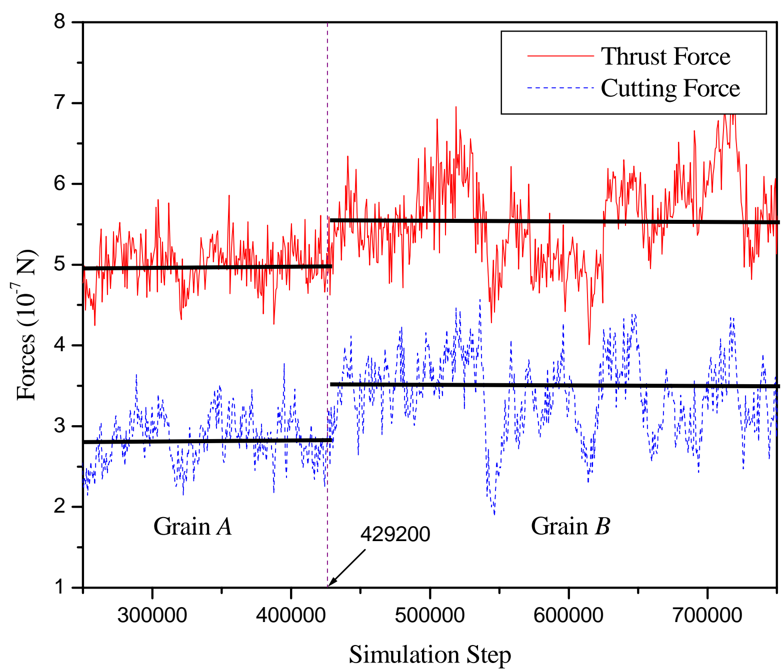

Figure 4.35 Simulated cutting and thrust forces

The mean cutting and thrust forces obtained from MD simulations for grain *A* are 2.79e-07 *N* and 5.1e-07 *N* respectively while those obtained for grain *B* are 3.5e-07 *N* and 5.62e-07 *N* respectively (Figure 4.35). The magnitudes of the forces are much smaller in comparison to predicted and experimental force values (Figure 4.26) and therefore a comparison may not be applicable. However, a comparison of the ratio of forces is relevant. But the MD simulation does not take the grain size into account due to the scale of the simulation process. Therefore the forces computed using the prediction model discussed above did not consider the effect of grain size. The misorientation value was set at 30°, similar to the MD model. The prediction of forces resulted in a variation of 8 – 10% (for both cutting and thrust forces) when the effect of grain boundary and crystallographic orientation were included. The MD simulation shows a variation of around 25% for the cutting forces and 11% for the thrust forces. The percentage variation

for the thrust direction is comparable while those for the cutting direction are slightly higher for the MD model. Thus the MD approach essentially reiterates the effect of microstructure on the forces during the process of ultraprecision machining.

4.4.5.6 Summary

Micromachining of *p*-SiC was performed and force measurements were compared to the simulation results. A new set of constants for the Johnson-Cook equation was determined. The predicted forces both in the cutting and thrust directions matched well, in magnitude and trend, with the experimental results. The average grain size of p-SiC was determined to be 4.7 μm. The effect of microstructure on the force variation was determined to be in the range of 7 – 11% from the model. However, a comparison to experimental results could not be performed as the sampling frequency was too low to pick up any force variation.

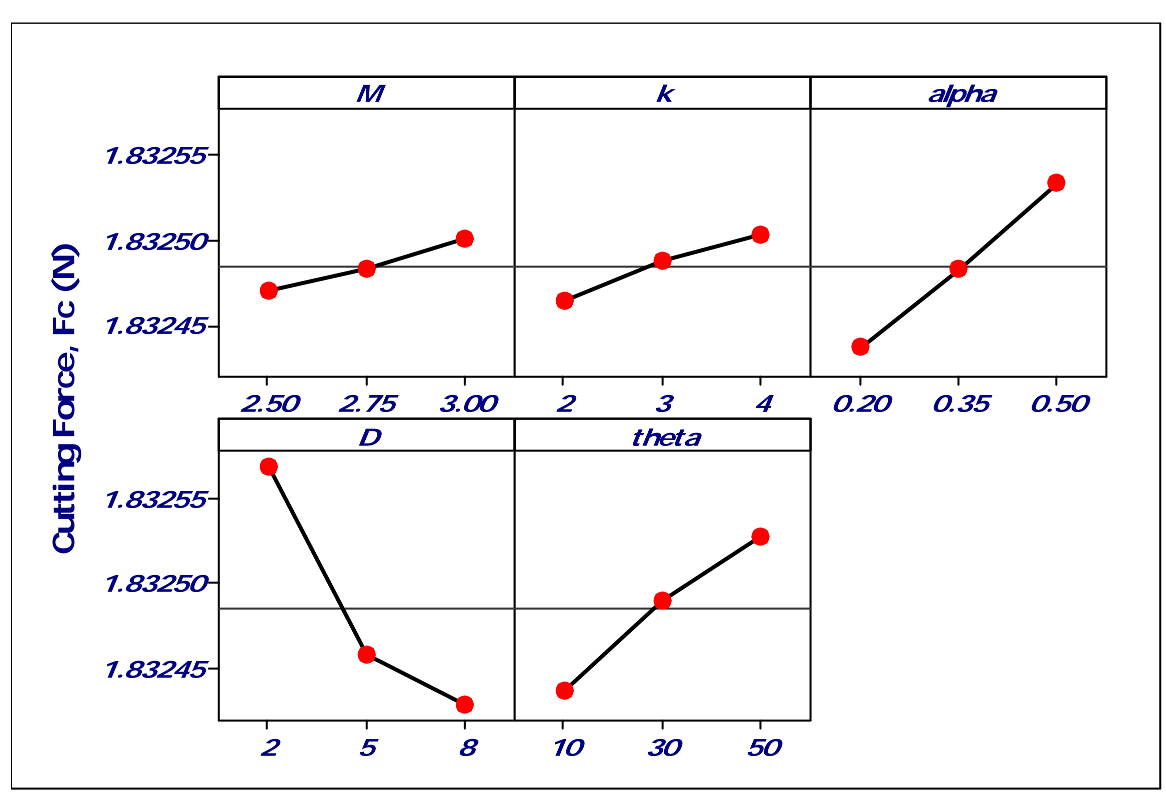

Figure 4.36 Main effects plot for cutting force (F_c)

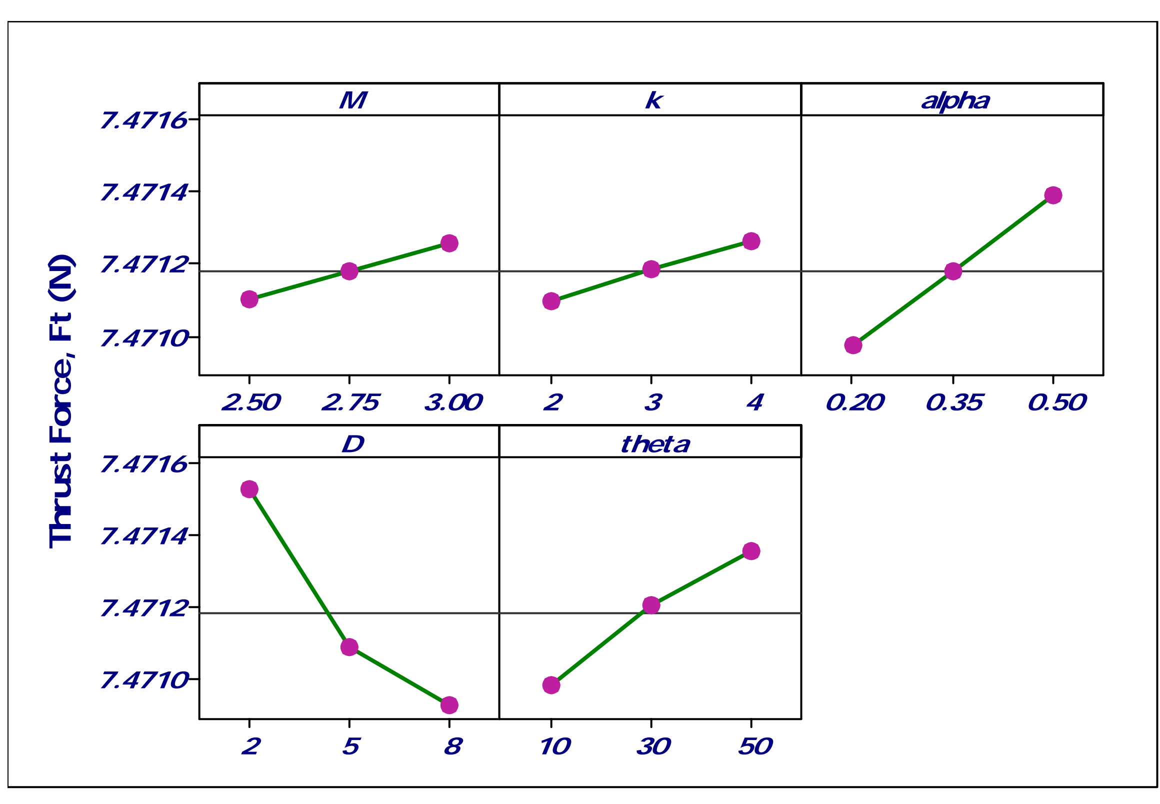

Figure 4.37 Main effects plot for thrust force (F_t)

4.5 Chapter Summary

The effects of microstructure including grain size, grain boundary and crystallographic orientation are modeled using the theory of dislocations. The application of stresses in a material due to the tool moving over the workpiece causes plastic deformation. The plastic deformation can lead to chip formation during machining and ploughing of material beneath the tool edge. The basis for the plastic deformation process is the movement of dislocations. Brittle materials typically have little dislocation movement in the macro-scale due to their low strength against fracture. But when machining is performed at sufficiently small scale the material is removed by ductile means, which can be beneficial. The next logical step in the analysis of machining polycrystalline materials would be to predict the transition undeformed chip thickness using a procedure similar to the model described for single crystal materials in chapter 3. The machining of polycrystalline materials would be beneficial in terms of reducing production cost and increasing material removal rates, and thereby enhancing productivity.

CHAPTER 5

CONCLUSIONS AND FUTURE WORK

5.1 Dissertation Overview

This dissertation presents a predictive modeling methodology to determine the transition undeformed chip thickness for ductile-regime machining of single crystal brittle materials. The model uses information about the properties of the material being machined including hardness, fracture toughness, elastic modulus etc.; the tool geometry specifications such as rake angle, edge radius, nose radius etc.; and the process conditions such as cutting velocity, feed, undeformed chip thickness etc. as its input parameters. The force model described in chapter 3 predicts cutting and thrust forces by considering an infinitesimally small area around the rounded edge of the tool and evaluating the incremental forces in that area. The incremental forces are integrated around the edge of the tool where the tool contacts the workpiece. The forces include both the chip formation and ploughing forces, though they are not represented separately. The transition between ductile and brittle mode of material removal occurs when the stress intensity factor equals the fracture toughness of the material. Also, the resolved shear stress exceeds the critical flow stress of the material in order to facilitate material removal via continuous chip formation. The model is validated by performing micro-machining experiments on an ultra-precision lathe using single crystal silicon as the workpiece material. A sensitivity analysis is also performed to determine the significant factors affecting both the forces and ultimately the transition undeformed chip thickness.

The machining of polycrystalline brittle materials, discussed in chapter 4, is a more complex process compared to machining of single crystal brittle materials. The complexities arise because the effects of microstructure (grain size, grain boundaries, and crystallographic orientation) become significant at the scale where the grain size is of the same order of magnitude as the undeformed chip thickness. The effects of microstructure on flow stress are modeled based on dislocation density. The grain size effect is captured using the Hall-Petch model which predicts an increase in the material strength with a decrease in the grain size. The misorientation between two adjacent crystals is related to the total dislocation density which includes effects of grain boundaries, both geometrically necessary boundaries and incidental dislocation boundaries. The model is verified by comparison with two sets of experimental data: (i) published results for ultra-precision machining of polycrystalline germanium, (ii) experiments performed on polycrystalline silicon carbide. A sensitivity analysis is performed to determine the significant factors affecting the cutting and thrust forces for both materials.

5.2 Conclusions and Contributions

The motivation to develop a predictive model to determine the transition undeformed chip thickness in ductile-regime machining arises due to the enormous cost and time involved in resorting to trial-and-error methods to determine the optimum machining conditions. The contributions and conclusions from Chapter 3 are listed as follows:

- Developed a force model to predict cutting and thrust forces in the field of micro-machining.

    - The force model was validated for single crystal silicon by comparing with experimental results. The cutting and thrust forces matched well in both trend and magnitude with experimental results.
    - A sensitivity analysis performed on cutting and thrust forces suggested that undeformed chip thickness, tool edge radius and rake angle significantly affected the variation in forces.
    - The shear angle was significantly influenced by the chip ratio, rake angle, undeformed chip thickness and tool edge radius.
    - A new set of constants for the Johnson-Cook material model equation was determined using a Nelder-Mead optimization procedure which involved a comparison of force values with experimental results.

- Developed a comprehensive model to determine the transition undeformed chip thickness for micro-machining of single crystal brittle materials.
    - The undeformed chip thickness for single crystal silicon was determined from the model to be 62.37 nm.
    - Machining experiments were performed on Si (111), (100), (110) for various input process conditions.
    - The machined surfaces were analyzed on a SEM for texture and the roughness was measured on a white light interferometer. The surfaces generated at or below 60 nm revealed ductile material removal. Moreover, evidence of chip formation was found from the chips collected for the different process conditions.

    - The cutting velocity and the nominal rake angle had a significant influence on the transition undeformed chip thickness value. A higher cutting velocity and a higher negative rake angle led to increased transition chip thickness values.

The machining of polycrystalline brittle materials and the effect of microstructure on machining process parameters was discussed in chapter 4 and some of the contributions and conclusions are listed below.

- The effects of microstructure including grain size, grain boundary and crystallographic orientation on the flow stress are modeled using the theory of dislocations.
- The model was validated using published experimental data on ultra-precision machining of polycrystalline germanium.
    - The cutting and thrust force data matched well with the predicted results in both magnitude and direction with a maximum error of 22%.
    - The effect of grain boundary and misorientation between two grains of germanium was studied. The ratio of forces between grains agreed reasonably with the experimental values.
- The model was also validated by performing experiments on polycrystalline silicon carbide.
    - The force prediction matched well with the experimental results and a new set of constants for Johnson-Cook equation was determined.

- The average grain size for the polycrystalline sample was determined to be 4.7 μm. However, the EBSD experiments to determine the misorientation distribution proved to be unsuccessful.
- A sensitivity analysis was performed to determine the significant microstructure effects on the stress and ultimately the forces.

5.3 Recommendations for Future Work

The research presented in this dissertation provides a foundation to determine the transition undeformed chip thickness for machining single crystal brittle materials. The transition undeformed chip thickness is a key process parameter in machining brittle materials to ensure generation of high quality surfaces. The field of ductile-regime machining is a relatively new research area with research emphasis over the last two decades. Therefore, a need for a thorough understanding of the basic process mechanics in order to better predict forces and optimum process parameters still exists.

Although the predictive model helps in eliminating trial-and-error to find the optimal process parameters, there is still room for improvement for better results. In recent years there has been a different approach to the understanding of ductile regime machining. The machining of brittle materials is a complex process involving the understanding of different concepts such as mechanics of tool-chip-surface interaction, high pressure phase transformation, tool wear, material constitutive modeling, motion of dislocation resulting in plastic deformation, temperature effects, fracture characteristics etc. as shown in a schematic in Figure 5.1.

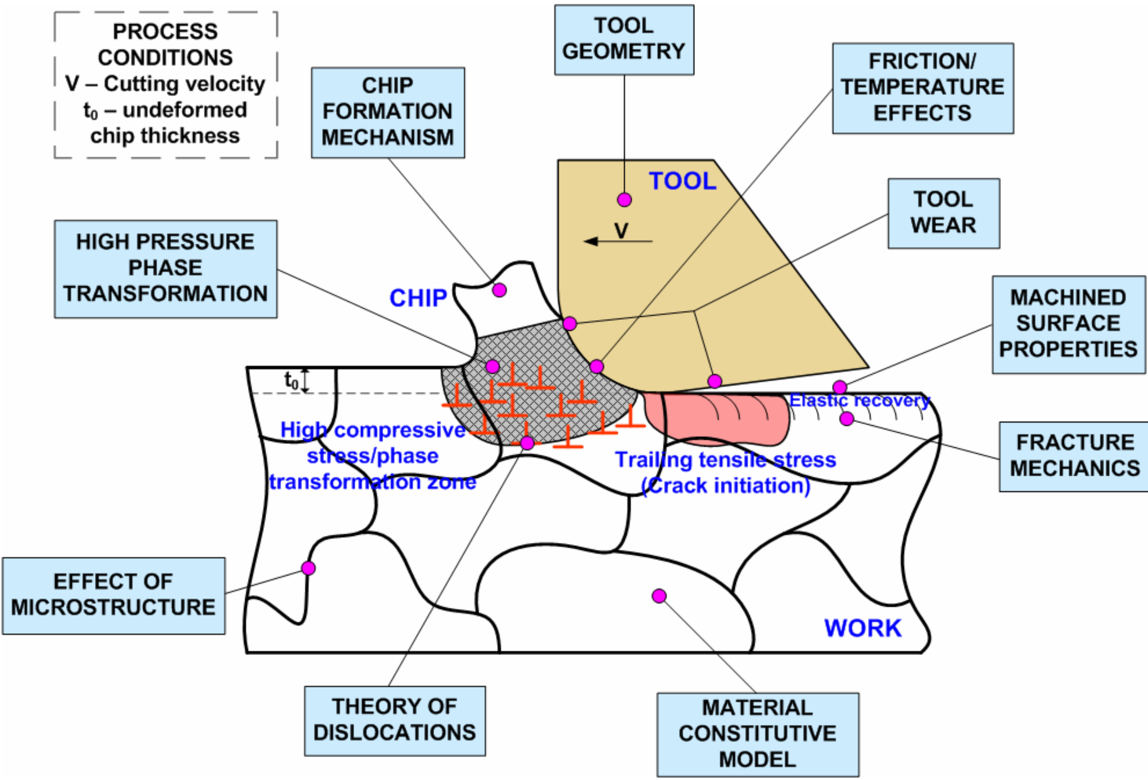

Figure 5.1 Complexities involved in ductile-regime machining

The fact that compressive stresses prevent crack propagation and thus lead to continuous chip formation is widely accepted. It has been suggested recently that the process of ductile regime machining occurs due to a high pressure phase transformation due to the existence of high compressive stresses beneath the tool edge. There is experimental evidence that the transformation of crystalline material to an amorphous phase occurs in the high pressure zone for materials such as silicon and silicon carbide, though there is some amount of embedded crystallites in the chips formed. The process of inducing plastic deformation to a material has always been understood to be through the motion of dislocations which also play a part in the formation of chips. This complex interplay between the phase transformations and the motion of dislocations needs to be further investigated to better understand the ductile-regime machining process.

There is also a need for a better material model to describe the behavior of brittle materials in response to changes in strain, strain rate and temperature. Vodenitcharova and Zhang (2004) presented a material model based on the phase transformation for silicon. It would be highly beneficial to develop a unified material model for brittle materials based on their response to applied stresses (both compressive and tensile).

Tool wear has been reported to be a significant problem in the machining of brittle materials. The effects of tool wear would also affect the finished surface properties. The progression of tool wear has an influence on the tool edge radius which is an important parameter in ductile-regime machining. The effect of tool wear could be incorporated into this model for better results.

The effect of temperature may also be significant at high material removal rates which involve high cutting velocities. The influence of temperature can be captured using existing temperature models for improvement in results for higher cutting velocities.

The surface finish after ductile-regime machining also requires more research, as it has been suggested that a thin layer of amorphous material is left behind after machining. The characteristic of the workpiece and its response to the tool moving over it would then differ from that observed in machining a crystalline material.

The implementation of the above improvements would result in a more reliable and comprehensive predictive model to describe the ductile-regime machining process. A better knowledge of the process can enhance its capabilities to many more brittle materials and composites that have properties close to a brittle material.

REFERENCES

Adbelmoneim, M. ES., Scrutton, R. F., 1974, "Tool Edge Roundness and Stable Build-up Formation in Finish Machining," ASME J. Eng. Ind., **96** (4), pp. 1258-1267.

Albrecht, P., 1960, "New Developments in the Theory of Metal Cutting Process," ASME J. Eng. Ind., **82**, pp. 348-358.

Anurag, S., Guo, Y. B., 2006, "A Micromechanical Approach to Determine Flow Stress of Work Materials Experiencing Complex Deformation Histories in Manufacturing Processes," *Proceedings of International Conference on Manufacturing Science and Engineering*, Ypsilanti, MI, USA.

Arsecularatne, J. A., Zhang, L. C., 2004, "Assessment of Constitutive Equations used in Machining," Key Eng. Mat., **274-276**, pp. 277-282.

Asai, S., Taguchi, Y., Horio, K., Kasai, T., Kobayashi, A., 1990, "Measuring the Very Small Cutting-Edge Radius for a Diamond Tool Using a New Kind of SEM Having Two Detectors," CIRP Ann-Manuf. Techn., **39** (1), pp. 85-88.

Basuray, P. K., Mishra, B. K., Lal, G. K., 1977, "Transition from Ploughing to Cutting During Cutting with Blunt Tool," Wear, **43**, pp. 341-349.

Bhattacharya, B., Patten, J. A., Jacob, J., 2005, "Ductile Regime Nano-Machining of Polycrystalline Silicon Carbide," *Proceedings of 2005 Annual Meeting of ASPE*, Norfolk, VA, USA.

Bhattacharya, B., Patten, J. A., Jacob, J., 2006, "Single Point Diamond Turning of CVD Coated Silicon Carbide," *Proceedings of International Conference on Manufacturing Science and Engineering*, Ypsilanti, MI, USA.

Bifano, T. G., Dow, T. A., Scattergood, R. O., 1991, "Ductile-Regime Grinding: A New Technology for Machining Brittle Materials," J. Eng. Ind.-T ASME, **113**, p 184-189.

Bitans, K., Brown, R. H., 1965, "An Investigation of the Deformation in Orthogonal Cutting," Int. J. Mach. Tool Des. Res., **5**, pp. 155–165.

Blackley, W.S., Scattergood, R.O., 1990, "Crystal Orientation Dependence of Machining Damage – A Stress Model," J. Am. Ceram. Soc., **73** (10), pp. 3113-3115.

Blackley, W.S., Scattergood, R.O., 1991, "Ductile-Regime Machining Model for Diamond Turning of Brittle Materials," Precis. Eng., **13** (2), pp. 95-103.

Blake, P. N., Scattergood, R. O., 1990, "Ductile-Regime Machining of Germanium and

Silicon," J. Am. Ceram. Soc., **73** (4), pp. 949-957.

Brandon, D. G., Kaplan, W. D., 1999, *Microstructural Characterization of Materials*, John Wiley & Sons, Ltd., Chichester, UK.

Cai, M. B., Li, X. P., 2007, Personal Communication (unpublished work).

Cai, M. B., Li, X. P., Rahman, M., 2007, "Study of the Mechanism of Nanoscale Ductile Mode Cutting of Silicon using Molecular Dynamics Simulation," Int. J. Mach. Tools Manuf., **47**, pp. 75-80.

Chao, C. L., Ma, K. J., Liu, D. S., Bai, C. Y., Shy, T. L., 2002, "Ductile Behavior in Single-Point Diamond-Turning of Single-Crystal Silicon," J. Mater. Process. Technol., **127**, pp. 187-190.

Cheng, J., Nemat-Nasser, S., Guo, W., 2001, "A Unified Constitutive Model for Strain-rate and Temperature Dependent Behavior of Molybdenum," Mech. Mater., **33**, pp. 603-616.

Cohen, P. H., Black, J. T., Horne, J. G., Shih, A. A., 1981, "Orthogonal Machining of Single Crystals," Manuf. Eng. Trans., **9**, pp. 386-396.

Connolly, R., Rubenstein, C., 1968, "The Mechanics of Continuous Chip Formation in Orthogonal Cutting," Int. J. Mach. Tool Des. Res., **8**, pp. 159-187.

Conrad, H., 2004, "Grain-Size Dependence of the Flow Stress of Cu from Millimeters to Nanometers," Metall. Mater. Trans. A, **35A**, pp. 2681-2695.

Cullity, B. D., 1978, *Elements of X-Ray Diffraction*, Addison-Wesley Publishing Company Inc, 2nd ed., USA.

Desai, C. S., Siriwardane, H. J., 1984, *Constitutive Laws for Engineering Materials, with Emphasis on Geologic Materials*, Prentice Hall, Englewood Cliffs, N.J., USA.

Dowling, N. E., 1999, *Mechanical Behavior of Materials: Engineering Methods for Deformation, Fracture, and Fatigue*, Prentice Hall, New Jersey, USA.

Drescher, J., 1993, "Scanning Electron Microscopic Technique for Imaging a Diamond Tool Edge," Precis. Eng., **15** (1), pp.112-114.

Ehmann, K. F., Bourell, D., Culpepper, M. L., Hodgson, T. J., Kurfess, T. R., Madou, M., Rajurkar, K. P., Devor, R. E., 2007, *Micromanufacturing – International Research and Development*, SpringerLink Publication, Netherlands.

Endres, W. J., Devor, R. E., Kapoor, S. G., 1995, "A Dual-Mechanism Approach to the Prediction of Machining Forces, Part 1: Model Development," ASME J. Manuf. Sci. Eng., **117**, pp. 526-533.

Evans, C., Polvani, R., Postek, M., Rhorer, R., 1987, "Some Observations on Tool Sharpness and Sub-Surface Damage in Single Point Diamond Turning," SPIE, **802**, pp. 52-66.

Fang, F. Z., Liu, X. D., Lee, L. C., 2003, "Micro-Machining of Optical Glasses – A Review of Diamond-Cutting Glasses," Indian Academy of Sciences, **28** (5) pp. 945-955.

Fang, F. Z., Venkatesh, V. C., 1998, "Diamond Cutting of Silicon with Nanometric Finish," CIRP Ann-Manuf. Techn., **47**, pp. 45-49.

Fang, F. Z., Zhang, G. X., 2003, "An Experimental Study of Edge Radius Effect on Cutting Single Crystal Silicon," Int. J. Adv. Manuf. Technol., **22**, pp. 703-707

Fang, N., 2003, "Slip-Line Modeling of Machining with a Rounded-Edge Tool – Part I: New Model and Theory," J. Mech. Phys. Solids, **51**, pp. 715-742.

Frost, H. J., Ashby, M. F., 1982, *Deformation Mechanism Maps – The Plasticity and Creep of Metals and Ceramics,* Pergamon, UK.

Gao, H., Huang, Y., 2001, "Taylor-Based Nonlocal Theory of Plasticity," Int. J. Solids Struct., **38**, pp. 2615-2637.

Gao, W., Motoki, T., Kiyono, S., 2006, "Nanometer Edge Profile Measurement of Diamond Cutting Tools by Atomic Force Microscope with Optical Alignment Sensor," Precis. Eng., **30**, PP. 396-405.

Hall, E. O., 1951, "The Deformation and Ageing of Mild Steel: III Discussion of Results," Proc. Phys. Soc., **B64**, pp. 747-753.

Hansen, N., Huang, X., 1998, "Microstructure and Flow Stress of Polycrystals and Single Crystals," Acta Mater., **46** (5), pp. 1827-1836.

Hansen, N., Juul Jensen, D., 1992, "Flow Stress Anisotropy Caused by Geometrically Necessary Boundaries," Acta Metall. Mater., **40** (12), pp. 3265-3275.

Hastings, W. F., Mathew, P., Oxley, P. L. B., 1980, "A Machining Theory for Predicting Chip Geometry, Cutting Forces etc. from Work Material Properties and Cutting Conditions," Proc. R. Soc. Lond., **A371**, pp. 569-587.

Hertzberg, R. W., 1976, *Deformation and Fracture Mechanics of Engineering Materials*, John Wiley & Sons, USA.

Hsu, T. C., 1966, "A Study of the Shear and Normal Stresses on a Cutting Tool," ASME J. Eng. Ind., **88**, pp. 51-64.

Huerta, M., Malkin, S., 1976, "Grinding of Glass: The Mechanics of the Process," ASME J. Eng. Ind., pp. 459-467.

Hughes, D. A., Hansen, N., 2000, "Microstructure and Strength of Nickel at Large Strains," Acta Mater., **48**, pp. 2985-3004.

Hung, N. P., Fu, Y. Q., 2000, "Effect of Crystalline Orientation in the Ductile-Regime Machining of Silicon," Int. J. Adv. Manuf. Technol., **16**, pp. 871-876.

ICSD, 2006, International Crystal Structure Database, FIZ Karlsruhe, Germany and NIST, USA.

Ikawa, N., Shimada, S., and Tanaka, H., 1992, "Minimum Thickness of Cut in Micromachining," Nanotechnology, **3**, pp. 6–9.

Irwin, G. R., 1957, "Analysis of Stress and Strain Near the End of a Crack Traversing a Plate," J. Appl. Mech., **24**, pp. 361-364.

Jasinevicius, R. G., 2006, "Influence of Cutting Conditions Scaling in the Machining of Semiconductors Crystals with Single Point Diamond Tool," J. Mater. Process. Tech., **179**, pp. 111-116.

Jasinevicius, R. G., Duduch, J. G., Pizani, P. S., 2007, "Structure Evaluation of Submicrometre Silicon Chips Removed by Diamond Turning," Semicond. Sci. Technol., **22**, pp. 561-573.

Johnson, G. R., Cook, W. H., 1983, "A Constitutive Model and Data for Metals Subject to Large Strains, High Strain Rates and High Temperatures," *Proceedings of the Seventh International Symposium on Ballistics*, Hague, Netherlands, pp. 541-547.

Kalpakjian, S., Schmid, S. R., 2003, *Manufacturing Processes for Engineering Materials*, Pearson Education Inc., USA.

Kim, J. D., Kim, D. S., 1995, "Theoretical Analysis of Micro-Cutting Characteristics in Ultra-Precision Machining," J. Mater. Process. Tech., **49**, pp. 387-398.

Kishawy, H. A., Haglund, A. J., Deiab, I. M., 2006, "An Analysis of Machining with Honed Tools Using ALE Finite Element Model: Ploughing Force and Minimum Chip Thickness," Trans. NAMRI/SME, **34**, pp. 277-284.

Komanduri, R., Chandrasekaran, N., and Raff, L. M., 1998, “Effect of Tool Geometry in Nanometric Cutting: A Molecular Dynamics Simulation Approach,” Wear, **219**, pp. 84–97.

Kopalinsky, E. M., Oxley, P. L. B., 1984, *Size Effects in Metal Removal Process*, 3rd Conf. Mech. Prop. High Rates of Strain, Oxford, pp. 389–396.

Kovacs, G. T. A., 1998, *Micromachined Transducers Sourcebook*, WCB/McGraw-Hill, New York, USA.

Lawn, B., Evans, A. G., 1977, “A Model for Crack Initiation in Elastic/Plastic Indentation Fields,” J. Mater. Sci., **12**, pp.2195-2199

Lawn, B. R., Jensen, T., Aurora, A., 1976, “Brittleness as an Indentation Size Effect,” J. Matl. Sci. Lett., **11**, pp. 575-577.

Lee, W. B., To, S., Cheung, C. F., 2000, “Effect of Crystallographic Orientation in Diamond Turning of Copper Single Crystals,” Scripta Mater., **42**, pp. 937-945.

Lee, W. B., To, S., Sze, Y. K., Cheung, C. F., 2003, “Effect of Material Anisotropy on Shear Angle Prediction in Metal Cutting – A Mesoplasticity Approach,” Int. J. Mech. Sci., **45**, pp. 1739-1749.

Lee, W. B., Zhou, M., 1993, “A Theoretical Analysis of the Effect of Crystallographic Orientation on Chip Formation in Micromachining,” Int. J. Mach. Tools Manufact., **33** (3), pp. 439-447.

Lei, S., Shin, Y. C., Incropera, F. P., 1999, “Material Constitutive Modeling Under High Strain Rates and Temperatures Through Orthogonal Machining Tests,” ASME J. Manuf. Sci. Eng., **121**, pp. 577-585.

Leung, T. P., Lee, W. B., Lu, X. M., 1998, “Diamond Turning of Silicon Substrates in Ductile-Regime,” J. Mater. Process. Technol., **73**, pp. 42-28.

Li, B. L., Cao, W. Q., Liu, Q., Liu, W., 2003a, “Flow Stress and Microstructure of the Cold-Rolled IF-Steel,” Mater. Sci. Eng., **A356**, pp. 37-42.

Li, X. P., He, T., Rahman, M., 2005, “Tool Wear Characteristics and their Effects on Nanoscale Ductile Mode Cutting of Silicon Wafer,” Wear, **259**, pp. 1207-1214.

Li, X.P., Rahman, M., Liu, K., Neo, K. S., Chan, C. C., 2003b, “Nano-precision measurement of diamond tool edge radius for wafer fabrication,” J. Mater. Process. Technol., **140**, pp. 358-362.

Liu, K., 2002, *Ductile Cutting for Rapid Prototyping of Tungsten Carbide Tools*, Ph.D. thesis, National University of Singapore, Singapore.

Liu, K., Li, X. P., 2001, “Modeling of Ductile Cutting of Tungsten Carbide,” Trans. NAMRI/SME, **29**, pp. 251-258.

Liu, K., Li, X. P., Liang, S. Y., 2003, “Nanometer Scale Ductile Cutting of Tungsten Carbide,” Trans. NAMRI/SME, **31**, pp. 153-160.

Liu, K., Li, X. P., Rahman, M., Liu, X. D., 2004, “A Study of the Cutting Modes in the Grooving of Tungsten Carbide,” Int. J. Adv. Manuf. Tech., **24**, pp. 321-326.

Liu, K., Subbiah, S., Melkote, S. N., 2005, “Material Strengthening Mechanisms and their Contribution to Size Effect in Micro-Cutting,” *ASME International Mechanical Engineering Congress and Exposition*, Orlando, Florida, USA.

Liu, Q., 1994, “A Simple Method for Determining Orientation and Misorientation of the Cubic Crystal Specimen,” J. Appl. Cryst., **27**, pp. 755-761.

Liu, Q., Juul Jensen, D., Hansen, N., 1998, “Effect of Grain Orientation on Deformation Structure in Cold-Rolled Polycrystalline Aluminum,” Acta Mater., **46** (16), pp. 5819-5838.

Liu, X., Devor, R. E., Kapoor, S. G., Ehmann, K. F., 2004, “The Mechanics of Machining at the Microscale: Assessment of the Current State of the Science,” ASME J. Manuf. Sci. Eng., **126**, pp. 666-678.

Mackenzie, J. K., 1958, “Second Paper on Statistics Associated with the Random Disorientation of Cubes,” Biometrika, **45** (1/2), pp.229-240.

Manjunathaiah, J., Endres, W. J., 2000, “A New Model and Analysis of Orthogonal Machining with an Edge-Radiused Tool,” ASME J. Manuf. Sci. Eng., **122**, pp. 384-390.

Masuzawa, T., 2000, “State of the Art of Micromachining,” CIRP Ann-Manuf. Techn., **49** (2), pp. 1-16.

Masuzawa, T., Tonshoff, H. K., 1997, “Three-Dimensional Micromachining by Machine Tools,” CIRP Ann-Manuf. Techn., **46** (2), pp. 621-628.

McKeown, P., 1996, “From Micro- to Nano-machining – Towards the Nanometer Era,” Sensor Review, **16** (2), pp. 4-10.

Merchant, M. E., 1945, “Mechanics of Metal Cutting Process,” J. Appl. Phys., **16**, pp. 267-318.

Moore, M. A., King, F. S., 1980, “Fracture vs Plastic Deformation Processes in the Sliding Abrasive Wear of Ceramics,” Wear **60**, pp. 123-140.

Morris, J. C., Callahan, D. L., 1994, “Origins of Microplasticity in Low-Load Scratching of Silicon,” J. Mater. Res., **9** (11), pp. 2907-2913.

Morris, J. C., Callahan, D. L., Kulik, J., Patten, J. A., Scattergood, R. O., 1995, “Origins of the Ductile Regime in Single-Point Diamond Turning of Semiconductors,” J. Am. Ceram. Soc., **78** (8), pp. 2015-2020.

Moriwaki, T., Shamoto, E., Inoue, K., 1992, “Ultraprecision Ductile Cutting of Glass by Applying Ultrasonic Vibration,” CIRP Ann-Manuf. Techn., **41**, pp. 141-144.

Nakasuji, T., Kodera, S., Hara, S., Matsunaga, H., Ikawa, N., Shimada, S., 1990, “Diamond Turning of Brittle Materials for Optical Components,” CIRP Ann-Manuf. Techn., **39** (1), pp. 89-92.

Nes, E., Holmedal, B., Evangelista, E., Marthinsen, K., 2005, “Modeling Grain Boundary Strengthening in Ultra-Fine Grained Aluminum Alloys,” Mater. Sci. Eng. A – Struct., **410-411**, pp. 178-182.

O’Connor, B. P., Marsh, E. R., Couey, J. A., 2005, “On the Effect of Crystallographic Orientation on Ductile Material Removal in Silicon,” Precis. Eng., **29**, pp. 124-132.

Okazaki, Y., Mishima, N., Ashida, K., 2004, “Microfactory – Concept, History and Developments,” ASME J. Manuf. Sci. Eng., **126**, pp. 837-844.

Oxley, P. L. B., 1989, *The Mechanics of Machining: An Analytical Approach to Assessing Machinability*, Ellis Horwood Limited, Chichester, UK.

Patten, J. A., Cherukuri, H., Yan, J., 2004, “Ductile-Regime Machining of Semiconductors and Ceramics,” Chapter 6, *High-Pressure Surface Science and Engineering*, Gogotsi, Y., Domnich, V., eds., Institute of Physics, Bristol, UK.

Patten, J. A., Gao, W., 2001, “Extreme Negative Rake Angle Technique for Single Point Diamond Nano-Cutting of Silicon,” Precis. Eng., **25**, pp. 165-167.

Patten, J., Gao, W., Yasuto, K., 2005, “Ductile Regime Nanomachining of Single-Crystal Silicon Carbide,” ASME J. Manuf. Sci. Eng., **127**, pp. 522-532.

Petch, N. J., 1953, “Cleavage Strength of Polycrystals,” J. Iron Steel I., **174**(1), pp. 25-28.

Piispanen V., 1937, “Lastunmuodostumisen Teoriaa,” Teknillinen Aikakauslehti, **27**, pp. 315-322.

Piispanen V., 1948, “Theory of Formation of Metal Chips, J. Appl. Phys., **19**, pp. 876-881.

Ramesh, A., 2002, *Prediction of Process-Induced Microstructural Changes and Residual Stresses in Orthogonal Hard Machining*, Ph.D. thesis, Georgia Institute of Technology, Atlanta, USA.

Randle, V., 1993, *The Measurement of Grain Boundary Geometry*, Institute of Physics Publishing, Bristol, UK.

Sarwar, M., Thompson, P. J., 1982, "Cutting Action of Blunt Tools," *Proceedings of the International Machine Tool Design and Research Conference*, pp. 295-304.

Schimmel, R. J., Endres, W. J., Stevenson, R., 2002, "Application of an Internally Consistent Material Model to Determine the Effect of Tool Edge Geometry in Orthogonal Machining," ASME J. Manuf. Sci. Eng., **124**, pp. 536-543.

Schinker, M. G., 1991, "Subsurface Damage Mechanisms at High Speed Ductile Machining of Optical Glass," Precis. Eng., **13** (3), pp. 208-218.

Shackelford, J. F., Alexander, W., 2001, *Material Science and Engineering Handbook*, 3rd ed., CRC Press, NY, USA.

Sharif Uddin, M., Seah, K. H. W., Li, X. P., Rahman, M., Liu, K., 2004, "Effect of Crystallographic Orientation on Wear of Diamond Tools for Nano-Scale Ductile Cutting of Silicon," Wear, **257**, pp. 751-759.

Shaw, M. C., 1987, *Metal Cutting Principles*, Oxford University Press, Oxford, New York, USA.

Shibata, T., Fujii, S., Ikeda, M., 1996, "Ductile-regime Turning Mechanism of Single-Crystal Silicon," Precis. Eng., **18** (2/3), pp. 129-137.

Shimada, S., Ikawa, N., Ohmori, G., Tanaka, H., Uchikoshi, U., 1992, "Molecular Dynamics Analysis as Compared with Experimental Results of Micromachining," CIRP Ann-Manuf. Techn., **41** (1), pp. 117-120.

Sreejith, P., 2005, "Machining Force Studies on Ductile Machining of Silicon Nitride," J. Mater. Process. Technol., **169**, pp. 414-417.

Stephenson, D. A., Agapiou, J. S., 2006, *Metal Cutting Theory and Practice*, 2nd ed., CRC Press, Taylor and Francis Group, Florida, USA.

Strenkowski, J. S., Hiatt, G. D., 1990, "A Technique for Predicting the Ductile Regime in Single Point Diamond Turning of Brittle Materials," ASME, Production Engineering Division (Publication) PED, **43**, Fundamental Issues in Machining, pp. 67-80.

Subbiah, S., 2006, *Some Investigations of Scaling Effects in Micro-Cutting*, Ph.D. thesis, Georgia Institute of Technology, Atlanta, USA.

Suzuki, T., Yonenaga, I., Kirchner, H. O. K., 1995, "Yield Strength of Diamond," Phys. Rev. Lett., **75** (19), pp. 3470-3472.

Tanaka, H., Shimada, S., Ikawa, N., 2004, "Brittle-Ductile Transition in Monocrystalline Silicon Analyzed by Molecular Dynamics Simulation," Proc. Instn. Mech. Engrs., **218** (6), Part C: J. Mech. Eng. Sci., pp. 583-590.

Taniguchi, N., 1983, "Current Status in, and Future Trends of, Ultraprecision Machining and Ultrafine Materials Processing," CIRP Ann-Manuf. Techn., **32** (2), pp. 573-582.

Tow, S. B., McPherson, R., 1986, "Fine Scale Abrasive Wear of Ceramics by a Plastic Cutting Process," p. 865, Science of Hard Materials, Almond, E. A., Brookes, C. A., Warren, R., Arrowsmith, J. W., eds., Bristol, UK.

Ueda, K., Iwata, K., Nakayama, K., 1980, "Chip Formation Mechanism in Single Crystal Cutting of β-brass," CIRP Ann-Manuf. Techn., **29** (1), pp. 41-46.

Ueda, K., Sugita, T., Hiraga, H., Iwata, K., 1991, "A J-Integral Approach to Material Removal Mechanisms in Microcutting of Ceramics," CIRP Ann-Manuf. Techn., **40**, pp. 61-64.

van Houten, F., 2005, "Philips man predicts death of light bulbs as LEDs win," The Inquirer.

Venkatachalam, S., Liang, S.Y., 2007, "Effects of Ploughing Forces and Friction Coefficient in Micro-Scale Machining," ASME J. Manuf. Sci. Eng., **129** (2), 2007, pp. 274-280.

von Blackenhagen, B., Gumbsch, P., Arzt, E., 2001, "Dislocation Sources in Discrete Dislocation Simulations of Thin-Film Plasticity and the Hall-Petch Relation," Model. Simul. Mater. Sc., **9**, pp. 157-169.

Waldrof, D. J., DeVor, R. E., Kapoor, S. G., 1998, "A Slip-Line Field for Ploughing During Orthogonal Cutting,", ASME J. Manuf. Sci. Eng., **120**, pp. 693-699.

Waldrof, D. J., 2004, "A Simplified Model for Ploughing Forces in Turning," Trans. NAMRI/ASME, **32**, pp. 447-454.

Wallace, P. W., Boothroyd, G., 1964, "Tool Forces and Tool-Chip Friction in Orthogonal Machining," J. Mech. Eng. Sci., **6** (1), pp. 74-87.

Xu, H. H. K., Jahanmir, S., Ives, L. K., 1998, "Mechanisms of Material Removal in Abrasive Machining of Ceramics," Interceram, **47** (6), pp. 380-385.

Yan, J., Syoji, K., Kuriyawaga, T., Suzuki, H., 2002, "Ductile Regime Turning at Large Tool Feed," J. Mater. Process. Technol., **121**, pp. 363-372.

Yan, J., Maekawa, K., Tamaki, J., Kubo, A., 2004a, "Experimental Study on the Ultraprecision Ductile Machinability of Single-Crystal Germanium," JSME Int. J., C – Mech. Sy., **47** (1), pp. 29-36.

Yan, J., Syoji, K., Tamaki, J., 2003a, "Some Observations on the Wear of Diamond Tools in Ultra-Precision Cutting of Single-Crystal Silicon," Wear, **255**, pp. 1380-1387.

Yan, J., Takahashi, Y., Tamaki, J., Kubo, A., Kuriyawaga, T., Sato, Y., 2006, "Ultraprecision Machining Characteristics of Poly-Crystalline Germanium," JSME Int. J., C – Mech. Sy., **49** (1), pp. 63-69.

Yan, J., Tamaki, J., Syoji, K., Kuriyawaga, T., 2003b, "Development of a Novel Ductile-Machining System for Fabricating Axisymmetric Aspheric Surfaces on Brittle Materials," Key Eng. Mat., **238-239**, pp. 43-38.

Yan, J., Tamaki, J., Syoji, K., Kuriyawaga, T., 2004b, "Single Point Diamond Turning of CaF_2 for Nanometric Surface," Int. J. Adv. Manuf. Tech., **24**, pp. 640-646.

Yaws, C. L., Dickens, L. L., Lutwak, R., Hsu, G., 1981, "Semiconductors Industry Silicon: Physical and Thermodynamic Properties," Solid State Technol., **24** (1).

Yellowley, I., 1987, "A Simple Predictive Model of Orthogonal Metal Cutting," Int. J. Mach. Tools Manuf., **27** (3), pp. 357-365.

Yoshino, M., Ogawa, Y., Aravindan, S., 2005, "Machining of Hard-Brittle Materials by a Single Point Tool Under External Hydrostatic Pressure," ASME J. Manuf. Sci. Eng., **127**, pp. 837-845.

Zarudi, I., Nguyen, T., Zhang, L. C., 2005, "Effect of temperature and stress on plastic deformation in monocrystalline silicon induced by scratching," Appl. Phys. Lett., **86**, 011922 (1-3).

Zarudi, I., Zhang, L. C., Zou, J., Vodenitcharova, T., 2004a, "The R8–BC8 Phases and Crystal Growth in Monocrystalline Silicon under Microindentation with a Spherical Indenter," J. Mater. Res., **19**, pp. 332-337.

Zarudi, I., Zou, J., McBride, W., Zhang, L. C., 2004b, "Amorphous Structures Induced in Monocrystalline Silicon by Mechanical Loading," Appl. Phys. Lett., **85** (6), pp. 932-934.

Zhang, L. C., 2004, "Plasticity in Monocrystalline Silicon: Experiment and Modeling," Key Eng. Mat., **274-276**, pp. 1-10.

Zhang, L. C., Tanaka, H., 1997, "Towards a Deeper Understanding of Wear and Friciton on the Atomic Scale – A molecular Dynamics Analysis," Wear, **211**, pp. 44-53.

Zhang, L. C., Zarudi, I., 2001, "Towards a Deeper Understanding of Plastic Deformation in Mono-crystalline Silicon," Int. J. Mech. Sci., **43**, pp. 1985-1996.

Zhao, X., Bhushan, B., 1998, "Material Removal Mechanisms of Single-Crystal Silicon on Nanoscale and at Ultralow Loads," Wear, **223**, pp. 66-78.

Zhou, M., Ngoi, B. K. A., Zhong, Z. W., Wang, X. J., 2001, "The Effect of Material Microstructure on Microcutting Processes," Mater. Manuf. Process., **16** (6), pp. 815-828.